INFORMATION TO USERS

The most advanced technology has been used to photograph and reproduce this manuscript from the microfilm master. UMI films the text directly from the original or copy submitted. Thus, some thesis and dissertation copies are in typewriter face, while others may be from any type of computer printer.

The quality of this reproduction is dependent upon the quality of the copy submitted. Broken or indistinct print, colored or poor quality illustrations and photographs, print bleedthrough, substandard margins, and improper alignment can adversely affect reproduction.

In the unlikely event that the author did not send UMI a complete manuscript and there are missing pages, these will be noted. Also, if unauthorized copyright material had to be removed, a note will indicate the deletion.

Oversize materials (e.g., maps, drawings, charts) are reproduced by sectioning the original, beginning at the upper left-hand corner and continuing from left to right in equal sections with small overlaps. Each original is also photographed in one exposure and is included in reduced form at the back of the book.

Photographs included in the original manuscript have been reproduced xerographically in this copy. Higher quality 6" x 9" black and white photographic prints are available for any photographs or illustrations appearing in this copy for an additional charge. Contact UMI directly to order.

U·M·I

University Microfilms International
A Bell & Howell Information Company
300 North Zeeb Road Ann Arbor MI 48106-1346 USA
313 761-4700 800 521-0600

Order Number 9119650

Brillouin scattering study of incommensurate potassium selenate (acoustic anomalies and the Landau free energy)

Li, Gen, Ph.D.

City University of New York, 1991

U·M·I
300 N. Zeeb Rd.
Ann Arbor, MI 48106

A

BRILLOUIN SCATTERING STUDY OF INCOMMENSURATE POTASSIUM SELENATE

(Acoustic Anomalies And The Landau Free Energy)

by

GEN LI

A dissertation submitted to the Graduate Faculty in Physics in partial
fulfillment of the requirements for the degree of Doctor of Philosophy,
The City University of New York.

1991

This manuscript has been read and accepted for the Graduate Faculty in Physics in satisfaction of the dissertation requirement for the degree of Doctor of Philosophy.

Dec 11, 1990
Date

Chair of Examining Committee

Dec 18, 1990
Date

Joseph B. Krieger
Executive Officer

J. Birman

S. Greenbaum

F.W. Smith

D. Weitz

Supervisory Committee

The City University of New York

Abstract

BRILLOUIN SCATTERING STUDY OF INCOMMENSURATE POTASSIUM SELENATE

(Acoustic Anomalies And The Landau Free Energy)

by

Gen Li

Adviser: Professor Herman Z. Cummins

Brillouin scattering studies of K_2SeO_4 in the vicinity of the incommensurate and commensurate phase transitions were performed and analyzed in the following aspects:

(1) The longitudinal acoustic mode propagating along the c^* axis was investigated both in 90° and 180° scattering geometries. A theoretical derivation of the complex elastic constant $\tilde{C}_{33}(\omega)$ was carried out in the framework of Landau theory including both bilinear (Landau-Khalatnikov) coupling to the amplitude mode, and fluctuation contributions from the Σ_2 soft mode above T_i and from pairs of amplitude modes and phase modes below T_i. The contribution of phase modes was considered for the first time in this analysis. Comparison between theory and the Brillouin data led to an excellent fit using free energy parameters close to values deduced from previous static and dynamic experimental results. This analysis also indicated that the phason gap $\Omega_\phi(0)$ is at least 100 GHz. Analysis beyond the mean-field approximation was also discussed.

(2) Transverse acoustic modes propagating and polarized along the crystal axes were investigated in 90° scattering geometries. The C_{44} anomalies above and below T_i were tentatively explained by bilinear coupling with the lowest B_{3g} optical mode. Raman scattering studies of this B_{3g} mode indicated a variation of frequency with temperature which is similar to the variation of C_{44}. The C_{55} anomaly near T_c was explained by coupling to the phase mode with wavevector of $K_i = a^*\delta(T)$. The C_{66} anomaly near T_i was also analyzed with Landau theory. Theoretically predicted transverse acoustic asymmetries due to the coupling with phase modes were also explored.

ACKNOWLEDGEMENTS

I would like to express my deep gratitude to my adviser Professor Herman Z. Cummins for his great encouragement, practical tutelage, patient guidance, and continued support throughout my graduate education and research here.

I express my grateful acknowledgement to Professor Robert M. Pick for his invaluable support and guidance in developing crucial theoretical aspects of this research. I also thank him and his family for the enjoyable hospitality during my visiting in Paris.

I am grateful to Dr. G. Hauret and Miss N. Levain for providing and preparing K_2SeO_4 crystals. Undoubtedly, they provided the basic requirement for our experiments. I also thank Miss N. Levain for instructing me in crystal preparation. I thank Dr. Catherine Dreyfus and Dr. M. Hebbache for their collaboration in the experimental and theoretical studies.

I thank Professor A.P. Levanyuk, Professor T. Yagi and Professor S.K. Esayan for their helpful discussions and suggestions concerning the theory and experiments which formed an important part of our research.

I thank all the members of the light scattering group: Dr. NongJian Tao, Dr. WinKee Lee, Dr. Chester X.W. Qian, Wen Li, XiaoKe Chen, Lloyd Williams, Martin Muschol, Tracy Truner, ShenLi Qiu and VenHong Le (a visitor from Viet Nam) for their assistance, collaboration, and friendship, and for contributing to the good working environment in our Lab and the Physics Department.

I thank Marcelo H. Orellana and Victor W.Q. Mei for their expert electronic design and construction. I thank the machine-shop as a whole for their professional machining. All of them have contributed to our high performance experimental systems.

I thank the members of my thesis committee, Professor J. Birman, Dr. D. Weitz, Professor S. Greenbaum and Professor F.W. Smith for their guidance and help.

I thank all of my friends.Through their encouragement, help and comradeship, they have contributed to this dissertation.

TABLE OF CONTENTS

LIST OF TABLES

LIST OF FIGURES

CHAPTER I

INTRODUCTION

1. INCOMMENSURATE CRYSTAL STRUCTURE

One of the most basic characterizing features of a crystal is its lattice translational periodicity. Traditionally each crystal has been assigned to one of the 230 three-dimensional crystallographic space groups according to the arrangement of the atoms in the unit cell and the crystal lattice symmetry. However in some crystals, there exists a kind of structure in some temperature range called incommensurate which can not be classified into one of the above space groups.

"Incommensurate structures are peculiar quasi-crystalline substances that lack periodic translational symmetry not in a haphazard amorphous way but because two (or perhaps more) elements of translational symmetry are present which are mutually incompatible. Suppose A(r) and B(r) represent the spatial distribution of two characteristic properties of a material and that

$$A(\mathbf{r}) = \sum_{\{\mathbf{G}\}} A_G e^{i\mathbf{G}\cdot\mathbf{r}}, \qquad B(\mathbf{r}) = \sum_{\{\mathbf{G}\}} B_G e^{i\mathbf{G}\cdot\mathbf{r}}. \tag{1.1.1}$$

The structure is incommensurate if the sets of reciprocal lattice vectors $\{\mathbf{G}\}$ and $\{\mathbf{G}'\}$ have only the trivial elements $\mathbf{G} = \mathbf{G}' = 0$ in common" [A1]. Generally incommensurate structures can be classified into four types: Magnetic, compositional, intergrowth/overgrowth, and displacive. In the displacive type, the two incommensurate characteristic properties are the displacement field u(r) and the periodic density of the unmodulated crystal, ρ_m. In general, an incommensurate structure is developed from a high temperature prototype structure through a second order phase transition at T_i and is stable in a certain temperature range (or ranges) in which the modulation wave vector usually becomes larger when temperature is lower. At some temperature T_c a commensurate structure becomes more stable and the system will lock into the commensurate phase with a first order lock-in phase transition.

Even though incommensurate structures cannot be classified into any of the normal three-dimensional space groups, deWolff[D1] has discussed the classification for structures with one-dimensional modulation by exploiting the symmetry of the four-dimensional structure of

$$\mathbf{K} = h\mathbf{a}^* + k\mathbf{b}^* + l\mathbf{c}^* + m\mathbf{q}, \tag{1.1.2}$$

where $(\mathbf{a}^*, \mathbf{b}^*, \mathbf{c}^*)$ are the three reciprocal basis vectors of the undistorted lattice, $\mathbf{q}$ is the wave vector of the modulation wave and (h, k, l, m) are integers.

There are several special characteristic features that make the incommensurate structure interesting: (a) The most characteristic features of incommensurate structures are their diffraction patterns in which besides the primary Bragg reflections, there exists a secondary set of satellite reflections with their own characteristic spacing [A2]. In spite of this discrete crystal-like diffraction pattern, incommensurate structures are not crystalline in the generally accepted sense because they lack translational periodicity. (b) The condensation below T_i of the two degenerate soft optical modes which exist above T_i generates two non-degenerate soft modes in the incommensurate phase: the amplitudon which is the usual totally symmetric soft mode, and the phason which (at $\mathbf{q} = 0$) is a zero-energy Goldstone mode. (c) There are two order parameters in the incommensurate system: Near T_i in the incommensurate phase, the modulation wave is essentially sinusoidal, so the order parameter is the amplitude of the incommensurate distortion. While near T_c the modulation evolves into an array of phase solitons which is described by a time-independent sine-Gordon equation, and the order parameter is the soliton density.

Because incommensurate modulations break the three-dimensional translation periodicity in a special way, incommensurate structures show new phenomena that do not exist in ordinary periodic crystals. By studying incommensurate structures and their phase transitions, we may extend our knowledge of physics from three-dimensional periodic to more complicated systems, and improve the understanding of aperiodic materials.

2. STRUCTURE OF K_2SeO_4

The Structure of the K_2SeO_4 (Potassium Selenate) crystal has been investigated by many groups. It exhibits four phases in different temperature range as shown in figure 1.2.1.

In the highest temperature phase, which exists from melting to 745K (T_1), the K_2SeO_4 crystal has hexagonal symmetry and belongs to the space group $D_{6h}^4 - P_{6_3/mmc}$. From the results of their experimental and phenomenological studies, Shiozaki et al.[S1] concluded that the phase transition from hexagonal to orthorhombic symmetry at T_1 was due to the instability of an optical mode belonging to the M_4 representation with a wave vector of $q = (0, 2\pi/\sqrt{3}a_H, 0)$. Where a_H is the lattice constant in the hexagonal phase.

In the normal phase between 745K (T_1) and 129.5K (T_i), the crystal structure of K_2SeO_4 was first determined by Kalman et al.[K1] (in 1970) though von Gattow[G1] (in 1962) had pointed out that the structure is isomorphous with $\beta - K_2SO_4$. In this phase, the crystal has orthorhombic symmetry and belongs to the space group of $D_{2h}^{16} - P_{nam}$. The cell dimension at room tem-

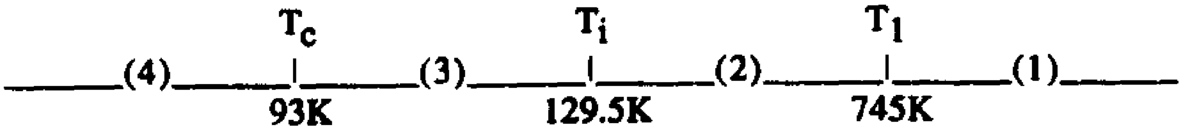

Phase 1	Hexagonal; $D_{6h}^{4}\text{-}P_{6_3/mmc}$ (α- K_2SO_4)	$Z = 2$
Phase 2	Orthorhombic; $D_{2h}^{16}\text{-}P_{nam}(b>a>c)$ (β- K_2SO_4); Paraelectric; (Normal Phase) At T=300K : $a = 7.661Å$, $b = 10.466Å$, $c = 6.003Å$ $n_a = 1.549$, $n_b = 1.539$, $n_c = 1.543$; $\rho_m = 3.05 g/cm^3$	$Z = 4$
Phase 3	Incommensurate $q_o = \frac{a^*}{3}[1-\delta(T)]$	
Phase 4	Commensurate; Orthorhombic; $C_{2v}^{9}\text{-}P_{na}2_1$ $q_c = a^*/3$; ferroelectric P_z	$Z = 12$

Figure 1.2.1. Phases of K_2SeO_4. Z is the number of formular units per unit cell.

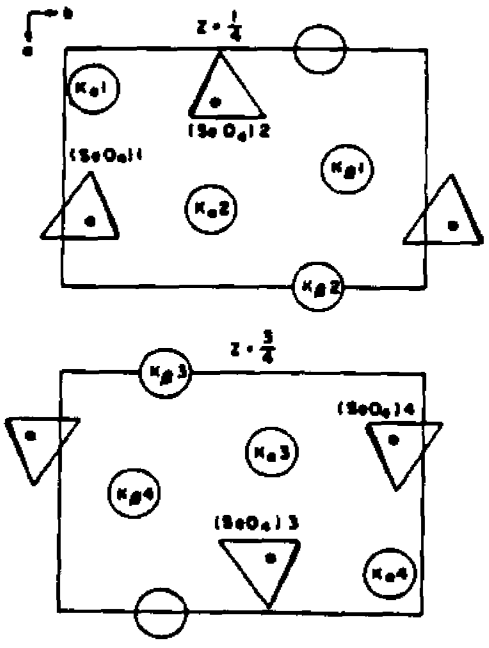

Figure 1.2.2. Schematic structure of the P phase K_2SeO_4. Two levels along the c direction at heights 1/4 and 3/4 are shown separately. K_α and K_β are symmetrically nonequivalent potassium ions. Numbering identifies ions or groups (from Iizumi et al. [11]).

perature are:

$$a = 7.661 \pm 0.004\text{Å} \quad b = 10.466 \pm 0.008\text{Å} \quad c = 6.003 \pm 0.001\text{Å}. \quad (1.2.1)$$

Figure 1.2.2 shows the schematic structure of K_2SeO_4. The unit cell contains four formula units (28 atoms). There are two non-equivalent sites for the potassium ions, K_α and K_β, which lie in special positions on the mirror planes at $z = \frac{1}{4}$ and $z = \frac{3}{4}$. The selenium ions at the center of the tetragonal SeO_4 groups also occupy special positions on the mirror planes and therefore mirror planes of the tetragonal groups coincide with the mirror planes of the lattice. In fact, the orthorhombic structure is a slightly distorted hexagonal structure with the a axis being the pseudo-hexagonal axis and the ratio of b/c being $1.7437 \approx \sqrt{3}$ in the P_{nam} notation in which the a axis is coincident with the hexagonal axis direction of the high temperature phase (hexagonal symmetry phase). In this phase, the crystal is paraelectric.

A major neutron scattering experiment was reported by Iizumi et al.[11] in 1977. In their experiment, they found that in this normal phase, there exists a lowest-lying transverse soft optical phonon branch which propagates along (1, 0, 0) and has the symmetry of the Σ_2 irreducible representation with a minimum at $q = \frac{a^*}{3}(1-\delta_0)$. Figure 1.2.3 shows the temperature dependence of the dispersion curve of this Σ_2 branch. Characterizing the dispersion curve by the Fourier series

$$[\hbar\omega(\xi)]^2 = \sum_n F_n(1-\cos n\pi\xi), \qquad (1.2.2)$$

they found that when the temperature decreasing towards T_i, the force constants between nearest-neighbor layers and second-neighbor layers, F_1 and F_2, are decreasing. In contrast, the force constant between third-neighbor layers is increasing and becomes the predominant component, resulting with the softening of phonon energy at about (1/3, 0, 0). At T_i, the incommensurate transition temperature, and the soft mode at $q = \frac{a^*}{3}(1-\delta_0)$ on the Σ_2 branch condensed, the soft mode instability transforms the crystal into a displacive incommensurate structure.

The incommensurate phase exists from 129.5K (T_i) to 93K (T_c). After the normal-incommensurate phase transitions, the "frozen-in" soft optical mode becomes a one-dimensional static modulation wave. The neutron diffraction study in this phase by Iizumi et al.[11] indicated that the satellites generated by the modulation wave are not exactly at superlattice positions. Instead, the wavevector is $q = \frac{a^*}{3}(1-\delta)$, where δ is a temperature-dependent mismatch parameter. They found that when temperature is decreased from T_i towards T_c, the value of δ decreases continuously from $\delta_0 \approx 0.07$ to about 0.02, as shown in figure 1.2.4. They also found that the intensity of the first-order satellites, which is proportional to the amplitude squared of the modulation wave, starts from zero and increases continuously with decreasing temperature. The fact that there is no abrupt change of either δ or the intensity of the satellites at T_i suggests that the incommensurate phase transition is second-order.

Based on their neutron scattering results and symmetry analysis, Iizumi et al.[11] concluded that the major components of the structural modulation consist of rotation of the SeO_4 groups around the b-direction and associated translation of K ions along the c-direction. The observations of the incommensurate structure were extended by Yamada et al.[11][12][13] by x-ray diffraction. Their results supported the predictions from the neutron scattering experiment. Several important points were obtained from their measurements: (a) The SeO_4 tetrahedra are almost regular and displace rigidly. (b) No higher order satellites were observed which indicates that the modulation is nearly sinusoidal. (c) The bond length between oxygen atoms belonging to adjacent SeO_4 tetrahedra changes remarkably from the normal phase and fluctuates widely in the incommensurate phase. These results provide a better understanding of the incommensurate instability.

At T_c, the incommensurate-commensurate phase transition point, the mismatch parameter δ abruptly drops from 0.02 to zero as shown in figure 1.2.4. The wavevector of the modulation becomes $q = \frac{a^*}{3}$. X-ray diffraction results [12] indicated that the "lock-in" phase transition is characterized by the structural modulation becoming commensurate with the lattice as well as an additional homogeneous structural change both in rotation of SeO_4 groups around the b-axis and in translation of K_α (see figure 1.2.2) ions along the c-axis.

In the commensurate phase, the crystal structure has orthorhombic symmetry and belongs to the space group of $C_{2v}^9-P_{na}2_1$. The modulation wave with $q = \frac{a^*}{3}$ results the unit cell being tripled along the a axis relative to the normal phase. Associated with the "lock-in" transition, a macroscopic dielectric polarization is generated by secondary atomic displacements induced by fourth-order anharmonic coupling of P_0 to the primary lattice modulation. Thus K_2SeO_4 in this phase is an improper ferroelectric with the spontaneous polarization along the c-direction.

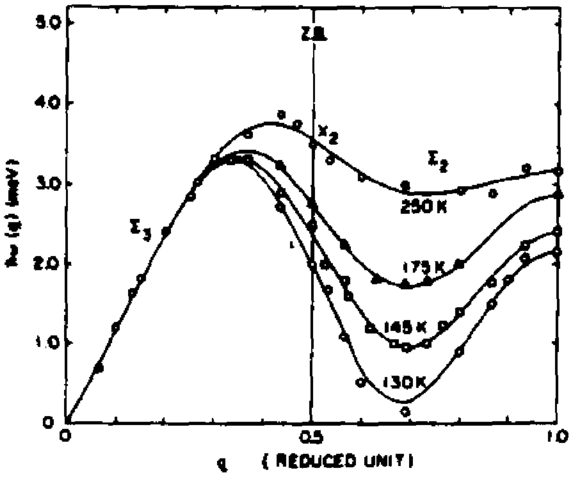

Figure 1.2.3. Dispersion curve of the Σ_2 soft mode along with the Σ_3 acoustic mode plotted in an extended zone which is doubled along the a^* axis. Z.B. indicates the original zone boundary. Solid lines show the results of fitting of Eq. (1.2.2) (from Iizumi et al. [11]).

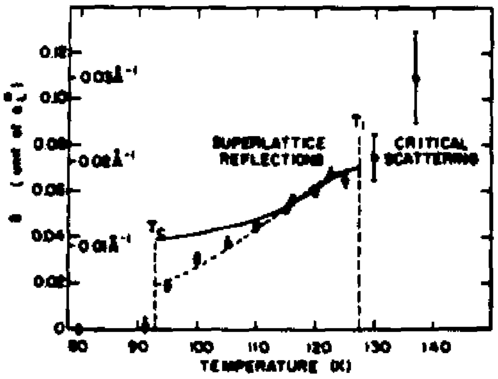

Figure 1.2.4. Temperature dependence of δ. Solid line is calculated result. (from Iizumi et al. [11]).

CHAPTER II

REVIEW OF PREVIOUS STUDIES OF K_2SeO_4

1. EXPERIMENTAL STUDIES

Among the A_2BX_4 family of incommensurate insulators, K_2SeO_4 is perhaps the best studied by various experimental techniques; it has also played a major role in understanding modulated incommensurate structures and the phase transitions.

a. X-ray diffraction and neutron scattering studies

The two successive phase transformations of K_2SeO_4 at $T_i = 129.5K$ and $T_c = 93K$ were first found in 1970 by Aiki et al.[A3][A4] in specific heat and dielectric constant measurements. They also found that the transition at T_c is to a ferroelectric phase with the spontaneous polarization along the c-axis. Following Aiki et al.'s discovery, Terauchi et al.[T1] carried out a x-ray diffraction measurement of the temperature dependence of the satellites in the temperature range between the two transition points. They failed to detect the incommensurate spacing of the satellites and concluded that the satellites are always at the commensurate positions of $\mathbf{q} = \frac{\mathbf{a}^*}{3}$.

A very important neutron scattering study of K_2SeO_4 was reported by Iizumi et al.[I1] in 1977. Above T_i, by inelastic neutron scattering, they explored the temperature dependence of the lowest lying soft optical Σ_2 branch (shown in figure 1.2.3). The dispersion curve for this branch shows a well defined soft mode at $\mathbf{q} \approx \frac{\mathbf{a}^*}{3}$ which condenses at T_i. This soft mode instability provides a dynamic explanation for the normal-incommensurate transformation. Lacking a microscopic explanation for the incommensurate lattice instability, they used a phenomenological force constant analysis of the soft-mode dispersion curves. With the picture of competition of the interaction forces among three layers, they could explain the softening of the Σ_2 branch. Below T_i, by precisely measuring the peak positions of the satellite reflections, they found that the reflections are characterized by a wave vector $q = \frac{a^*}{3}(1-\delta)$. The deviation δ changes with temperature and disappears discontinuously at T_c (as shown in figure 1.2.4). From these results, they concluded that the phase transition at T_i is the transformation to an incommensurate structure and the transition at T_c is an incommensurate to commensurate phase transition. They also presented a discussion of the incommensurate-commensurate transition and the simultaneous occurrence of the commensurate phase and the spontaneous polarization by using a Landau free energy expansion in which the coupling term $Q^3(q_\delta)P_2(q_{3\delta})$ plays an essential role both in driving the incommensurate-commensurate phase transformation and inducing the spontaneous polarization.

After the elucidation of the incommensurate properties of K_2SeO_4 by Iizumi et al., many further experimental investigations were carried out. In their x-ray diffraction study, Chen et al.[C1] (1981) observed thermal hysteresis at the incommensurate- commensurate transition. Kudo[K1] (1982) reported x-ray diffraction results for the satellite positions and intensities in the incommensurate phase. Their results are in good agreement with the neutron scattering results. More detailed x-ray diffraction studies were carried out by Yamada et al.[Y1][Y2][Y3]. Based on the concept of de Wolff's four-dimensional lattice space, they analyzed the structures of K_2SeO_4 in the incommensurate phase and evaluated the eigenvectors of the modulation mode from the observed atomic displacement pattern. They also analyzed the structure in the commensurate phase and revealed the details of the structural change at the incommensurate-commensurate phase transition. Several important results of their work have been mentioned in the last section of chapter I.

After Iizumi et al., further neutron scattering studies were reported by several groups. Majkrzak et al.[M1] (1980) studied the temperature dependence of the primary and secondly satellites by neutron diffraction. Press et al.[P1] (1980) studied the effects of hydrostatic pressure on the normal-incommensurate phase transition. Axe et al.[A6] (1980) studied the dispersion and temperature dependence of the "amplitudon" and "phason" (they were not able to measure the behavior of the phason branch when $T \rightarrow T_c$ from below or in the incommensurate phase, what they studied was only the "pseudo-phason".) which represent the fluctuations in amplitude and phase of the modulation wave below T_i. Figure 2.1.1 shows their results for the temperature dependence of the soft mode frequences. Their results are in agreement with the Raman data reported by Wada et al.[W1][W2] in 1977.

In 1983, Quilichini et al.[Q1] reported their neutron scattering study on the phason branch in the incommensurate phase of K_2SeO_4. They observed a heavily damped inelastic feature near the strong satellite reflection and they identified it as the phase-mode response. By fitting their data to a damped harmonic oscillator response function with the assumption of a wavevector independent phason damping with linear temperature dependence (which was estimated by using the Raman and neutron results in the normal and commensurate phases), they obtained a non-zero gap for the phason branch dispersion curve as shown in figure 2.1.2. By extrapolating to q = 0, They found a phason gap of $\Omega_\Phi \approx 60GHz$.

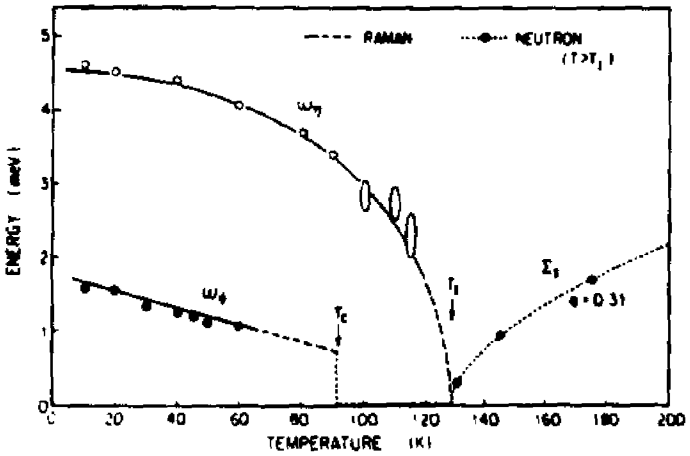

Figure 2.1.1. Temperature dependences of q = 0 phase and amplitude mode frequencies. Solid lines indicate Raman scattering results, data points are neutron results.The dashed portions of the ω_ϕ is entirely schematic serving to indicate that ω_ϕ is expected to vanish at T_c (from Axe et al. [A6]).

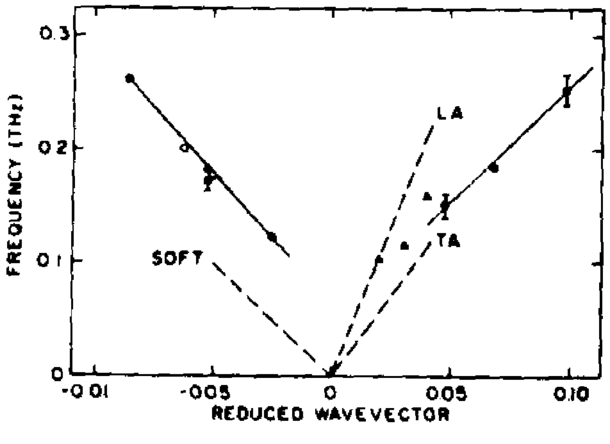

Figure 2.1.2. Phason dispersion of K_2SeO_4 for $q//a^*$: circles are neutron data (closed-120K, open-100K); triangles are Raman data; acoustic slopes are shown as broken lines, for comparison (from Quilichini et al. [Q1]).

b. Raman scattering studies

Wada et al.[W1][W2] (1977) reported Raman scattering studies of the soft modes in the incommensurate and commensurate phases. They obtained the temperature dependence of the frequencies and damping constants of the amplitudon and pseudo-phason. Unruh et al.[U1] repeated the Raman scattering measurement on the two soft modes in 1979. With the help of the higher resolution of their triple monochromator, they extended the measurement closer to T_i and found that the frequency of the amplitudon can be described by $\Omega_A = 11.2(cm^{-1})[127.4-T(k)]^{0.26}$. Also they observed a remarkable increase of the amplitudon damping when the temperature approached T_i from below. Their results are shown in figure 2.1.3. Further Raman investigations on the amplitudon were carried out by the groups of Fleury et al.[F1], Wada et al.[W3] Kolpakov et al.[K2], Echegut et al.[E1] and Lee at al.[L1].

A Raman scattering study of the phase mode in the incommensurate phase of K_2SeO_4 was performed by Inoue et al.[I2] in 1983. They found that the pseudo-phason in the commensurate phase developed into an over-damped mode in the incommensurate phase. Based on a damped harmonic oscillator model, their analysis gave a phason frequency with a q=0 gap which was later found by Quilichini et al.[Q1] to be consistent with their neutron scattering results.

c. Specific heat and thermal expansion studies

After Aiki et al. more specific heat measurement of K_2SeO_4 in the vicinity of T_i and T_c were carried out [L2][C2][F2][A7]. A small specific heat anomaly was found at T_c and a second-order transition behavior was found at T_i, as shown in figure 2.1.4. The specific heat jump at T_i found by Chaudhuri et al.[C2] and by Flerov et al.[F2] were $8.5JK^{-1}mol^{-1}$ and $10.1JK^{-1}mol^{-1}$

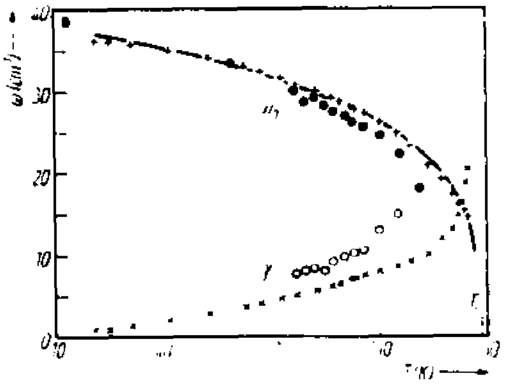

Figure 2.1.3. Eigenfrequency ω_0 and damping constant γ of the amplitude mode of K_2SeO_4 versus temperature. Circles are the results of Wada at al. [W1] for comparison (from Unruh et al. [U1]).

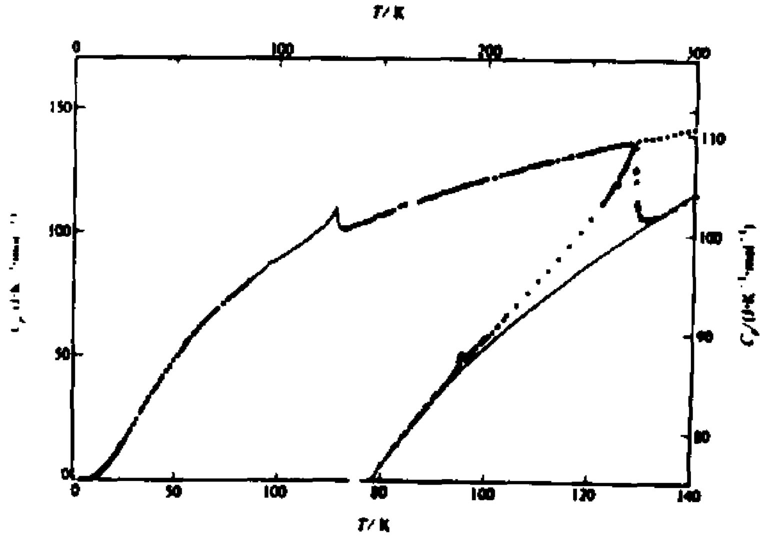

Figure 2.1.4. Heat capacities of K_2SeO_4 (from Chaudhuri et al.[C2]).

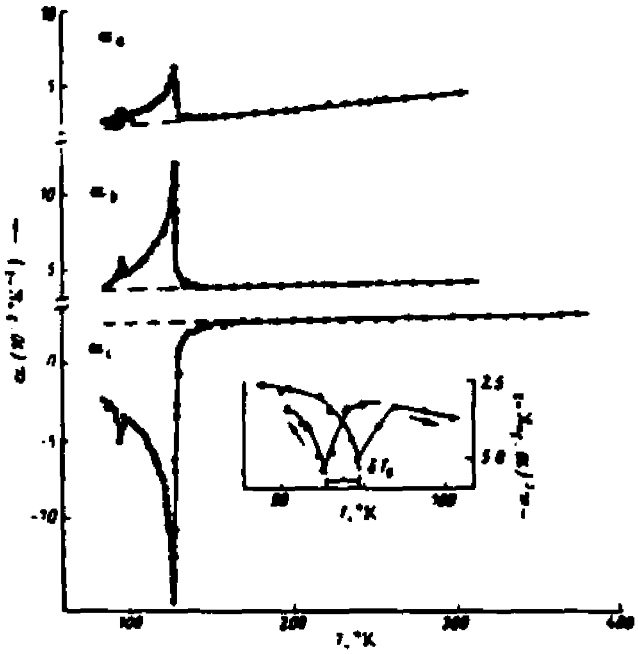

Figure 2.1.5. Linear thermal expansion coefficients of K_2SeO_4 measured along the a, b and c axes (from Flerov et al.[F2]).

respectively. Flerov et al. also studied the behaviors of the linear thermal expansion coefficients along the three crystal axes. Big discontinuous changes were found at T_i for all three directions with $(\Delta\alpha_a, \Delta\alpha_b, \Delta\alpha_c) = (3.4, 8.1, -19.1)\times10^{-5}K^{-1}$, and small anomalies were found at T_c. Their experimental results are shown in figure 2.1.5.

A thermal expansion measurement on K_2SeO_4 was performed by Shiozaki et al.[S1] in 1977. The measurement was reexamined by Midorikawa[M2] in 1981. His result is in better agreement with the results of neutron scattering under high pressure by Press et al.[P1] and the results of the x-ray measurement on the lattice constant by Kudo et al.[K3]. In both thermal expansion measurements, remarkable changes were observed at the normal-incommensurate phase transition in the slopes of the thermal expansion (as a function of T) along the three crystal axes. In the incommesurate phase, the spontaneous strains along the **a** and **b** axes show linear temperature dependence while along the **c** axis shows non-linear temperature dependence. A small discontinuity in the thermal expansion in the c direction was observed by Midorikawa at Tc, indicating that this transition is of first order.

d. Ultrasonic and Brillouin scattering studies

Ultrasonics and Brillouin scattering studies of K_2SeO_4 were reported by several groups. Yagi et al.[Y4][C3] were the first to investigate the temperature dependence of the elastic constants of the pure longitudinal acoustic modes of K_2SeO_4. A large anomaly was observed with decreasing temperature for the C_{33} longitudinal acoustic mode Brillouin frequency, with about a 25% downward rounded step around T_i, and a gradual increase after T_i.

Rehwald et al.[R1] combined ultrasonic and Brillouin scattering results together in their report in 1980 in which they measured the temperature

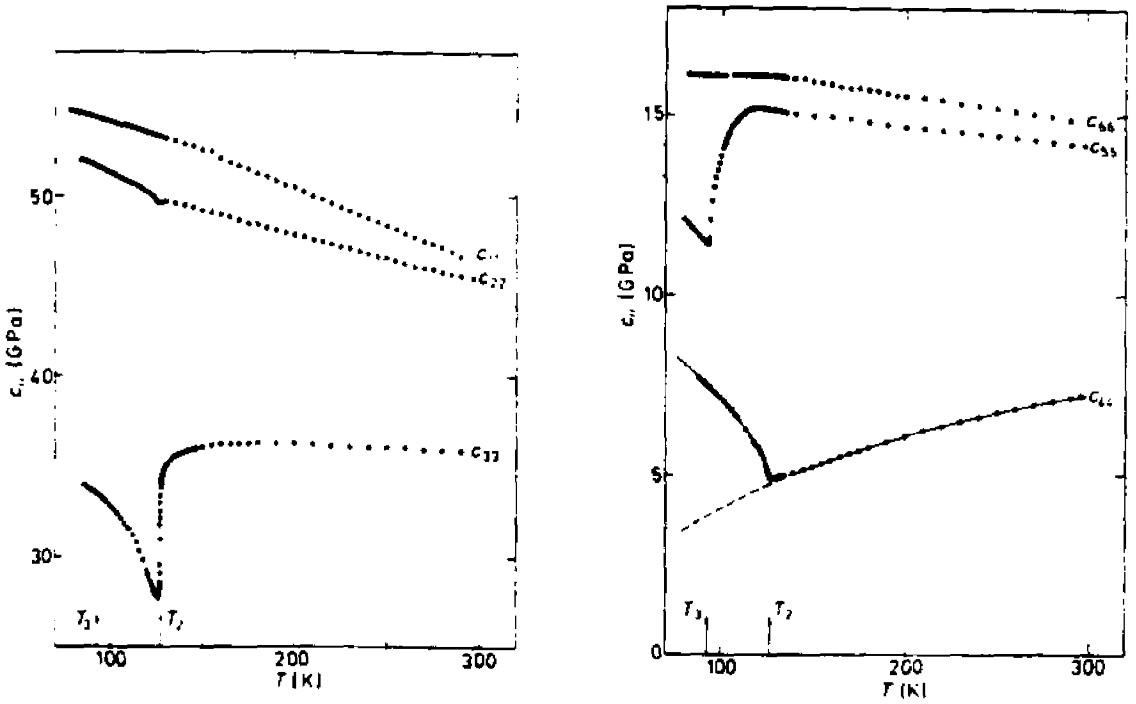

Figure 2.1.6. Variation of the elastic stiffness functions of K_2SeO_4 with temperature from ultrasonic measurements (from Rehwald et al.[R1]).

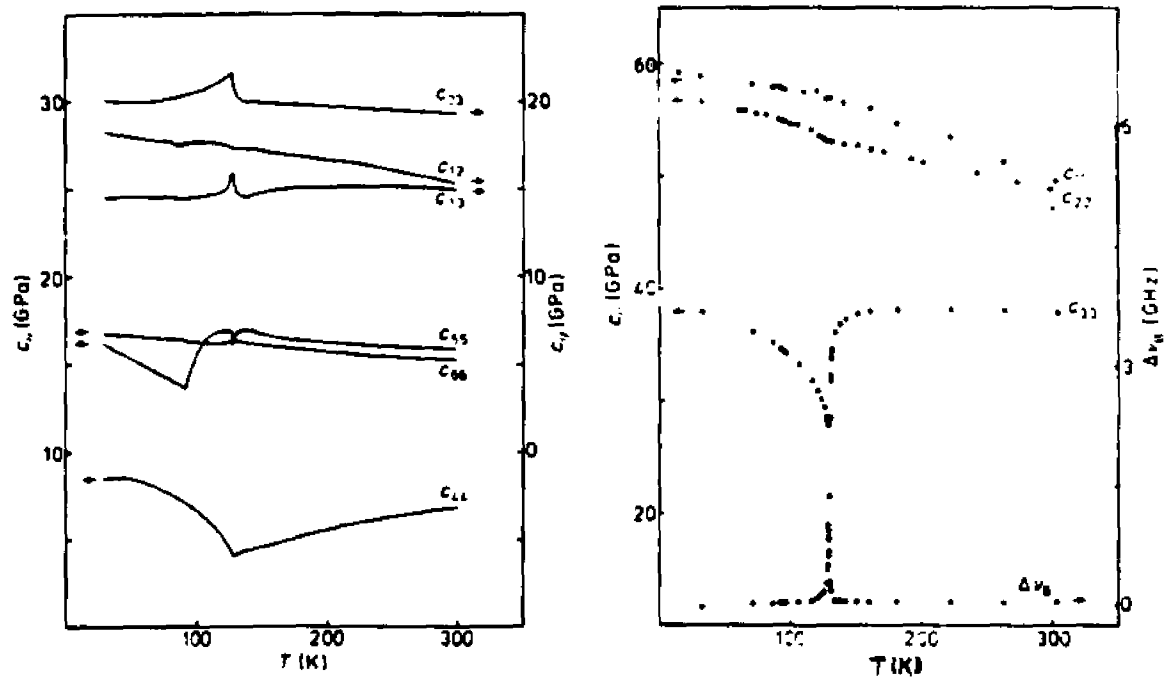

Figure 2.1.7. Variation of the elastic stiffness functions and sound attenuation of the longitudinal sound wave along (001) of K_2SeO_4 with temperature from Brillouin scattering. The solid lines are calculated from the stiffness functions of 'pure'- and 'quasi'- phonons (from Rehwald et al.[R1]).

dependence of the elastic constants $C_{11}-C_{66}$ (see figure 2.1.6 and 2.1.7). The results from both measurements are similar (They did not succeed in detecting the Brillouin scattering from the pure transverse modes because of the small scattering cross section). They determined the C_{44}, C_{55} and C_{66} from the quasi-longitudinal and quasi-transverse phonons for the hypersonic frequency. In their measurements, characteristic variations in the vicinity of T_i were observed for the elastic functions of C_{22}, C_{33}, C_{13}, C_{23} and C_{44}. For the C_{33} longitudinal acoustic mode, besides the remarkable anomaly of the frequency decreasing around T_i as reported by Yagi et al., they found that the damping also experienced a pronounced increase around T_i. The C_{44} elastic constant also shows considerable changes around T_i, decreasing when temperature approaches T_i from both sides. Around T_c, only C_{55} exhibits large variations, with about a 25% decrease in the incommensurate phase. Based on a Landau-type power-series expansion of the free-energy, they interpreted the anomalies of the elastic functions as a consequence of the coupling of strains to the order parameter in the incommensurate and commensurate phases. In a more detailed analysis of the C_{55} anomaly from their ultrasonic measurement [R2], they investigated the role of phason coupling and the existence of soliton-like discommensurations close to T_c in the incommensurate phase.

More Ultrasonic studies of the anomalies of the elastic constants were reported by Hoshizaki et al.[H1], Esayan et al.[E2], and Lemanov et al.[L3]. In further Brillouin scattering studies, Hauret et al.[H2] carried out an analysis of the damping of the C_{33} longitudinal acoustic mode in the incommensurate phase around T_i based on the linear coupling between the incommensurate deformations and an overdamped mode which is equivalent to a Debye relaxation process. They found a relaxation time of $\tau = \frac{\tau_0}{(T_i-T)}$ where

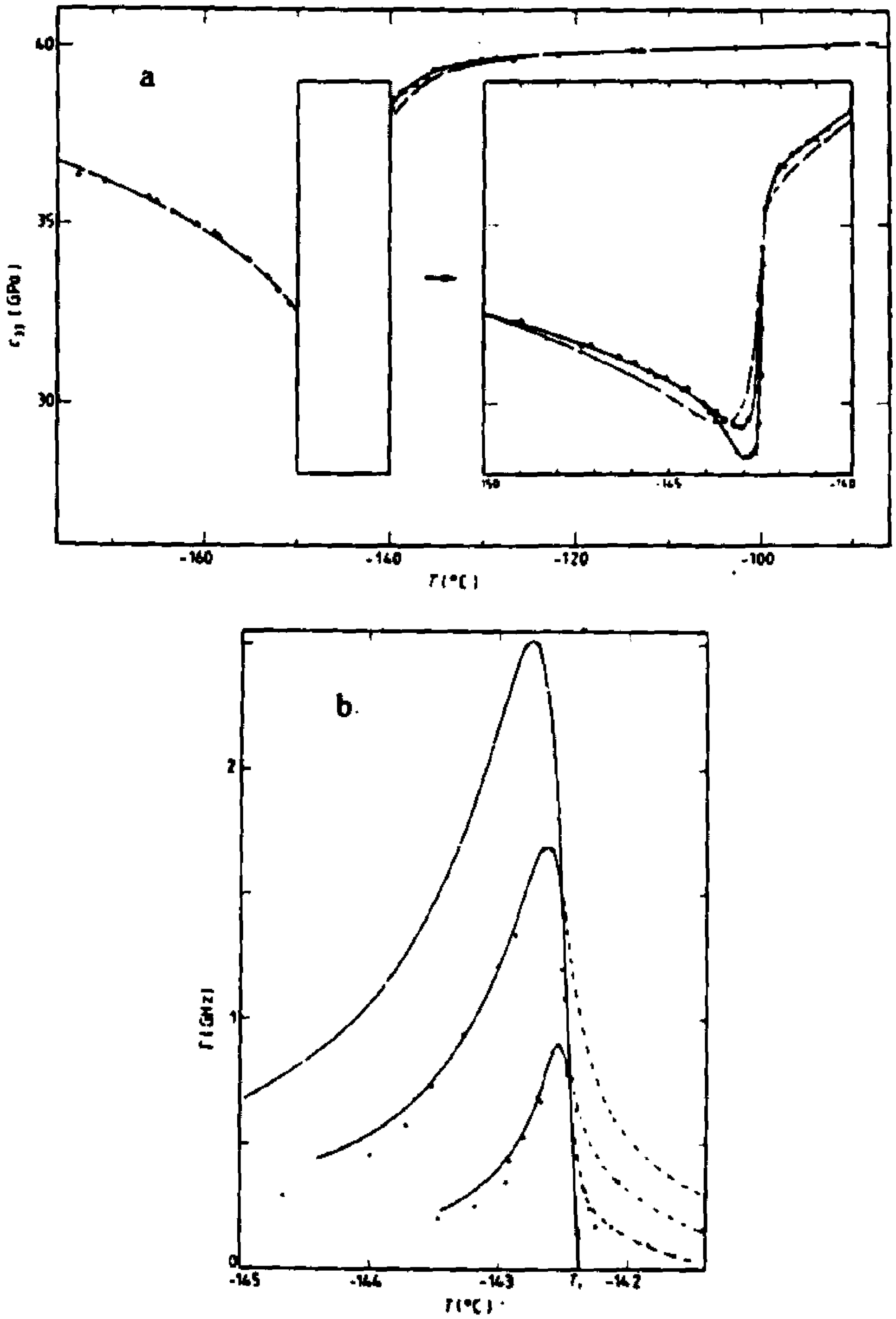

Figure 2.1.8. The temperature dependence of C_{33} (a) and the FWHM (*b*) of K_2SeO_4 for $\theta = 45°$ (triangles), 90° (closed circles) and 135° (open circles) from Brillouin scattering (from Luspin et al.[L4]).

$\tau_0 = 2.6\times10^{-12}$sK. Luspin et al.[L4] reported their Brillouin scattering studies of the wavevector dependence of the C_{33} mode anomaly in the incommensurate phase around T_i by changing the scattering angles (see figure 2.1.8). Hydrostatic pressure effect and uniaxial stress effect on the C_{33} anomalies were reported by Benoit et al.[B1] and Billesboch et al.[B2] respectively. Additional review and discussion of the analysis of Brillouin scattering results will be given in subsequent chapters in which we will make comparison with our results.

e. Other experimental studies

Incommensurate K_2SeO_4 has been intensively studied by many other experiments: Dielectric constant measurement [A5][G2][V1][M3][S2][K3][H3][H4], millimeter wave measurement [P2][V1][V2], piezoelectric resonance [K5] and magnetic resonance [J1][C4][S3][F3][T2]. The recent NMR measurement results reported by Topic et al.[T2] indicated that the phason has a non-zero gap of about 160GHz.

2. THEORETICAL STUDIES

Many theoretical studies on the incommensurate structure and the phase transitions of K_2SeO_4 have been carried out by many groups and with various models. The principal theories may roughly be sorted as follows:

a. Lattice dynamics

An interlayer force competition phenomenological lattice dynamics analysis was first applied by Iizumi et al.[I1] in 1977 to explain the dispersion relations of the temperature-dependent soft optical Σ_2 branch of K_2SeO_4 observed from their neutron scattering studies. Assuming that the interactions between lattice layers perpendicular to the direction of the modulation wavevector are represented by interlayer harmonic force constants, they found that the dispersion relation could be well described by the Fourier decomposition of equation (1.2.2), in which only terms with n $\leqslant 3$ give the main contributions. From the temperature dependence of the force constants, they concluded that the softening of the Σ_2 branch and the condensation of the soft mode at $\mathbf{q} \approx \frac{\mathbf{a}^*}{3}$ is the result of the competition of the first, second and third layer interaction forces in which F_1 and F_2 decrease with temperature whereas F_3 increases and becomes the predominant component. In their study of the hydrostatic pressure effect on the incommensurate transition of K_2SeO_4, Press et al.[P1] extended the lattice dynamics analysis and concluded that the three-force-constant approximation does make specific predications about the pressure dependence of the soft phonon branch.

b. Ab initio lattice dynamics

In 1980, Haque and Hardy[H5] reported their ab initio lattice-dynamics studies of the incommensurate phase transition in K_2SeO_4. Using the known K_2SeO_4 structure, they combined general Coulomb interactions and short-range interactions between restricted numbers of close neighbors into a Born-von Karman rigid-ion model. The associated short-range force constants were fixed by using the static equilibrium conditions and the observed Raman frequencies. By varying the temperature which is simulated by varying the short-range force constants, they found that the crystal has a low-frequency optical branch of Σ_2 symmetry which displays softening and instability for wavevector $\mathbf{q} \approx 0.3\mathbf{a}^*$. Haque and Hardy noted that the instability is very sensitive to changes in a small number of potassium-oxygen and inter-anion oxygen-oxygen potentials. By decomposing the squares of the normal mode frequencies into a sum of Coulomb and short-range components, they found that the instability was resulted from a near cancellation of stabilizing Coulomb forces and destabilizing short-range contributions.

Recently, Lu and Hardy[1.5][1.16] reported their new approach to the first-principle simulations of the phase transitions in K_2SeO_4. In this simulation, they performed ab initio quantum chemistry calculation for an isolated SeO_4^{2-} ion and calculated the electron charge density for the whole SeO_4^{2-} ion and individual Se and O atoms. After a symmetry-restricted static relaxation, in which both the intramolecular and intermolecular interaction potentials are determined, they obtained a room-temperature structure which is very close to the experimental structure. A further lower temperature symmetry restricted static relaxation also gives a close fit to the low temperature experimental structure. They concluded the a double-well type of structure in the potential energy surface is the driving mechanism of the phase transitions.

c. Phenomenological Landau theory

Phenomenological models based on a Landau theory have been widely utilized to investigate the incommensurate phase and the phase transitions of K_2SeO_4. Iizumi et al.[11] were the first to explain the phase transitions of K_2SeO_4 by using an extended Landau theory. By taking the lattice distortion Q_q with wavevector $\mathbf{q} = (\frac{1}{3},0,0)$ as the primary order parameter and the spontaneous polarization P_z as a secondary order parameter, they found that the interaction term $Q_q^3P_z$ can provide explanations for the incommensurate-commensurate phase transition and the induction of the spontaneous polarization below T_c. They also noted that the strain component ϵ_5 which is related to the transverse xz acoustic mode has the same symmetry as P_z and that a similar coupling effect is possible.

A further theoretical study on K_2SeO_4 was reported by Sannikov and Levanyuk[S4] in 1978 based a free energy in which the primary order parameter describes the change of the symmetry of the ferroelectric phase relative to the normal phase. They found that the Lifshits gradient invariant term in the free energy is required to describe a phase transition from a normal phase to an incommensurate phase. They also noted that a higher-order (sixth rather than fourth order used in the previous studies) anisotropy invariant is essential in the description of the phase transition from an incommensurate to a commensurate polarized phase. In this analysis, the contribution of the coupling terms of $Q_q{}^3P_z$ and $Q_q{}^3\epsilon_5$ will renormalize the coefficient of the sixth order term for the Lock-in transition at T_c.

In contrast to the previous studies in which the coefficients of the free energy were treated as fitting parameters and adjusted to fit individual experimental results, Sannikov and Golovko[S5] reported a systematic study of K_2SeO_4 based on the Landau-type free energy. They quantitatively evaluated most of the coefficients of the free energy by using various results from different experiments. In this way, the validity of the Landau free energy was verified.

Many calculations and analyses based on the Landau theory have been carried out over the years. Ishibashi[I3] calculated the temperature dependences of the specific heat in the incommensurate phase by solving the Landau-type thermodynamic potential within the phase modulation-only approximation. Under the same approximation, Mashiyama[M3][M4] calculated the dielectric susceptibility. Comprehensive overviews on the theoretical and experimental studies on K_2SeO_4 can be found in the reviews of Axe[A8], Ishibashi[I4] and Cummins[C5].

b. Three-dimensional XY model

Since their introduction by Wilson[W4], n-component Landau-Ginzburg-Wilson (LGW) Hamiltonian models have been successfully applied in describing critical phenomena of many phase transitions. By using the renormalization-group techniques and field theoretic methods [W4][W5][L11][L12], this theory can be used to calculate quantities such as the critical exponents for various systems.

K_2SeO_4 has a second-order displacive normal-incommensurate phase transition with a two component order parameter of continuous symmetry. Thus the two component (n=2) Landau-Ginzburg-Wilson Hamiltonian is appropriate near the transition point. The critical behavior should then belong to that of the universality class of the 3-dimensional (d=3) XY model. The critical exponents of this (d=3, n=2) model have been calculated by Le Guillou et al.[L11][L12] who found $\gamma = 1.316$, $\nu = 0.669$ and $\beta = \frac{1}{2}(\nu d - \gamma) = 0.3455$. The temperature dependences of the soft mode frequency $\Omega_{\Sigma_2}(q_o)$ and the modulus of the primary order parameter $\rho(T)$ of K_2SeO_4 should behave as $\Omega^2_{\Sigma_2}(q_o)\ \alpha\ (T-T_i)^{\gamma}$ and $\rho^2\ \alpha\ (T_i-T)^{2\beta}$, respectively.

Iizumi et al.[I1] were the first to explore the possibility of describing the normal-incommensurate phase transition of K_2SeO_4 with a 3-dimensional XY model. In their neutron scattering studies of K_2SeO_4, they analyzed the intensity of the primary satellite reflection which is proportional to ρ^2 and obtained the critical exponent of $2\beta \approx 0.8 \pm 0.1$. This value obviously deviates from the mean-field results of $\gamma = 1$, $\nu = \frac{1}{2}$, $2\beta = 1$ [L13]. Based on the free energy they used which, by suppressing the secondary order parameter, is an example of a Landau-Ginzburg-Wilson Harmiltonian with an (n=2)-component vector, they suggested that the true critical behavior of K_2SeO_4 might be that of the XY model. A further neutron diffraction study and analysis of the normal-incommensurate phase transition of K_2SeO_4 was reported by Majkrazak et al.[M1] in 1980. They measured the critical exponents associated with the primary and secondary diffraction satellites and found them to be $2\beta = 0.75 \pm 0.05$ and $2\tilde{\beta} = 1.57 \pm 0.07$, respectively. These values are in reasonable agreement with the theoretical estimates $2\beta = 0.70 \pm 0.04$ and $2\tilde{\beta} = 1.69 \pm 0.09$ of the 3-dimensional XY model.

Recently, Chen[C7] reported a new analysis of the specific heat anomalies of K_2SeO_4 and Rb_2ZnCl_4 near the normal-incommensurate phase transition. Based on the 3-dimensional XY model, he compared the experimental data with the theoretical calculations in which the critical exponents [L12] and other universal features were fixed to the XY universality class. Very close agreement between the theory and the experimental results [C2][A7][L2] were found in this analysis. He concluded that normal-incommensurate phase transitions in the A_2BX_4 family do belong to the universality class of the 3-dimensional XY model.

3. OUR BRILLOUIN SCATTERING STUDIES OF K_2SeO_4

As mentioned in the previous sections, acoustic anomalies of K_2SeO_4 in the vicinity of the incommensurate (T_i) and lock-in (T_c) phase transitions have been studied by many groups with ultrasonic [H1][R1][R2][L3], acoustic resonance [K5] and Brillouin scattering methods [F1][Y4][C3][R1][H2][L4][B1]. However, to date there has been no attempt to establish whether or not the details of the acoustic anomalies observed in these experiments can be successfully explained by the Landau free energy with coefficients determined by independent experiments rather than being considered as free fitting parameters. Also, analysis of the anomaly of the longitudinal elastic constants based on an equal treatment of the Landau-Khalalnikov bilinear coupling effect and fluctuation effects which arise from the same anharmonic coupling terms in the free energy, has not been done in the previous studies. Furthermore, previous attempts at direct observation and study of Brillouin scattering from the pure-transverse acoustic modes by other groups has not been successful. From the consideration of the symmetry of phasons with small wavevector and the symmetry of the transverse acoustic modes, theoretical analysis [E2][E3][G3][G4][P3] predicted certain asymmetries for transverse sound waves under interchange of their propagation and polarization directions. Transverse sound waves with a vector **q** perpendicular to the modulation axis and with displacements along the modulation axis could couple to phasons, whereas sound waves with **q** along the modulation axis and displacements along the perpendicular direction can not couple. Therefore, asymmetric behavior is expected for the related elastic constants or attenuations or both. However, there is no light-scattering study reported on the investigation of this kind of asymmetry effect. Therefore, we have performed the following research:

(1). Brillouin scattering (90° and 180°) studies of the C_{33} LA mode in which we have analyzed the elastic constants and the damping by using a Landau-free energy expansion with most of the free energy coefficients determined by other existing experimental results, in the spirit of the Sannikov-Golovko approach. In the analysis, all anharmonic terms resulting from third order coupling between the LA phonon and pairs of excitations lying on the soft mode branch are taken into account simultaneously. The main analysis is based on a self-consistent mean field framework. Approaches beyond the mean field approximation are also briefly discussed.

(2). Brillouin scattering studies of the anomalies of yz, zx and xy pure transverse acoustic modes which are directly related to the elastic constants of

C_{44}, C_{55} and C_{66}. The anomalies are analyzed also based on the Landau-type free energy.

(3). Brillouin scattering investigations of the asymmetric behavior of the transverse acoustic modes.

CHAPTER III

EXPERIMENTAL APPARATUS AND DATA ANALYSIS

1. BRILLOUIN SCATTERING APPARATUS

a. Fabry-Perot interferometers

Brillouin scattering spectroscopy using Fabry-Perot interferometers is a well established method for investigating thermally excited sound waves in solids and liquids. A single plane Fabry-Perot etalon consists of two high quality plane mirrors mounted accurately parallel to one another and separated by an optical path length L. For a single-pass Fabry-Perot, the transmission function is given by

$$T_1 = \frac{T_o}{1+\frac{4F_1^2}{\pi^2}\sin^2[\frac{2\pi L}{\lambda}]}, \qquad (3.1.1)$$

where T_o is the maximum possible transmission of the system, λ is the wavelength of the transmitted light and F_1 is the finesse which is defined as the ratio of the FSR (free spectral range) to the FWHM (full width at half maximum) of the instrument response. A schematic plot of equation (3.1.1) is shown in figure 3.1.1. For a Fabry-Perot, the finesse depends on the mirror reflectivity and the departure of the mirror surfaces from ideal planes. With the consideration of these two effects, we have a reflectivity finesse, F_r, and a surface finesse, F_s:

$$F_r = \frac{\pi\sqrt{R}}{1-R}, \qquad (3.1.2)$$

$$F_s = \frac{m}{2}, \qquad (3.1.3)$$

where R is the reflectivity of each mirror and $\frac{m}{\lambda}$ is the r.m.s. variation of the mirror surfaces flatness. In a real system, light is collected from a finite size source and over a finite solid angle so that the collimated light is not perfectly parallel, as shown in figure 3.1.2. This effect will causes an additional broadening of the transmission peak. For a pinhole of diameter d at the focus of a collimating lens of focal length f, the pinhole finesse is given as

$$F_p = \frac{4\lambda f^2}{d^2L}. \qquad (3.1.4)$$

The combined finesse F_1 is given by

$$\frac{1}{F_1^2} = \frac{1}{F_r^2}+\frac{1}{F_s^2}+\frac{1}{F_p^2}. \qquad (3.1.5)$$

The contrast of the system is defined as the ratio of the maximum transmission to the minimum transmission and is related to the finesse of the system by

$$C_1 = \frac{T_{max}}{T_{min}} = 1+\frac{4F_1^2}{\pi^2}. \qquad (3.1.6)$$

For a typical single pass Fabry-Perot interferometer system with R = 98%, λ = 488nm, m/λ = 200, L = 1cm, d = 150μm and f = 10cm, the calculated finesse is 60 and the contrast is about 1500. When other imperfections of the system are included, the actual finesse is usually about 50 with a contrast of about 1000.

Although the finesse of a single pass Fabry-Perot system can be further increased up to a limit of about 80, the low contrast limits its application in observing weak Brillouin signals in the presence of the usually extremely

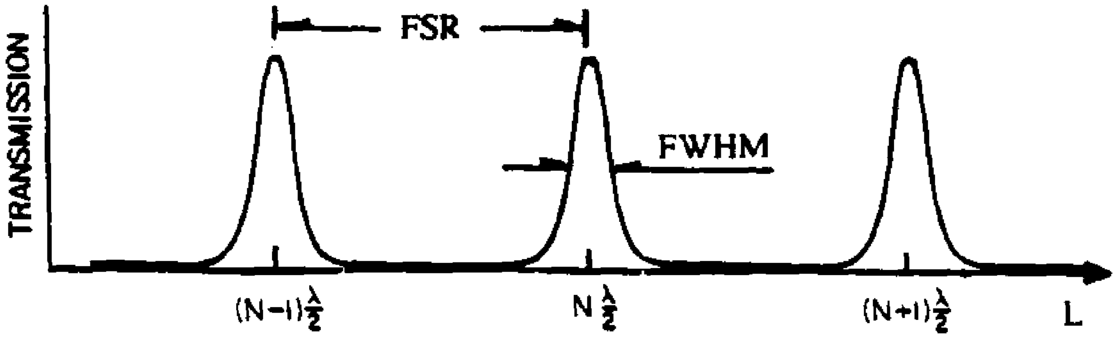

Figure 3.1.1. Schematic plotting of equation (3.1.1) as a function of L. The transmission of monochromatic light through a single cavity Fabry-Perot interferometer is a periodic function of the mirror spacing.

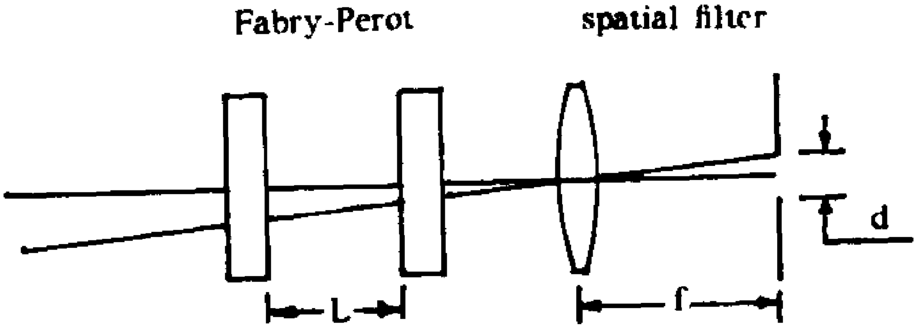

Figure 3.1.2. The non-parallel components of the collected light would cause an additional broadening of the transmission function.

intense elastically scatted light. This problem can be solved by using a multi-pass Fabry-Perot interferometer[B5][S7]. For a n-pass single Fabry-Perot system in which light traverses the Fabry-Perot n times at different positions, the transmission function is just the n-th power of equation (3.1.1):

$$T_n = (T_1)^n. \tag{3.1.7}$$

The finesse and the contrast of the system are

$$F_n = \frac{F_1}{(2^{\frac{1}{n}}-1)^{\frac{1}{2}}}. \tag{3.1.8}$$

$$C_n = (C_1)^n. \tag{3.1.9}$$

3-pass and 5-pass are the multi-pass systems commonly used. For a 5-pass Fabry-Perot interferometer system with $R = 95\%$, a finesse of $F_5 \geqslant 70$ and a contrast $C_5 \geqslant 10^{10}$ can easily be achieved.

Although a multi-pass interferometer can provide high finesse and high contrast, it suffers, like a single-pass Fabry-Perot interferometer, from the overlapping of neighboring interference orders which introduces ambiguity to the analysis of the measured spectra and can even make the measurement impossible if the spectrum contains many (or broad), features. Efforts have been made to solve this problem by constructing interferometers consisting of two Fabry-Perot etalons of unequal spacing in tandem operation. Light will be transmitted through the system only when both Fabry-Perots satisfy the resonance conditions of

$$m_1\frac{\lambda}{2} = L_1 \qquad m_2\frac{\lambda}{2} = L_2, \tag{3.1.10}$$

where m_1 and m_2 are integers, and L_1 and L_2 are the mirrors separations of the first and second Fabry-Perot. To scan the transmitted wavelength, a synchronization condition must be satisfied:

$$\frac{\delta L_1}{\delta L_2} = \frac{L_1}{L_2}, \tag{3.1.11}$$

where δL_1 and δL_2 are the variations of L_1 and L_2 during the scan.

A tandem Fabry-Perot interferometer (TFPI) introduced by Sandercock in 1978 [S8] provides a practicable solution to the problem. This Sandercock TFPI consists of two Fabry-Perot etalons interferometers in which the scanning mirrors of both interferometers are mounted on a common translation stage. The axis of the first Fabry-Perot is along the scan axis while the second is rotated, as shown in figure 3.1.3, by an angle θ. The spacings of the two Fabry-Perots are related by

$$L_2 = L_1\cos\theta. \tag{3.1.12}$$

This relation automatically satisfies the synchronization condition of equation (3.1.11). The transmission functions for a single-pass of each Fabry-Perot are

$$T_{FP1} = \frac{T_o}{1+\frac{4F_1^2}{\pi^2}\sin^2\frac{2\pi L_1}{\lambda}}, \tag{3.1.13a}$$

$$T_{FP2} = \frac{T_o}{1+\frac{4F_1^2}{\pi^2}\sin^2\frac{2\pi L_1\cos\theta}{\lambda}}. \tag{3.1.13b}$$

The total transmission function for light passing the two Fabry-Perots in tandem is

$$T_{1x1} = T_{FP1}T_{FP2}. \tag{3.1.13c}$$

Schematic plots of equations (3.1.13) are shown in figure 3.1.4. It shows clearly how the neighboring interference orders are suppressed because of equation (3.1.12). By setting up a multi-pass for the Sandercock TFPI, we obtain a high suppression of the neighboring interference orders, high

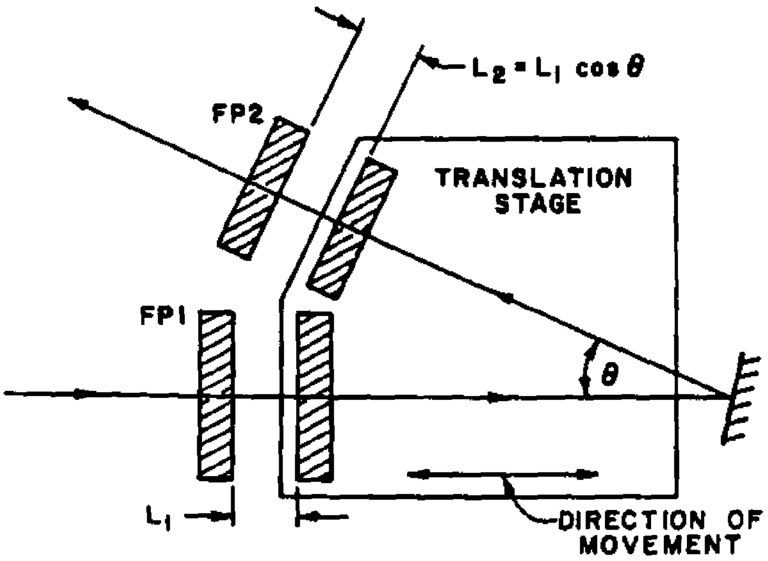

Figure 3.1.3. The scanning stage of the Sandercock TFPI which automatically satisfies the synchronization condition of equation (3.1.11).

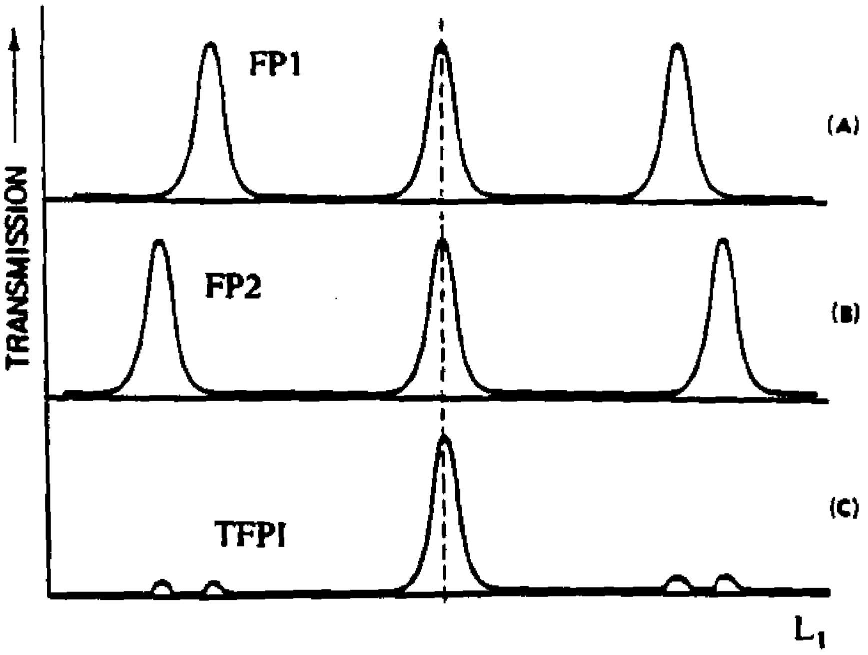

Figure 3.1.4. Schematic plotting of equations (3.1.13) as functions of L_1. Neighboring interference orders are suppressed in the Sandercock TFPI by the condition of equation (3.1.12).

resolution, high contrast and thus a high performance Brillouin scattering system.

b. Brillouin scattering instrumentation

The interferometer used in our Brillouin scattering spectrometer is a Sandercock TFPI set up for 6-pass (3×2) operation. The mirrors mounted on the interferometer are 60mm diameter fused silica flats obtained from "ICOS" with a reflectivity of R=92-94% at $\lambda = 4880-5145\text{Å}$ and a flatness of about $\lambda/150$ over the central 46mm region. The back surface of each mirror is antireflection coated to minimize transmission losses and unwanted reflection. According to equations (3.1.2) and (3.1.3), the corresponding finesses for the mirrors are $F_r \approx 37$ and $F_s \approx 75$, while for the 6-pass (3×2), we have $F_{r(6)} \approx 106$ and $F_{s(6)} \approx 200$. The angle between the second Fabry-Perot axis and the scan axis is $\theta = 18°$ and the mirror separation range is $L_1 = 0-27$mm. The mirror used for coupling the first and second Fabry-Perots has reflectivity R=99% and a flatness of $\lambda/40$.

A schematic diagram of the 90° Brillouin scattering apparatus is shown in figure 3.1.5. A Spectra-Physics 165 Argon ion laser with a built-in air spaced etalon is used as a light source which can be operated in a single-mode at 4880Å or 5145Å. The stability and quality of the single-mode output of the laser is checked regularly by using a Coherent Optics model 670 spherical Fabry-Perot (SFP) with a free spectral range of 8 GHz. The scan of the SFP is driven by a 25V ramp and the output of the SFP is monitored by an oscilloscope. With careful adjustment of the laser cavity and the etalon, one can obtain true single mode output from the laser.

The single-mode laser light is focused onto the sample and the scattered light is collected at 90° by the focusing lens of the first spatial filter. To

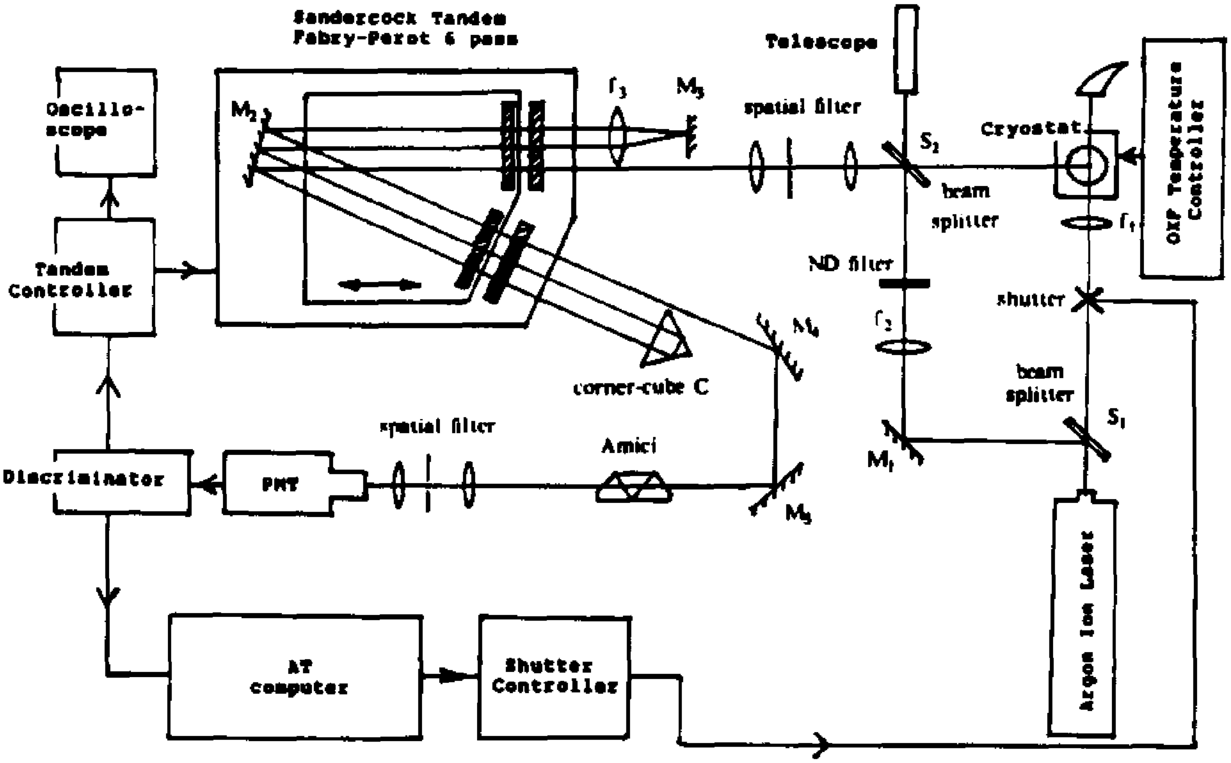

Figure 3.1.5. Schematic illustration of the 6-pass TFPI Brillouin scattering apparatus.

minimize the aperture broadening, we collect light in a small solid-angle with a collecting aperture of 1:0.088 (about 5×10^{-4} sr). The incident light is polarized perpendicular to the scattering plane and the polarization of the scattered light may be analyzed by placing a polarizer in the path of the collected light. To protect the potomultiplier tube (PMT) from overload when the elastic scattering from a sample is too strong, a computer controlled fast shutter is placed before the focusing lens f_1. The shutter is controlled so that it will close in some intervals of each scan where the signal is too strong. A suitable intense reference beam of the laser frequency is required for automatic stabilization when the shutter is in operation. This is achieved by the beam splitter S_1 and a continuously adjustable neutral density (ND) filter that provides the reference beam that by-passes the shutter. The second beam splitter S_2 has two uses: first, it sends the reference beam into the system, second, it acts as a mirror for viewing the sample through the telescope so that a high optical quality path of the sample can be selected. The scattered light (and reference light) is collected and passed through the first spatial filter which serves to define the scattering volume. The size of the pinhole in the spatial filter is chosen (100-250μm) according to equation (3.1.4) such that $F_p \approx 150$. The collimated light is then analyzed with the TFPI. The combination of the coupling mirror M_2, corner-cube C, and cat's-eye element (f_3 and M_3) reflects the beam and adjusts the beam positions to complete the 6-pass (3×2) through the TFPI.

Because the frequency response of the PMT is much wider than the effective free spectral range of the TFPI, significant background noise would be caused by the light outside the free spectral range such as Raman scattering and fluorescence from the sample and optics, ambient room light, etc. In order to eliminate these background effects, we use an Amici dispersing prism and a spatial filter as a final bandpass filter. By using a f = 250mm focusing lens and a $300\mu m$ diameter pinhole in the spatial filter, from the angular dispersion of the Amici prism of $d\alpha/d\lambda = 0.028^{\circ}nm^{-1}$, we have a bandwidth of 2.4nm for the bandpass filter, which is the same as the common interference narrow band filter. The transmission of this bandpass filter is about 90%, much higher then a narrow band interference filter ($R \approx 50\%$) or a diffraction grating.

The analyzed light is detected by a Hamamatsu model R464 PMT which has a spectral response range of 300-650nm with peak wavelength at 420nm. This PMT can be operated in the temperature range of $-80^{\circ}C$ to $+50^{\circ}C$. The normal operating voltage is 1kv and the gain is about 6×10^{6}. At room temperature, the dark count is about 2.5 counts/second (a little too high in some cases of weak Brillouin scattering signal). By using a Canberra Industries model 813 discriminator/pre-amplifier, the output of the PMT is converted into TTL signals which are recorded by a data acquisition system during the interferometer scan (the data acquisition system is described in the following section). The PMT output also serves, by feeding back to the TFPI controller, as a reference for stabilizing the TFPI.

The scan, alignment and stabilization of the TFPI is controlled by a Sandercock TFPI controller which came with the TFPI. The scan of the interferometer is performed by a piezoelectric transducer (PZT). To compensate for the non-linearity of the scanning PZT, a plane capacitor is contained in the TFPI with its capacitance inversely proportional to the extension of the PZT. By driving the PZT with a voltage which is controlled by the separation of the capacitor, a linearized scanning is achieved. With a careful adjustment of the linearizing circuit [s9], our TFPI system can have a linearity of $\geqslant 98\%$. The fine adjustments of the Fabry-Perot mirrors are made with six additional PZTs which support the non-scanning mirrors of the two Fabry-Perots. In the initial alignment, the adjustment may be handled by switching off the stabilization and changing the voltages across the PZTs manually . When acquiring data, automatic alignment can be applied by switching on the stabilization which will maximize the central transmission peak during scanning.

To achieve long-term stability, special attention has to be paid to the influences of vibration coupling. To decouple the vibration from the surrounding environment, the whole Brillouin scattering apparatus is mounted on a compressed air floating optical table (Modern Optics). The decoupling of vibrations arising from the equipment is accomplished by supporting the laser and the TFPI unit with anti-vibration rubber pads.The other optics are supported solidly by metal holders and guiding rails. To minimize the influence of the air motion between the Fabry-Perot mirrors and obtain better thermal uniformity, a plexiglas box is used to enclose the entire interferometer. With these precautions, the system can scan continuously for days without destabilization.

To maintain the high contrast of the multi-pass Fabry-Perot system, masks are placed at the front and back of the Fabry-Perots, in front of the coupling mirror and corner cube, and in some necessary places to eliminate stray reflections from imperfect optical surfaces.

With the apparatus described above, we obtain a finesse of $\geqslant 65$ at a mirror separation of 1.0cm, a contrast of $\approx 10^{10}$ and a suppression of ≈ 300 of neighboring interference orders for a sandblasted copper block sample.

For temperature control, samples are mounted on the coldfinger of an Air Products Cryotip continuous flow nitrogen (or helium) cryostat with optical widows. Temperature is controlled by an Oxford ITC-4 platinum resistance temperature controller with an accuracy of ±0.1K. Details of the cryostat and temperature controller are given in appendix B.

2. DATA ACQUISITION AND ANALYSIS

An IBM-AT compatible computer equipped with an EG&G Ortec ACE-MCS multi-scalar board was used for the data acquisition. This EG&G hardware and software package is capable of storing data to memory in only 2 microseconds, allowing very short collection times ($2\mu s$ - 35.7min per channel per scan). The built-in counter can accept TTL signals or signals directly from the PMT. The scan length can be up to 4096 channels with a minimum length of 4 channels. The count rate can be up to 100 MHz for TTL signals and 100 KHz for analog signals. The "live" display feature allows us to monitor the spectrum during acquisition, whereas the background-job feature allows us to use the computer for other purpose while the EG&G board is collecting data by itself.

In everyday operation, a total of 1024 channels is generally used with a collection time of 0.5ms/channel-scan which matches the time scale of 1024channel×0.5ms/channel-scan of the TFPI set by the TFPI controller. Sequential scans are accumulated to build up the Brillouin components until a satisfactory Brillouin signal is obtained (the accumulation time can be from 10 minutes to 10 hours, depending on the Brillouin scattering intensity). Collected spectra are stored in the IBM compatible computer and subsequently transferred to the science division VAX/780 for analysis with a nonlinear least squares fitting program. A hard-copy of a recorded spectrum can be obtained with a HP 7040A x-y plotter interfaced to the IBM-type computer.

The program (tandemfit.f) used for analyzing the Brillouin spectra was developed from a standard (taurosv.f) nonlinear least-squares fitting program based on the Rosenbrock stepping method. A list of the tandemfit.f program is given in appendix C.

To show how the fitting procedure is organized, let's first have a look at the structure of a Brillouin scattering spectrum. Figure 3.2.1 shows a typical room temperature 90° Brillouin scattering spectrum of K_2SeO_4 crystal with the wavevector, q, of the acoustic phonons along the (001) direction (mirror separation of the FP1: 0.700cm, laser light wavelength: 488nm). The strong narrow peak (R) at the center of the spectrum is the Rayleigh scattering component which essentially represents the instrument transmission response. The two small peaks (G_L and G_R) at both sides of the spectrum are the suppressed neighboring interference orders (ghosts) of the central line. As indicated in figure 3.1.4, because the FP1 and FP2 have deferent separations, their corresponding ghosts are in different positions. In frequency space, the inner pair on both sides is due to FP1 and the outer pair, to FP2. In the spectrum of figure 3.2.1, G_L and G_R consist of these two pairs of ghosts merged with each other. The two other enlarged peaks (LA_L and LA_R) are the Stokes and anti-Stokes Brillouin components of the longitudinal acoustic modes with q//c. They are the the convoluted results of the instrumental response, $\bar{I}(\omega)$, with the spectrum of the sound wave, $S(\omega)$. In general the spectral function $S(\omega)$ can be well represented by the imaginary part of a damped harmonic oscillator response multiplied by a Bose-Einstein factor[16]. In the classical limit, we have

$$S(\omega) = \frac{k_B T}{\omega} \frac{\omega\gamma}{(\omega^2-\omega_o^2)^2+\omega^2\gamma^2}, \tag{3.2.1}$$

where γ is the damping constant of the acoustic mode. The experimental intensity spectrum of the Brillouin scattering is given as

$$I(\omega) = A\int \bar{I}(\omega-\omega') \frac{\gamma\, d\omega'}{(\omega'^2-\omega_o^2)^2+\omega'^2\gamma^2}, \tag{3.2.2}$$

where A is a frequency independent constant.

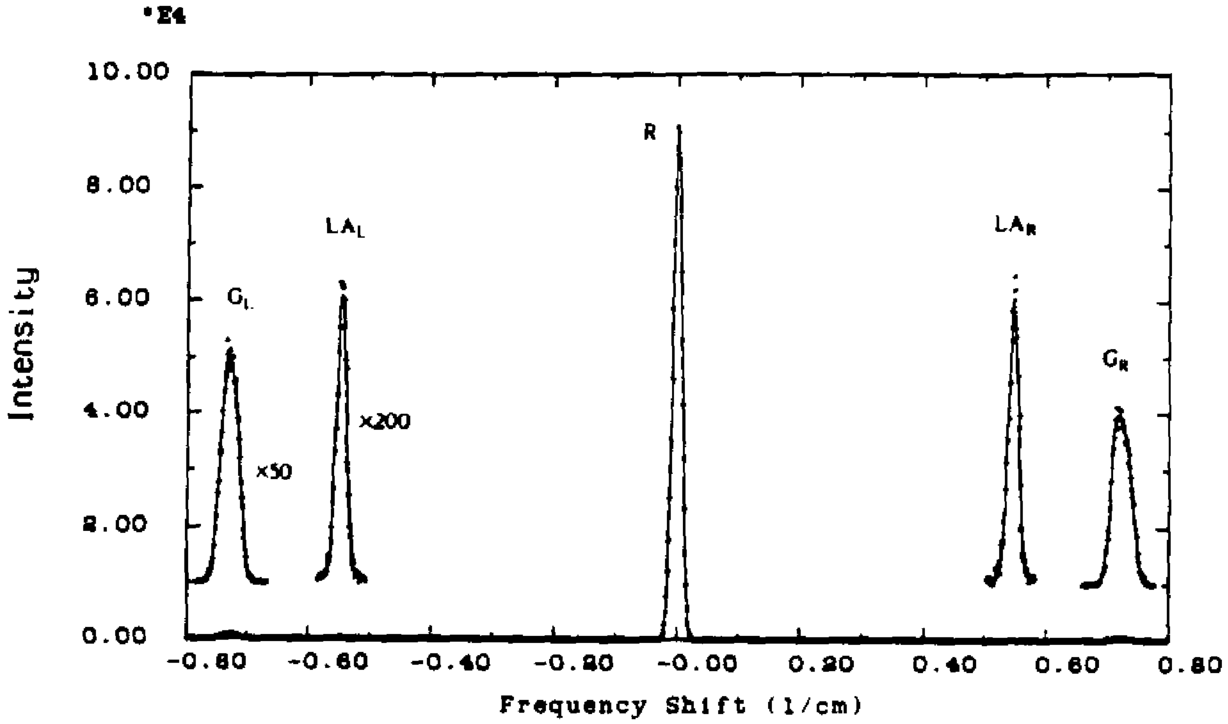

Figure 3.2.1. Room temperature 90° Brillouin scattering spectrum of K_2SeO_4 with (a+c)(b,T)(a−c) scattering geometry. The G_L and G_R are enlarged by ×50, and the LA_L and LA_R are enlarged by ×200. The points are the experimental spectrum and the solid lines are the fitted results

In most cases, all the components in a spectrum, such as the spectrum of figure 3.2.1, are well separated because of the high resolution, high suppression of neighboring orders and high contrast of the TFPI system. To analyze the spectrum, we therefore can apply the above fitting to each of the components separately.

a). In the fitting program, we first locate the central position of the Rayleigh peak (R) by fitting it with a Gaussian distribution function. This peak position is used as the zero frequence shift point, or the origin of the spectrum.

b). Second, we determine the FSR of the spectrum by using the G_L and G_R components. Because G_L and G_R each consist of two ghosts as discussed above, we fit each of them with a two Gaussian distribution function. The inner pair of ghosts are selected to define the FSR which corresponds to the separation of the FPI in the TFPI with $FSR = \frac{1}{2L_1}$ in units of cm^{-1}.

c). Finally, we carry out the convolution fittings to each of the Brillouin components. Because the instrumental response (R) is very narrow, the convolution of equation (3.2.2) only needs to integrate over a narrow range around the peak position of the instrumental response. As a good approximation, we use a range of $\pm 3 \times HWHM_R$ (half width at the half maximum of the Rayleigh peak) around the $\bar{I}_{max}$ position in which the transmission of the instrumental response decreases from the $\bar{I}_{max}$ to a value of less than $\bar{I}_{max}/1000$. In the calculations of the convolution, we replace the integral with a summation so that we can directly use the stored digital values of the Rayleigh peak as $\bar{I}(\omega)$ in the integral. This substitution has two advantage: first it takes much less CPU time, second it eliminates the error in the $\bar{I}(\omega)$ function found from the Gaussian fitting to the Rayleigh peak.

The solid lines in figure 3.2.1 are the fitted results to the experimental spectrum. The CPU time used for the fitting in a VAX/780 is about 10 minutes. The results given by the fitting for this spectrum are: $HWHM_R$ = 261MHz, the full width at the half maximum of the deconvoluted Brillouin components $FWHM_B = \gamma$ = 86MHz, and the frequency shift of the Brillouin components $\Delta\nu_B$ = 16.40GHz.

3. EXPERIMENTAL RESULTS

In Brillouin scattering, the frequency shift $\Delta\nu_i$ of the scatted light is connected to the sound velocity v_i by the relation of [C6]

$$\Delta\nu_i = v_i \frac{\sqrt{2}(n_I^2+n_S^2)^{1/2}}{\lambda_0} \sin(\frac{\theta}{2}), \tag{3.3.1}$$

where λ_0 is the wavelength of the laser light, n_I and n_S the refractive indices of the medium for the incident and scatted light respectively and θ the scattering angle. For an orthorhombic system, the velocity v_i of a longitudinal or transverse sound wave along the crystal axes is related to the component of the elastic constants C_{ii} by

$$v_i = \sqrt{C_{ii}/\rho_m}, \quad (i = 1,....,6) \tag{3.3.2}$$

where ρ_m is the density of the medium. By substituting equation (3.3.2) into equation (3.3.1), we obtain

$$C_{ii} = \frac{\rho_m}{2(n_I^2+n_S^2)} \left[\frac{\Delta\nu_i \lambda_0}{\sin(\frac{\theta}{2})} \right]^2 . \tag{3.3.3}$$

The room-temperature values of ρ_m and n_i (i=1,2,3) are given in chapter 1. Experimental results [K3] indicate that in the temperature range of interest, the density varies by $\leqslant$1.5% and this variation may be partially compensated by the variation of the refractive indices. Therefore in the following calculations, ρ_m and n_i are assumed to be constants and to have their room-temperature values.

The K_2SeO_4 crystals used in our experiments were grown by G. Hauret at the University d'Orleans from 99% stock material (Alfa products, Danvers, Mass.) which was recrystallized twice for purification. They were oriented, cut, and polished at the university P. and M. Curie in Paris by N. Lenain

a. C_{33} longitudinal acoustic mode

In the studies of the anomalies of the C_{33} longitudinal acoustic phonon, 90° and 180° (back) scattering experiments were performed. Two crystals approximately 6mm on each side were used. For 90° scattering, the crystal was cut with faces perpendicular to **b**, **a+c**, and **a−c**, and the scattering geometry was **(a+c)[b,T](a−c)**. For back-scattering, the crystal was cut with faces perpendicular to the crystal axes, and the scattering geometry was **c[a,T](−c)**.

Figure 3.3.1 shows three 90° Brillouin scattering spectra at T=300, 127.5 and 81K. The broadening of the Brillouin components is visible at T=127.5 which is around the transition temperature.

The elastic constant C_{33} and the damping constant γ_{33} found from 90° and 180° scattering data are shown in figures 3.3.2 and 3.3.3 respectively. As part of a joint program, back-scattering was also performed at the university of P. and M. Curie in Paris. Their results are correspondingly plotted in figure 3.3.3. In agreement with the reported Brillouin results [H2][L4], the C_{33}'s of both 90° and 180° scattering show rounded-step decreases ($\approx$25%) around T_i and gradual increases below T_i. The damping constants γ_{33}'s also show remarkable increases around T_i with their maxima occurring slightly above

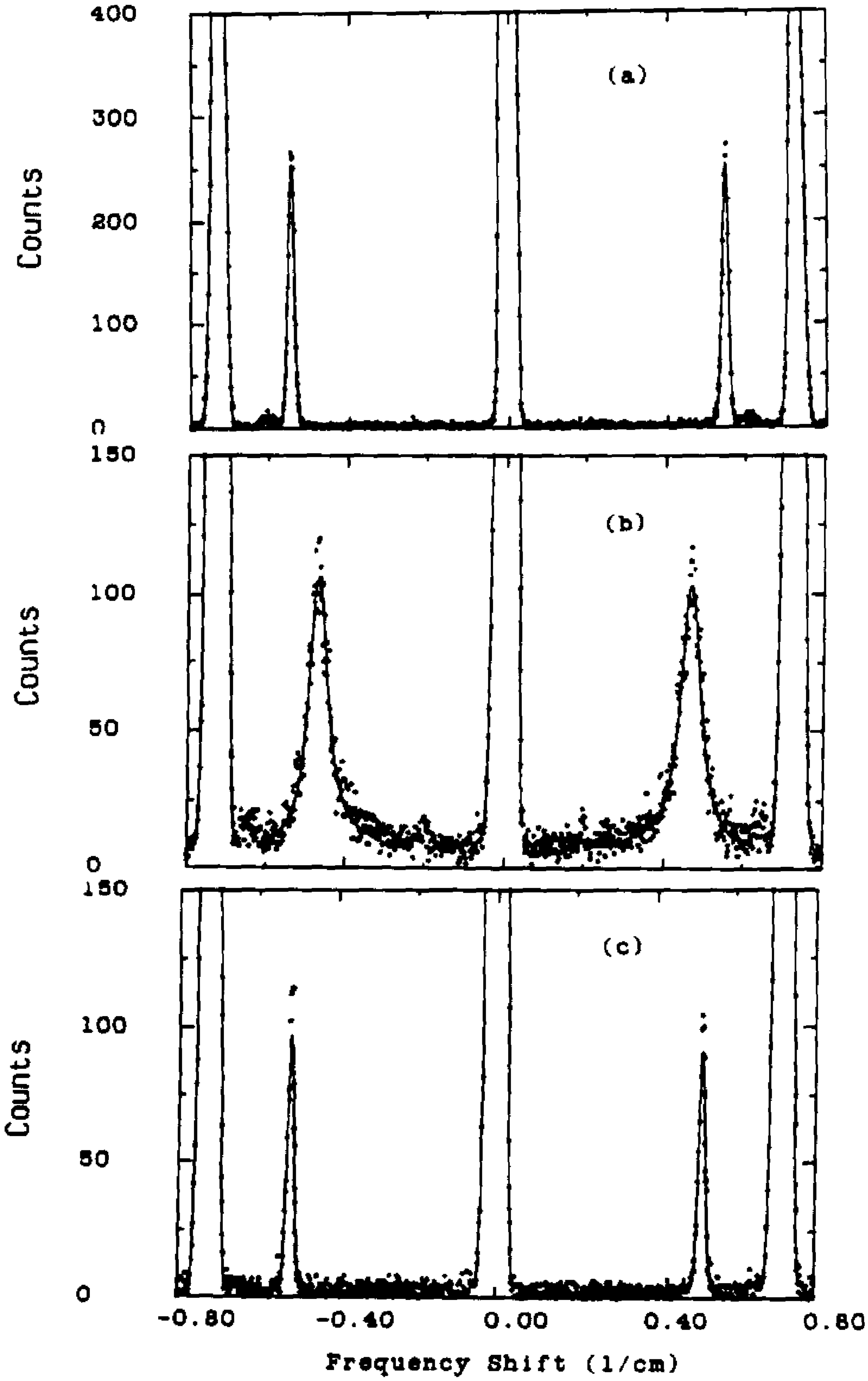

Figure 3.3.1. 90° Brillouin scattering spectra of K_2SeO_4 in the (a+c)(b,T)(a−c) scattering geometry at the temperatures of: (a) 300K, (b) 127.5K and (c) 81K showing the temperature dependence of the C_{33} longitudinal acoustic mode.

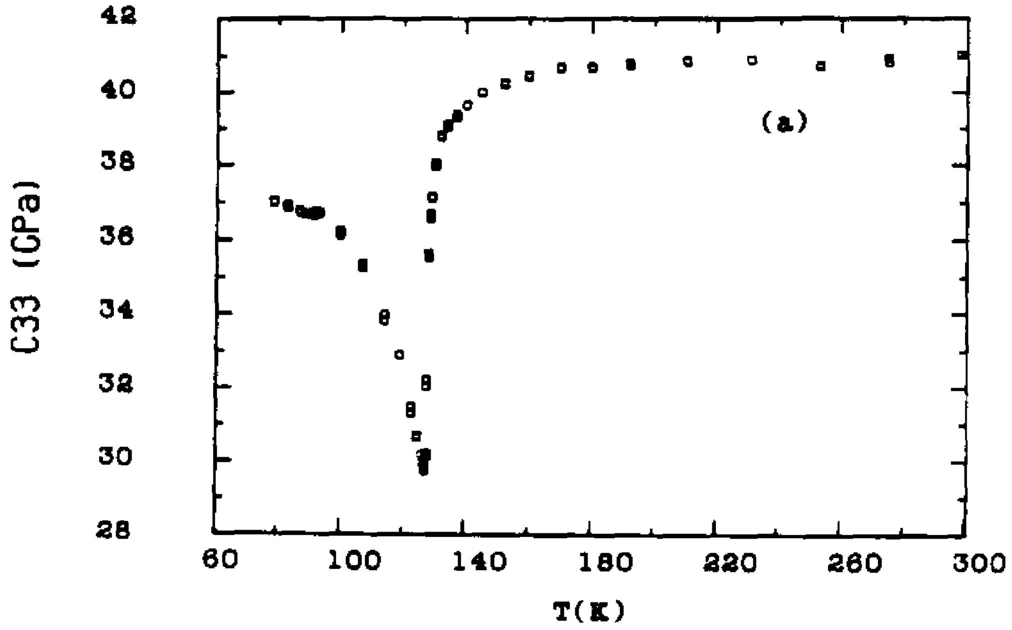

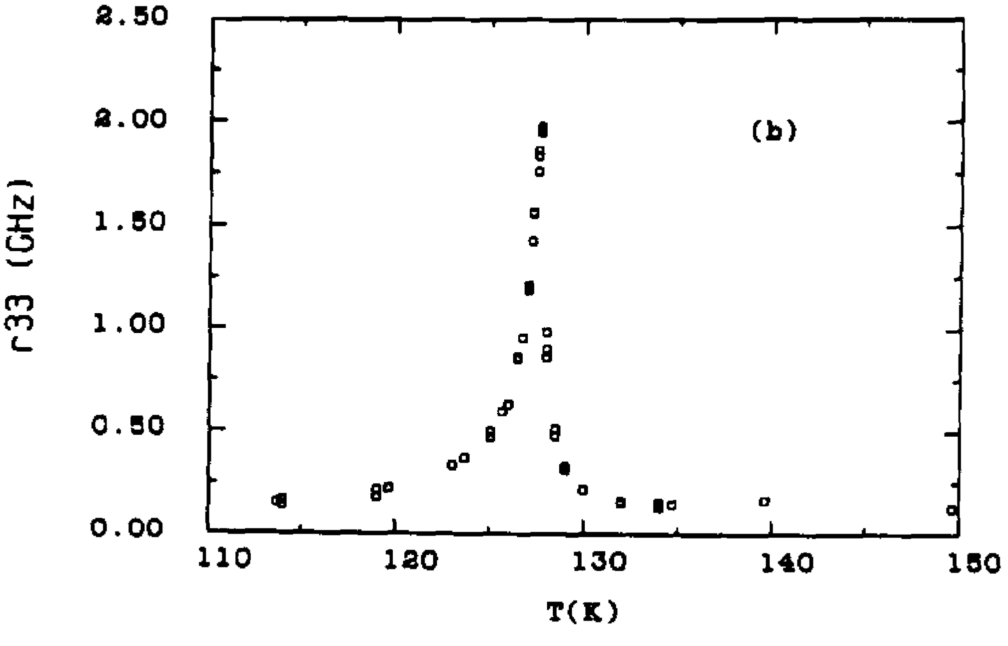

Figure 3.3.2. Temperature dependences of the elastic constant C_{33} (a) and the damping constant γ_{33} (b) of K_2SeO_4 from the 90° Brillouin scattering with damped harmonic oscillator fits.

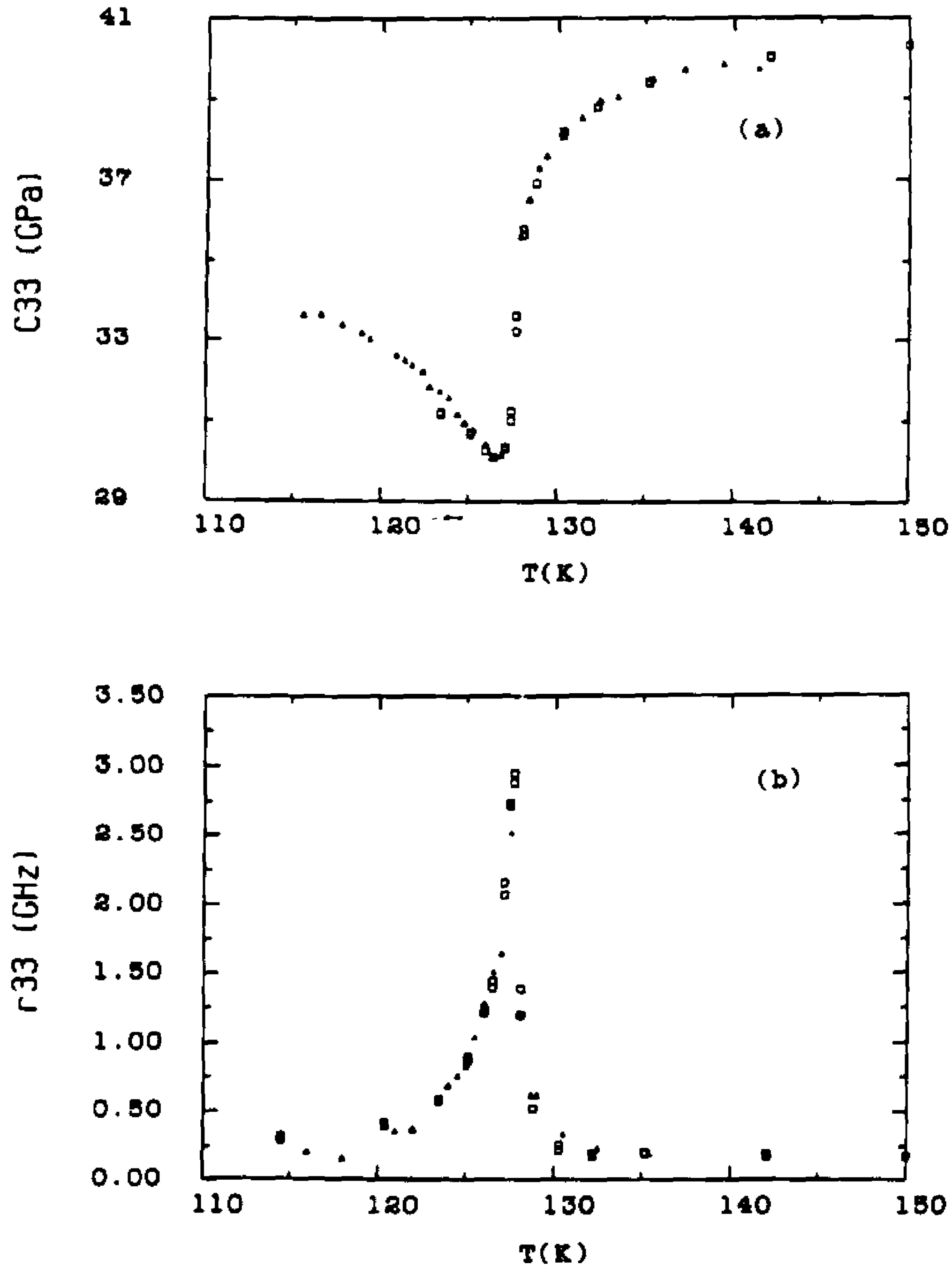

Figure 3.3.3. Temperature dependences of the elastic constant C_{33} (a) and the damping constant γ_{33} (b) of K_2SeO_4 from the 180° Brillouin scattering. Squares–data of ours (NY), triangles–data from Paris.

the minima of the corresponding C_{33}. The maximum of the γ_{33} curve increases with scattering angle, showing a strong q dependent behavior. The average accuracies for C_{33} and γ_{33} are estimated to be 0.3GPa and 100 MHz respectively.

b. C_{44}, C_{55} and C_{66} transverse modes

Brillouin scattering investigations of the C_{44}, C_{55} and C_{66} transverse modes has not been successfully carried out before by other groups because of their very small scattering cross sections. By using our high resolution and high contrast Sandercock TFPI system, we are able to detect the weak Brillouin signals from these transverse modes and follow their temperature dependences. Figure 3.3.4 shows two room-temperature Brillouin spectra of K_2SeO_4 collected in 90°, VV+VH (a) and VH (b) scattering scattering geometries. The strong LA components in the spectrum (a) correspond to the C_{33} longitudinal mode and the weak TA components correspond to the C_{55} transverse mode. In the depolarized scattering spectrum (b), the LA components are eliminated (except the ≈2% leaking from the imperfect polarizer) while the TA components are shown clearly.

To investigate all six transverse modes with **q** along the crystal axes, three K_2SeO_4 samples with different crystal cuts are used. The sizes of the samples are about 6mm on each side. They are cut so that each of them has two surfaces perpendicular to a different crystal axis (**a** or **b** or **c**) and four other faces perpendicular to the diagonal directions of the other two crystal axes. All the Brillouin scattering measurements were performed in a 90° depolarized (VH) geometry. The laser was operated at the wavelength of 4880Å with output power of 250mW. The collection time for each spectrum varied from 1/2 hour to 10 hours.

Figures 3.3.5 and 3.3.6 show the temperature dependences of the elastic constants and the deconvoluted FWHM's (damping constants) deduced from the Brillouin scattering components of these six transverse modes. For the pair of the C_{44} and γ_{44}, we use squares to represent the results of the transverse mode propagating along **b** direction and polarized along c direction (**q**//**b**, **u**//**c**) and triangles to represent the results of the other C_{44} transverse mode (**q**//**c**, **u**//**b**) with interchanged **q** and **u** directions from the first one. In the same way, we denote the results of the pair C_{55} modes with: squares - (**q**//**a**, **u**//**c**), triangles - (**q**//**c**, **u**//**a**); and C_{66} modes with: squares - (**q**//**a**, **u**//**b**), triangles - (**q**//**b**, **u**//**a**). When the temperature approached T_c from above, the Brillouin scattering intensity of the C_{55} transverse modes decreased dramatically, making further low temperature measurements impossible. The weakness of the transverse mode Brillouin signals causes uncertainties in determining the frequency shifts and the damping constants. The accuracies for the elastic constants and the attenuations are estimated as 0.3GPa and 100MHz respectively around room-temperature and 0.6GPa and 200MHz at low temperatures.

As can be seen from figures 3.3.5 and 3.3.6, within the experimental accuracies, there is no distinguishable asymmetry in the C_{ii} and γ_{ii} for the pairs of transverse modes under interchange of their propagation and polarization directions.

A comparison of our hypersonic shear stiffnesses C_{44}, C_{55} and C_{66} with the results of Rehwald et al.[R1] shows that our results are similar to their ultrasonic results, but somewhat different from their hypersonic results indirectly obtained by using the stiffness functions of pure longitudinal, quasi-longitudinal and quasi-transverse phonons.

Of the measured shear elastic constants, only C_{44} shows pronounced variations around the T_i temperature with a gradual decrease of about 40% when

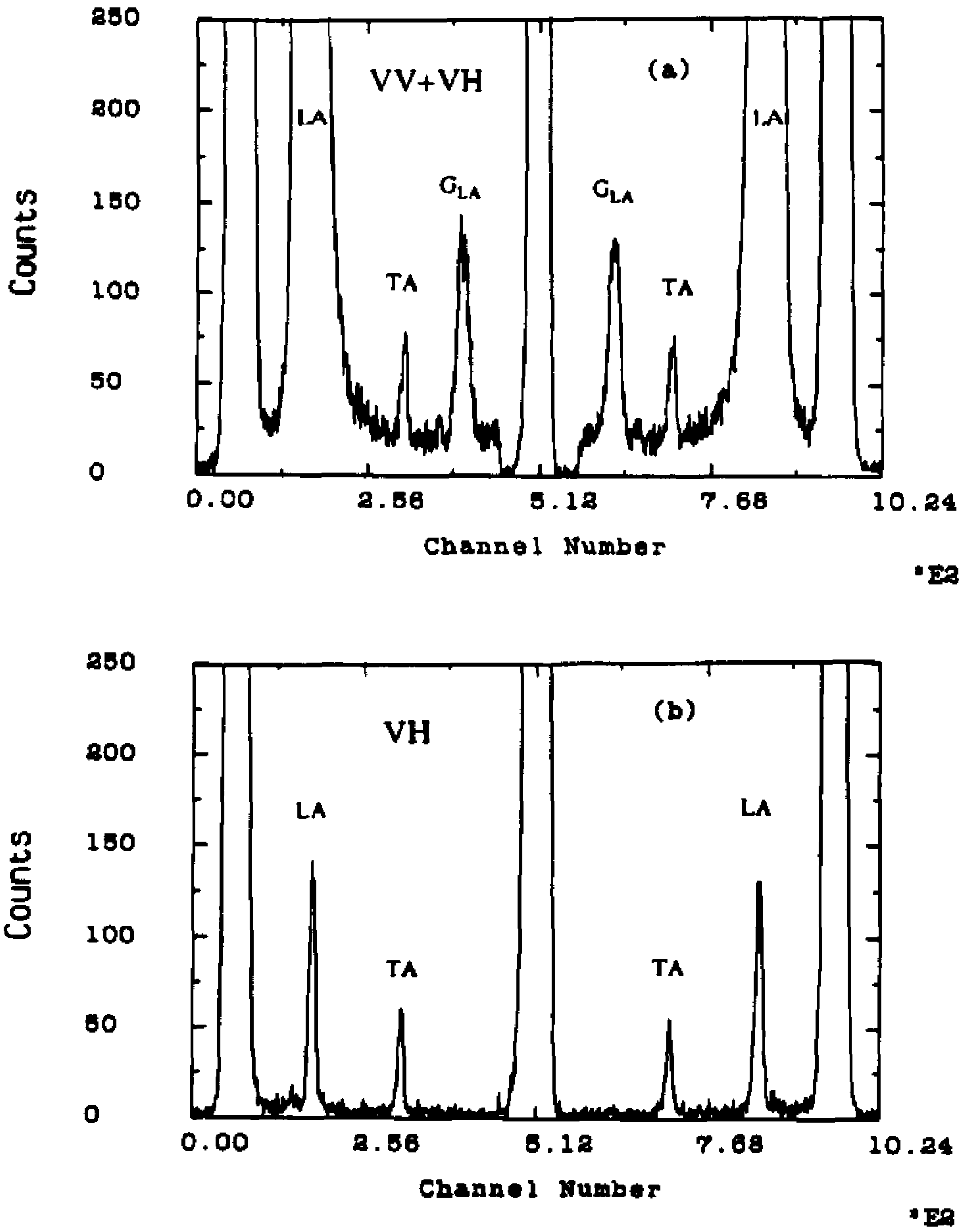

Figure 3.3.4. Room temperature 90° Brillouin scattering spectra of K_2SeO_4 in the scattering geometries of: (a) (b—c)[a, T](b+c); (b) (b—c)[a, b—c] (b+c). The notations LA, TA and G_{LA} represent the longitudinal components, transverse components and the ghosts (neighboring order) of the LA components. The LA components in (b) are the leakages.

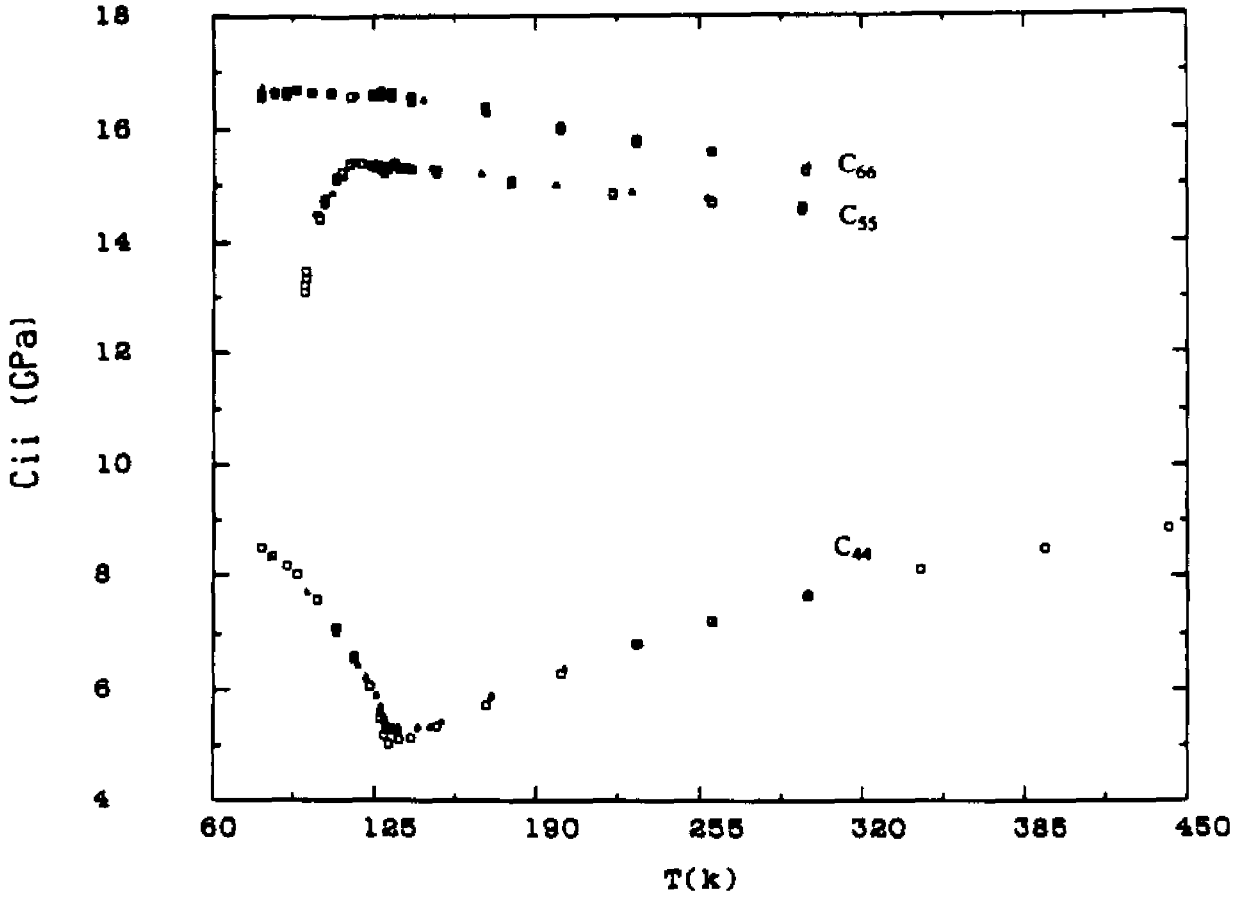

Figure 3.3.5. Temperature dependences of the shear elastic constants from 90° Brillouin scattering. The corresponding transverse modes are represented with: for C_{44}, squares - (q//b, u//c), triangles - (q//c, u//b); for C_{55}, squares - (q//a, u//c), triangles - (q//c, u//a); for C_{66}, squares - (q//a, u//b), triangles - (q//b, u//a).

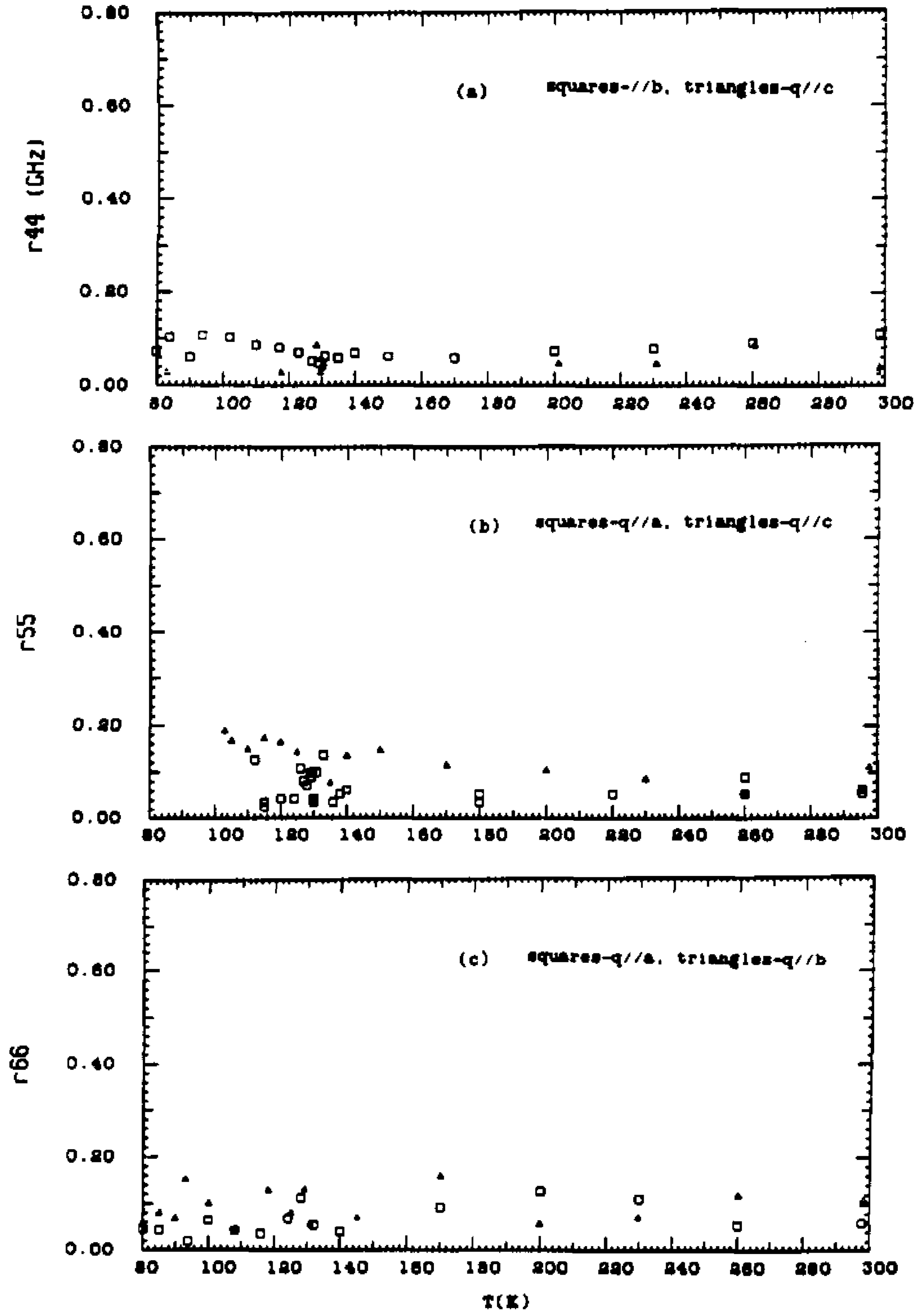

Figure 3.3.6. Temperature dependences of the transverse mode damping constants from 90° Brillouin scattering. The corresponding transverse modes are represented with: (a) γ_{44}, squares - (q//b, u//c), triangles - (q//c, u//b); (b) γ_{55}, squares - (q//a, u//c), triangles - (q//c, u//a); (c) γ_{66}, squares - (q//a, u//b), triangles - (q//b, u//a).

the temperature approaches T_i from both sides. Only C_{55} shows an anomaly around T_c with a significant decrease when the temperature approaches T_c above. Of all the measured damping constants, no countable anomaly was observed within the experimental accuracy.

Figure 3.3.7 shows the temperature dependences of the integrated Brillouin scattering intensities (I_{44}, I_{55} and I_{66}) of the C_{44}, C_{55} and C_{66} transverse modes. They are obtained by integration over the area of the corresponding Brillouin components and normalization with the laser power and collection time. The accuracy of these values is estimated to be about 20%. As shown in figure 3.3.7, the Brillouin scattering intensity of the C_{44} mode exhibits unusual changes on both sides of T_i, and the C_{55} mode when approaching T_c. To explore the intrinsic properties, we plot in figure 3.3.8 the temperature dependences of P_{ii} with

$$P_{ii} = (I_{ii}C_{ii}/\ T)^{1/2}, \tag{3.3.4}$$

in which the P_{ii} are proportional to the elasto-optic (Pockels's) coefficients. The figure shows clearly that while P_{66} is temperature independent, P_{44} is temperature dependent with a variation opposite to that of C_{44}, and P_{55} is also temperature dependent in the incommensurate phase with a variation similar to that of C_{55}, though it is temperature independent in the normal phase.

The analysis and discussions of these experimental results will be given in the later chapters in which we will discuss the longitudinal C_{33} mode and the transverse modes separately.

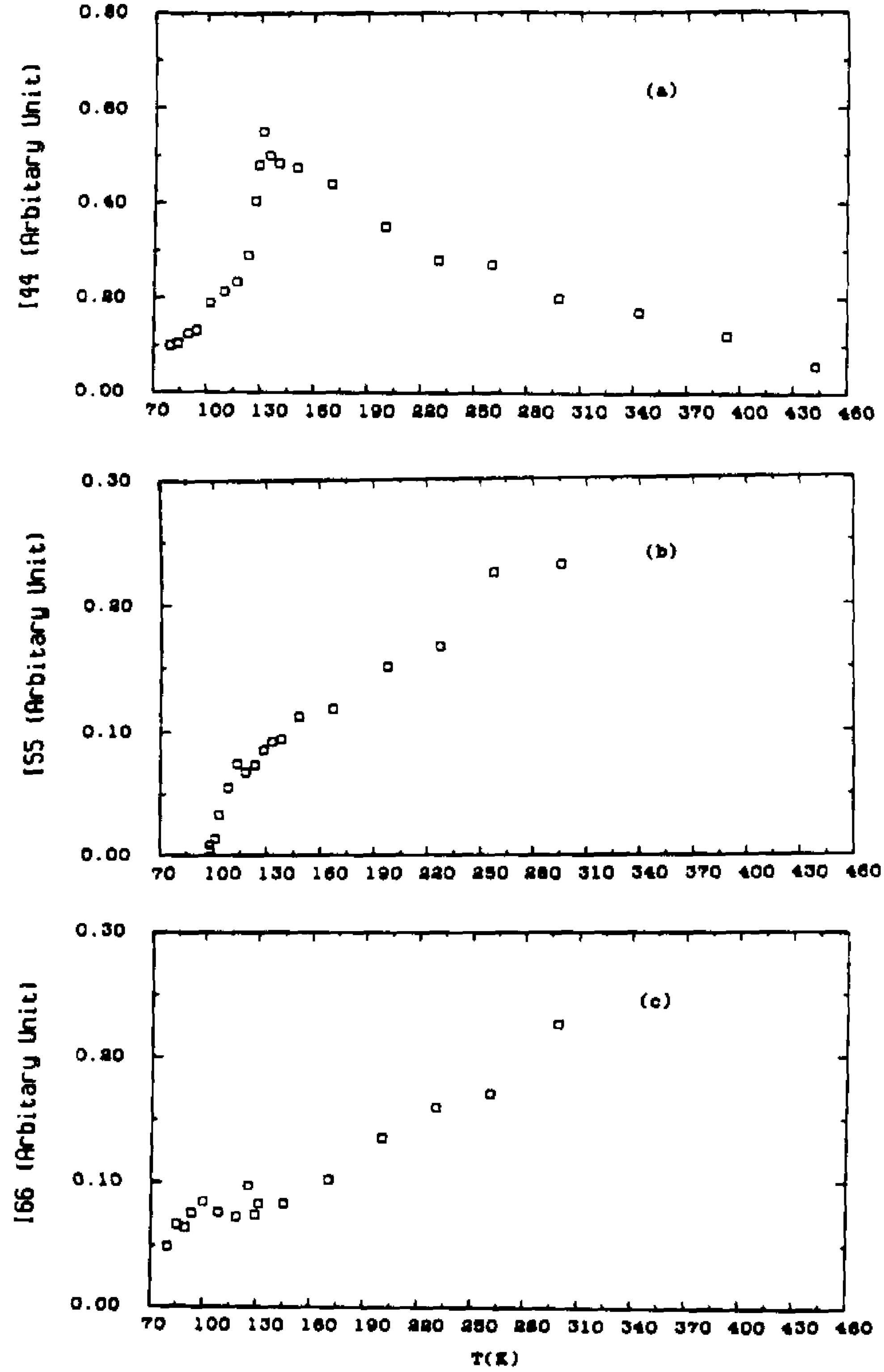

Figure 3.3.7. Temperature dependences of the integrated Brillouin scattering intensities: (a) C_{44} transverse mode - I_{44}; (b) C_{55} transverse mode - I_{55} and (c) C_{66} transverse mode - I_{66} in arbitrary unit.

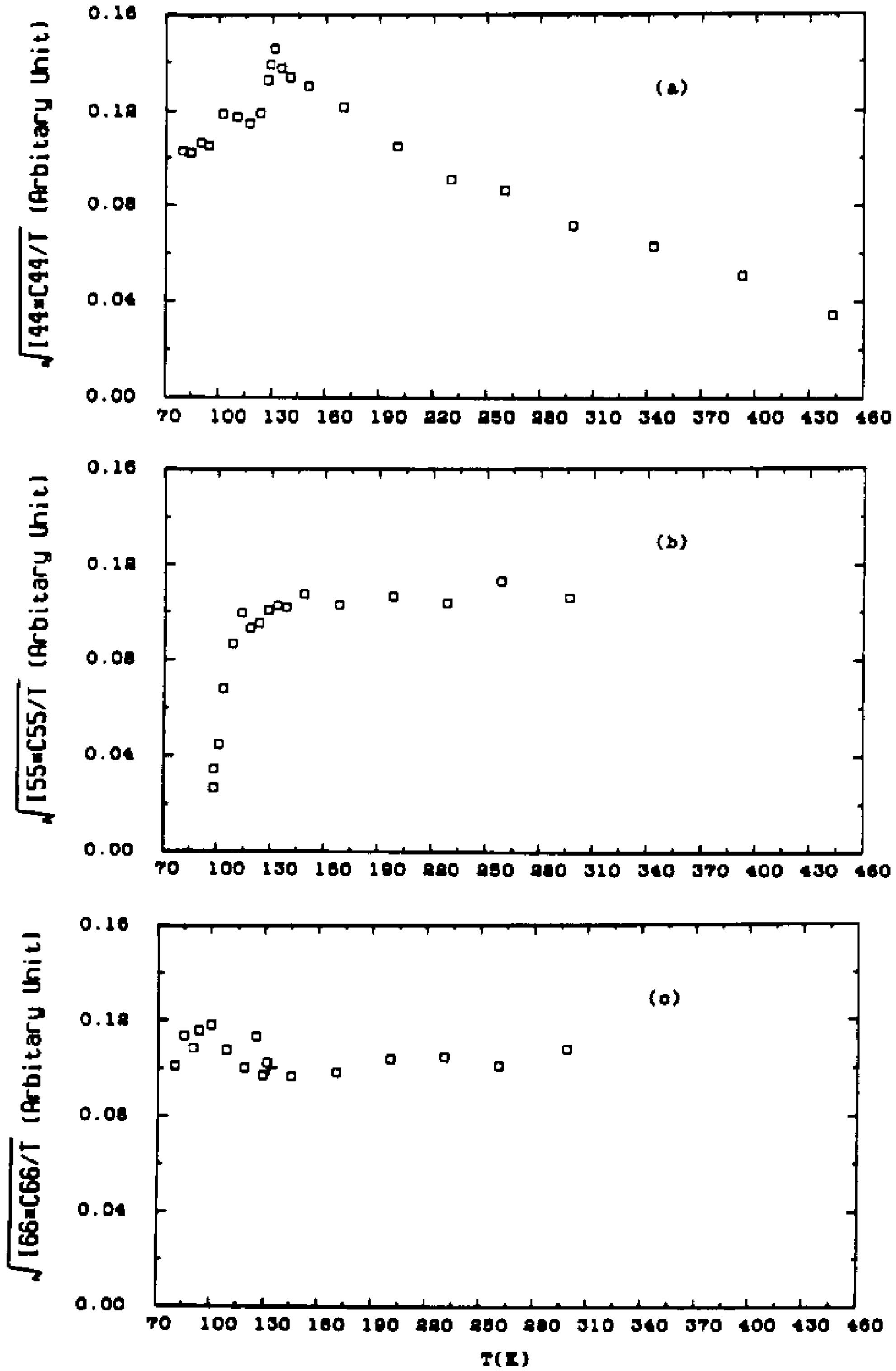

Figure 3.3.8. Temperature dependences of the $P_{ii} = \sqrt{I_{ii}C_{ii}/T}$,(a) from C_{44}, (b) from C_{55} and (c) from C_{66} transverse modes.

CHAPTER IV

ELASTIC ANOMALY OF C_{33} LONGITUDINAL ACOUSTIC MODE AROUND T_i

In this chapter we present a self-consistent theoretical analysis of the C_{33} longitudinal acoustic anomaly of K_2SeO_4 in the vicinity of the incommensurate phase transition based on the framework of Landau theory. Much of the material presented in this chapter has been recently published in Physical Review B[L17].

1. THE LANDAU FREE ENERGY

The phenomenological Landau theory has been extended and widely applied in describing structurally incommensurate phases and the phase transitions with great success. For K_2SeO_4, two kinds of Landau free energy expressions are generally used. Although they are essentially equivalent, each of them has advantages in describing some of the incommensurate characteristics. The complete form of the free energy most widely used is an expansion in the complex commensurate normal-mode coordinate, Q_{q_c}, whose phase and amplitude are assumed to be continuous slowly varying functions of position. This kind of free energy has been extensively discussed by many authors [L9][S6][B4][I4][S5]. It includes the gradient term which guarantees that the equilibrium state is homogeneous, and the Lifshiz invariant term which provides a natural explanation for the occurrence of the incommensurate phase. Another expression for the free energy is a normal-mode expansion in which the order parameters are the complex normal-mode amplitudes, Q_q, of the Σ_2 soft optical branch. This form of the free energy has the advantage for analyzing the lattice dynamics in the incommensurate phase. The existence of two new excitations, the amplitudon and phason, in the incommensurate phase is a natural result of this free energy. Detailed reviews of this normal-mode expansion free energy have been given by Axe [A2], Dovrak et al.[D2] and Bruce et al.[B3]. We will show that under certain approximations, both free energies can be reduced to a simple form which is valid in the vicinity of T_i and has been widely used.

a. Complete form of the Landau free energy

The Landau free energy density function for incommensurate K_2SeO_4 can be constructed according to the crystal symmetry in the normal and commensurate phase. It can be expressed as a sum of three parts:

$$f(x) = f_Q(x)+f_\epsilon(x)+f_P(x), \tag{4.1.1}$$

where $f_Q(x)$ includes terms only containing the order parameter $Q(x)$ which is the complex position-dependent amplitude of the Σ_2 mode at the commensurate wavevector $\mathbf{q}_c = \frac{\mathbf{a}^*}{3}$, $f_\epsilon(x)$ includes terms in the strains ϵ_i (i=1-6) both alone and in combination with Q, and $f_P(x)$ includes terms in the polarization P_z both alone and in combination with Q. Each of them can be expressed as:

$$f_Q = \frac{1}{2}\alpha QQ^*+\frac{1}{4}\beta(QQ^*)^2+\frac{1}{6}\gamma_1'(QQ^*)^3-i\frac{1}{2}\sigma\left(Q\frac{dQ^*}{dx}-Q^*\frac{dQ}{dx}\right)$$

$$+\frac{\kappa}{2}\frac{dQ^*}{dx}\frac{dQ}{dx}+\frac{1}{2}\gamma'(Q^6+Q^{*6}), \tag{4.1.2a}$$

$$f_P = \frac{1}{2\chi_o}P^2+\frac{1}{2}\eta P^2QQ^*+\xi P(Q^3+Q^{*3})-PE, \tag{4.1.2b}$$

$$f_\epsilon = \frac{1}{2}\sum_{i,j=1}^{6} C_{ij}^o\epsilon_i\epsilon_j-\sum_{i=1}^{3} h_i\epsilon_i QQ^*+\sum_{i,j=1}^{3} g_{ij}\epsilon_i\epsilon_j QQ^*$$

$$+\sum_{i=4}^{6} g_i \epsilon_i^2 QQ^* + \frac{1}{2} a_5 \epsilon_5 (Q^3 + Q^{*3}) - \sum_{i=1}^{6} \epsilon_i \sigma_i, \qquad (4.1.2c)$$

where, according to the usual Landau assumption, only the coefficient α is temperature dependent with

$$\alpha = \alpha_0 (T - T_0), \qquad (4.1.3)$$

and all the other coefficients are assumed to be temperature independent.

This form of free energy has the great advantage of describing both the incommensurate and lock-in transitions as well as the evolution of the modulation wave from the sinusoidal regime near T_i to the multi-soliton regime near T_c in the incommensurate phase. But it does not naturally include dynamics. to apply the free energy for the elastic anomalies around T_i, we will show that it can be simplified to a simple form under certain approximations. First, we make the usual transformation to polar coordinates $Q = \rho e^{i\phi(x)}$ and invoke the continuum constant-amplitude approximation $\frac{d\rho}{dx} = 0$. Equations (4.1.2a), (4.1.2b) and (4.2.2c) can then be rewritten as:

$$f_Q = \frac{1}{2} \alpha \rho^2 + \frac{1}{4} \beta \rho^6 + \frac{1}{6} \gamma_1' \rho^6 - \sigma \rho^2 \frac{d\phi}{dx} + \frac{1}{2} \kappa \rho^2 \left(\frac{d\phi}{dx}\right)^2 + \gamma' \rho^6 \cos 6\phi, \qquad (4.1.4a)$$

$$f_P = \frac{1}{2\chi_0} P^2 + \frac{1}{2} \eta P^2 \rho^2 + 2\xi P \rho^3 \cos 3\phi - PE, \qquad (4.1.4b)$$

$$f_\epsilon = \frac{1}{2} \sum_{i,j=1}^{6} C_{ij}^o \epsilon_i \epsilon_j - \sum_{i=1}^{3} h_i \epsilon_i \rho^2 + \sum_{i,j=1}^{3} g_{ij} \epsilon_i \epsilon_j \rho^2$$

$$+\sum_{i=4}^{6} g_i \epsilon_i^2 \rho^2 + a_5 \epsilon_5 \rho^3 \cos 3\phi - \sum_{i=4}^{6} \epsilon_i \sigma_i. \qquad (4.1.4c)$$

Since we will not consider the polarization P, we minimize the average free energy density $F = (\frac{1}{L}) \int_0^L f(x) dx$ with respect to P and find the equilibrium value:

$$P = \chi_o'(E-2\xi\rho^3\cos 3\phi), \tag{4.1.5}$$

where

$$\chi_o' = \frac{1}{\frac{1}{\chi_o}+\eta\rho^2},$$

Assuming that the electric field E and the stresses σ_i are zero, we eliminate P from f(x) and find:

$$f_P = \chi_o'\xi^2\rho^6(1+\cos 6\phi), \tag{4.1.6}$$

where we have made use of the identity

$$\cos^2(\frac{n\phi}{2}) = \frac{1+\cos(n\phi)}{2}.$$

It can be seen that the terms in $f_b(x)$ can be absorbed into the sixth order terms of $f_Q(x)$, resulting a modification of the coefficients of γ_1' and γ'. In this way the free energy can be considerably simplified.

The xz elastic strain ϵ_5 has the same symmetry as the phason and, therefore, will have interaction through the term $\frac{1}{2}a_5\epsilon_5(Q^3+Q^{*3})$. However, the interaction has a strong effect only near T_c; for the temperature around T_i, the effect is small, so we drop this term. For the purpose of describing the longitudinal elastic anomalies around T_i, we ignore all terms in strains ϵ_4, ϵ_5, ϵ_6 and the off-diagonal components of g_{ij}. Then the approximate form of f(x) is:

$$f(x) = \frac{1}{2}\alpha\rho^2+\frac{1}{4}\beta\rho^4+\frac{1}{6}\gamma_1\rho^6-\sigma\rho^2\frac{d\phi}{dx}+\frac{1}{2}\kappa\rho^2(\frac{d\phi}{dx})^2+\gamma\rho^6\cos(6\phi)$$

$$+\frac{1}{2}\sum_{i,j=1}^{3}C_{ij}^{o}\epsilon_i\epsilon_j-\sum_{i=1}^{3}h_i\epsilon_i\rho^2+\sum_{i=1}^{3}g_i\epsilon_i^{\,2}\rho^2, \tag{4.1.7}$$

where

$$\gamma_1 = \gamma_1'-6\chi_o'\xi^2, \tag{4.1.8a}$$

$$\gamma = \gamma' - \chi_o' \xi^2. \tag{4.1.8b}$$

A further simplification can be achieved by minimizing the average free energy density $F = \frac{1}{L}\int_o^L f(x)dx$ with respect to ϕ in the constant-amplitude approximation. The Euler-Largrange equation

$$\frac{d}{dx}\frac{\partial f}{\partial(\frac{\partial\phi}{\partial x})} - \frac{\partial f}{\partial\phi} = 0, \tag{4.1.9}$$

yields

$$\kappa\frac{d^2\phi}{dx^2} = -6\gamma\rho^4\sin(6\phi), \tag{4.1.10}$$

which is the sine-Gorden equation. The solution of this equation indicates that when T is close to T_c in the incommensurate phase, the spatial variation of the phase ϕ of the modulation wave is soliton like, whereas when the temperature is close to T_i, $\frac{d\phi}{dx}$ tends to be constant as shown in figure 4.1.1 [B2]. In the vicinity of T_i, we take the incommensurate plane wave limit and let

$$\frac{d\phi}{dx} = q - q_c. \tag{4.1.11}$$

In this limit, equation (4.1.7) reduces to

$$f(x) = \frac{1}{2}[\alpha - 2\sigma(q-q_c) + \kappa(q-q_c)^2]\rho_2 + \frac{1}{4}\beta\rho^4 + \frac{1}{6}\gamma_1\rho^6$$
$$+\frac{1}{2}\sum_{i,j=1}^{3} C_{ij}^{o}\epsilon_i\epsilon_j - \sum_{i=1}^{3} h_i\epsilon_i\rho^2 + \sum_{i=1}^{3} g_i\epsilon_i{}^2\rho^2. \tag{4.1.12}$$

In the above free energy, ρ is the amplitude of a Σ_2 mode at the wavevector q, and thus equation (4.1.12) is the free energy of a single mode. Minimizing f(x) with respect to q gives

$$q_o = q_c + \frac{\sigma}{\kappa}. \tag{4.1.13}$$

Substituting q_o into (4.1.12), one obtains

$$f(x) = \frac{1}{2}(\alpha - \frac{\sigma^2}{\kappa})\rho^2 + \frac{1}{4}\beta\rho^4 + \frac{1}{6}\gamma_1\rho^6 + \frac{1}{2}\sum_{i,j=1}^{3} C_{ij}^{o}\epsilon_i\epsilon_j$$

$$-\sum_{i=1}^{3} h_i\epsilon_i\rho^2 + \sum_{i=1}^{3} g_i\epsilon_i^2\rho^2. \tag{4.1.14}$$

Note that the Lifshitz invariant term $-i\frac{\sigma}{2}(Q\frac{dQ^*}{dx} - Q^*\frac{dQ}{dx})$ in equation (4.1.2) shifts the minimum in the part of f(x) quadratic in ρ from $q_c = \frac{a^*}{3}$ to $q_o = q_c + \frac{\sigma}{\kappa}$. Also it increase the transition temperature from T_o where $\alpha = \alpha_o(T - T_o) = 0$ (the virtual paraelectric-commensurate transition) to $T_i = T_o + \frac{\sigma^2}{\alpha_o\kappa}$, where $(\alpha - \frac{\sigma^2}{\kappa}) = 0$. Finally, replacing $(\alpha - \frac{\sigma^2}{\kappa})$ by $A = A_o(T - T_i)$, β by B and γ_1 by D, and noting that f(x) is no longer dependent on x and is therefore identical to the average free energy, we have the final simple form of the free energy:

$$F = \frac{1}{2}A_o(T - T_i)\rho^2 + \frac{1}{4}B\rho^4 + \frac{1}{6}D\rho^6 + \frac{1}{2}\sum_{i,j=1}^{3} C_{ij}^{o}\epsilon_i\epsilon_j$$

$$-\sum_{i=1}^{3} h_i\epsilon_i\rho^2 + \sum_{i=1}^{3} g_i\epsilon_i^2\rho^2. \tag{4.1.15}$$

This form of the free energy is advantageous for calculating the thermodynamic properties in the vicinity of T_i. It includes the main contributions from the amplitude of the order parameter which is the amplitude of the condensed soft optical mode on the Σ_2 branch with wavevector q_o. We will evaluate the coefficients appearing in this approximate free energy expression in the static equilibrium limit.

Although this form of the free energy can be extended to analyze the interaction of acoustic phonons with the order parameter dynamics [Y5], it lacks some important dynamic information. Note that originally the complex order parameter Q is two dimensional (amplitude and phase), whereas the one in the free energy (4.1.15) is only the amplitude ρ of the order parameter (the incommensurate condition provides that the free energy of the equilibrium state is independent of the phase angle ϕ and the equilibrium state is thus continuously degenerate [B3]). Also it does not include the dynamic information required to describe the degeneracy of the soft modes at (q_o+q) and $(-q_o+q)$ in the paraelectric phase and the lifting of the degeneracy in the incommensurate phase because of the change of the symmetry. To obtain this information for the dynamic calculation of the acoustic phonon - soft mode interactions, we need to consider the free energy density written directly as an expansion in normal mode coordinates.

b. Free energy in normal mode expansion

We know that the incommensurate phase transition of K_2SeO_4 is driven by the condensation of the soft optical mode of $q = q_o$ on the Σ_2 branch. To investigate the dynamic properties of the soft modes, we should use a free energy density expressed directly in normal mode coordinates. For easy discussion, we write it in the form of

$$F = F_Q+F_\epsilon+F_c, \tag{4.1.16}$$

where F_Q is the part of the free energy which depends only on the normal mode coordinates, $Q(q)$, on the Σ_2 branch where the modes at q_o and $-q_o$ become critical at T_i, F_ϵ is the purely elastic contribution, and F_c is the part which includes coupling between the normal modes and the elastic strains in which we will only consider the lowest order contributions. All contributions of the polarization P are neglected. The three parts of the free energy can be written as

$$F_Q = \frac{1}{2}\sum_{q_1,q_2} \Omega^2(q_1)Q(q_1)Q(q_2)\delta(q_1+q_2)+\frac{1}{6}\sum_{q_1\ldots q_4} BQ(q_1)\ldots Q(q_4)\delta(q_1+\ldots+q_4)$$

$$\frac{1}{15}\sum_{q_1\ldots q_6} DQ(q_1)\ldots Q(q_6)\delta(q_1+\ldots+q_6), \qquad (4.1.17a)$$

$$F_\epsilon = \frac{1}{2}\sum_{q_1,q_2}\sum_{i,j=1}^{3} C_{ij}^{o}\epsilon_i(q_1)\epsilon_j(q_2)\delta(q_1+q_2), \qquad (4.1.17b)$$

$$F_c = -\sum_{q_1\ldots q_3}\sum_{i=1}^{3} h_i\epsilon_i(q_1)Q(q_2)Q(q_3)\delta(q_1+\ldots+q_3)$$

$$+\sum_{q_1\ldots q_4}\sum_{i=1}^{3} g_i\epsilon_i(q_1)\epsilon_i(q_2)Q(q_3)Q(q_4)\delta(q_1+\ldots+q_4). \qquad c(4.1.17c)$$

In this expression, it is understood that $Q(q)$, the normal coordinate of a mode on the Σ_2 branch, is considered only for q in the vicinity of q_o or $-q_o$. Furthermore, we have neglected the wavevector variation of the coefficients of B, D, C_{ij}^o, h_i and g_i. Only Ω is temperature and wavevector dependent and is defined as

$$\Omega^2(q) = A_o(T-T_i)+\frac{1}{2}\sum_{\alpha,\beta}\Lambda_{\alpha\beta}(q\pm q_o)_\alpha(q\pm q_o)_\beta, \qquad (4.1.18)$$

where the ± sign depends on the proximity of q to q_o or $-q_o$ and $\Lambda_{\alpha\beta}$ is a symmetric tenser with the full orthorhombic symmetry. In the lowest order approximation, we write it as

$$\Lambda = \begin{vmatrix} \Lambda_x & 0 & 0 \\ 0 & \Lambda_y & 0 \\ 0 & 0 & \Lambda_z \end{vmatrix}.$$

This free energy is written in the variables relevant to $T>T_i$; it contains both equilibrium and dynamic components. The equilibrium components can be obtained by dropping all terms in the sums on **q** except those for which all $\mathbf{q}_i$ are equal to $\pm\mathbf{q}_0$ for the normal mode coordinates $Q(\mathbf{q}_i)$ and all $\mathbf{q}_i$ are equal zero for the strains $\epsilon(\mathbf{q}_i)$. By setting

$$Q(\mathbf{q}_0) = \frac{1}{\sqrt{2}}\rho e^{i\phi}, \tag{4.1.19}$$

one can obtain

$$F = \frac{1}{2}\Omega^2(\mathbf{q}_0)\rho^2+\frac{1}{4}B\rho^4+\frac{1}{6}D\rho^6+\frac{1}{2}\sum_{i,j=1}^{3}C_{ij}^{o}\epsilon_i\epsilon_j$$
$$-\sum_{i=1}^{3}h_i\epsilon_i\rho^2+\sum_{i=1}^{3}g_i\epsilon_i^2\rho^2, \tag{4.1.20}$$

where, as indicated by (4.1.18)

$$\Omega^2(\mathbf{q}_0) = A_0(T-Ti).$$

Comparisons of equation (4.1.20) with equation (4.1.15) shows that the equilibrium components of the free energy (4.1.20) is identical with the simple form free energy (4.1.15).

Now we will consider the dynamic components of the free energy (4.1.17) and find the dynamic effects of the coupling between the acoustic phonons and the soft optical modes. Using equations (4.1.17), we will calculate the energy associated with the time dependent fluctuations of the normal coordinates in the presence of the static distortion $\langle Q(\pm\mathbf{q}_0)\rangle$. Following Bruce and Cowley[B3], we redefine the variables $Q(\pm\mathbf{q}_0)$ in the free energy (4.1.17) by

$$Q(\pm\mathbf{q}_0) \rightarrow \langle Q(\pm\mathbf{q}_0)\rangle+Q(\pm\mathbf{q}_0), \tag{4.1.21}$$

so that the $Q(\pm\mathbf{q}_0)$ in the right hand side always describes the fluctuating coordinators of wavevector $\pm\mathbf{q}_0$ in the normal and incommensurate phases. The static distortion is defined as

$$\langle Q(\pm\mathbf{q}_0)\rangle = \frac{\rho_0}{\sqrt{2}}e^{\pm i\phi_0},$$

where ρ_o is the equilibrium value of equation (4.1.20). The lowest order deviation of the free energy from its equilibrium value is given by

$$\delta F_Q = \sum_q [\Omega^2(\pm q_o+q)+2B\rho_o^2+3D\rho_o^4]Q(\pm q_o+q)Q^*(\pm q_o+q)$$

$$+\sum_q (B+2D\rho_o^2)\rho_o^2[e^{-i2\phi_o}Q(q_o+q)Q^*(-q_o+q)+\text{c.c.}], \tag{4.1.22a}$$

$$\delta F_c = \sum_q \sum_{i=1}^{3} g_i\rho_o^2\epsilon_i(-q')\epsilon_i(q')$$

$$-\sum_q \sum_{i=1}^{3} [h_i-g_i\epsilon_i^{o}(0)]\rho_o\epsilon_i(-q')\frac{1}{\sqrt{2}}[e^{-i\phi_o}Q(q_o+q')+e^{i\phi_o}Q(-q_o+q')]$$

$$-\sum_{q,q'} \sum_{i=1}^{3} [h_i-g_i\epsilon_i^{o}(0)]\epsilon_i(-q')Q(\pm q_o+q'+q)Q^*(\pm q_o+q), \tag{4.1.22b}$$

where c.c. is the complex conjugate. Since the structure is changed by the static distortion in the incommensurate phase, the above energy fluctuation will play a different role above and below T_i. We will discuss the two situations in turn.

1). When $T>T_i$:

Since the equilibrium conditions of equation (4.1.20) requires $\rho_o = 0$ and $\epsilon_i^{o}(0) = 0$, equations (4.1.22) can be reduced into

$$\delta F_Q = \sum_q \Omega_{\Sigma_2}^2(\pm q_o+q)Q(\pm q_o+q)Q^*(\pm q_o+q), \tag{4.1.23a}$$

$$\delta F_c = -\sum_{q,q'} h_i\epsilon_i(-q')Q(\pm q_o+q'+q)Q^*(\pm q_o+q). \tag{4.1.23b}$$

The above equations indicate that above T_i, the dynamical variables are the normal modes of the Σ_2 branch. Also, in this phase, the energy of the system can be lowered by the coupling of the acoustic phonon to pairs of soft modes around the two minima at $\pm q_o$ on the Σ_2 branch. Such a coupling may be represented by the usual bubble diagrams

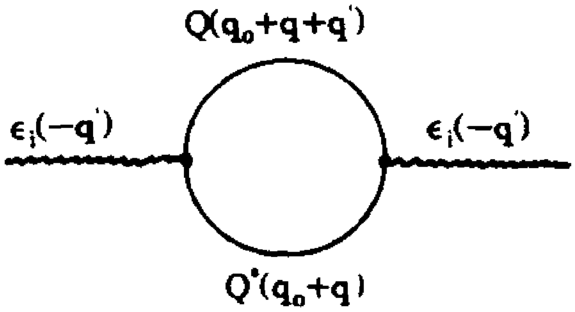

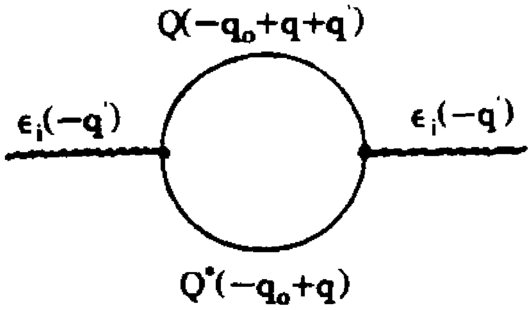

The total effect should sum the q over the Σ_2 branch.

2). When $T<T_i$:

In the incommensurate phase, ρ_o and $\epsilon_i^{q}(0)$ are different from zero. In this case, as can be seen from equation (4.1.22a), soft-branch modes with wavevectors (q_o+q) and $(-q_o+q)$ become coupled. Since they are degenerate (in the parabolic approximation with the minima at q_o and $-q_o$), they can be decoupled by introducing a canonical transformation

$$P_A(q) = \frac{1}{\sqrt{2}}[e^{-i\phi}Q(q_o+q)+e^{i\phi}Q(-q_o+q)], \tag{4.1.24a}$$

$$P_\phi(q) = \frac{i}{\sqrt{2}}[e^{-i\phi}Q(q_o+q)-e^{i\phi}Q(-q_o+q)]. \tag{4.1.24b}$$

As a result of the transformation, the eigenvalues are given by

$$\Omega_A^2(q) = 2B\rho_o^2+4D\rho_o^4+\frac{1}{2}\sum_{\alpha,\beta}\Lambda_{\alpha\beta}q_\alpha q_\beta, \tag{4.1.25a}$$

$$\Omega_\phi^2(q) = \frac{1}{2}\sum_{\alpha,\beta}\Lambda_{\alpha\beta}q_\alpha q_\beta. \tag{4.1.25b}$$

It is well know that $P_A(q)$ is the amplitudon and $P_\phi(q)$ the phason. They are associated with the local fluctuations in the amplitude and the phase of the static distortion field. A schematic illustration of these fluctuations is shown in figure 4.1.2. Note that in the incommensurate phase, the dynamic variables are

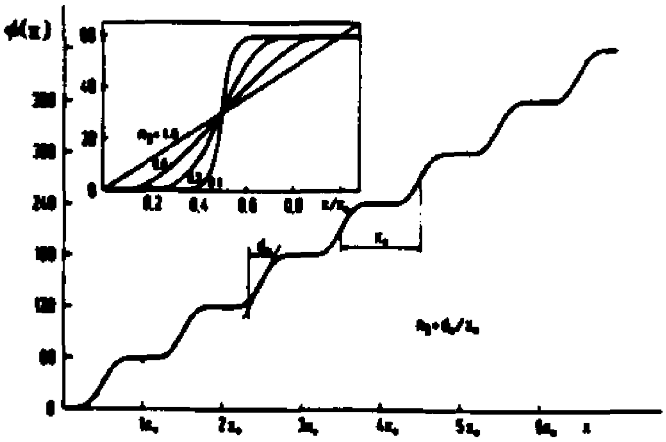

Figure 4.1.1. Spatial variation of the phase ϕ of the modulation wave for different soliton densities $n_s = d_0 / x_0$, here d_0 is the soliton width and x_0 the intersoliton spacing. The spatial variable is measured in units of $x_0 = L$. When T→T_i, n_s→1; when T→T_c, n_s→0 (from Blinc et al.[B2]).

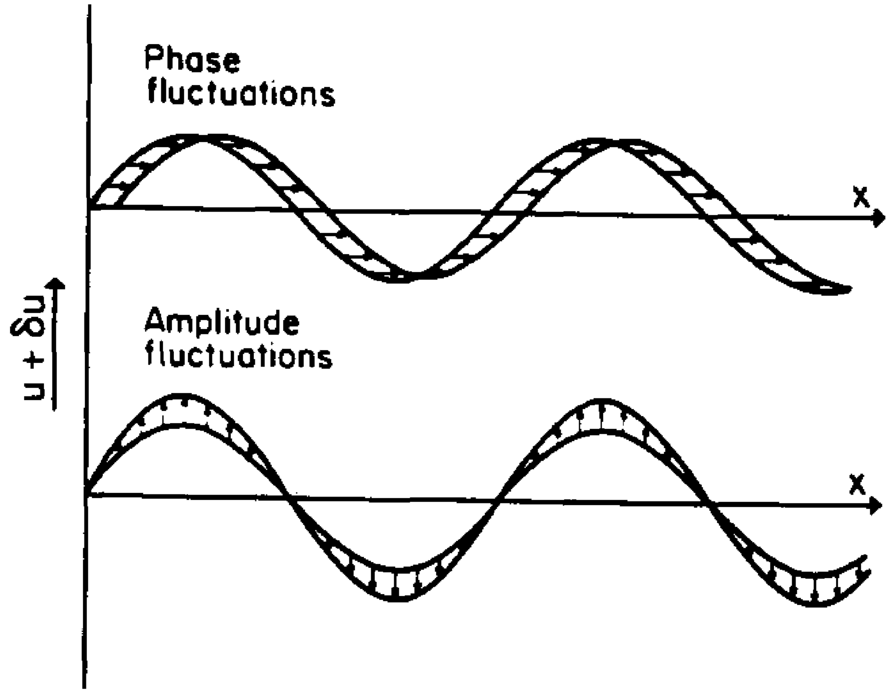

Figure 4.1.2. Schematic illustration of the amplitude and phase fluctuations of the modulation field.

no longer $Q(q)$, but $P_A(q)$ and $P_\phi(q)$. With the transformation of equations (3.1.24), equations (4.1.22a,b) have the form

$$\delta F_Q = \sum_q \Omega_A^2 P_A(q) P_A^*(q) + \sum_q \Omega_\phi^2 P_\phi(q) P_\phi^*(q), \qquad (4.1.26a)$$

$$\delta F_c = \sum_q \sum_{i=1}^{3} g_i \rho_o^2 \epsilon_i(-q') \epsilon_i(q') - \sum_q \sum_{i=1}^{3} (h_i - g_i \epsilon_i^o) \rho_o \epsilon_i(-q') P_A(q')$$

$$- \sum_{q,q'} \sum_{i=1}^{3} (h_i - g_i \epsilon_i^o) \epsilon_i(-q') [P_A(q+q') P_A^*(q) + P_\phi(q+q') P_\phi^*(q)]. \qquad (4.1.26b)$$

The second term in equation (4.1.26b) represents a bilinear coupling of the acoustic phonon to the amplitudon. From equations (4.1.24a,b), we can see that the amplitudon is essentially even and the phason is odd in the vicinity of $q = 0$. Since the elastic strains ϵ_i ($i=1$-3) are even, the invariance of the free energy restricts the bilinear coupling of acoustic phonons to the amplitudon (in the lowest order approximation - q independent coupling constants h_i and g_i). This coupling will lead to the well know Landau-Khalatnikov result of the elastic anomaly discussed by Landau and Khalatnikov in 1954[L6].

As indicated by the third term of equation (4.1.16b), in the incommensurate phase, the acoustic phonon can couple to pairs of amplitudons and phasons. Therefore we have another two bubble diagrams, one for amplitudons and one for phasons

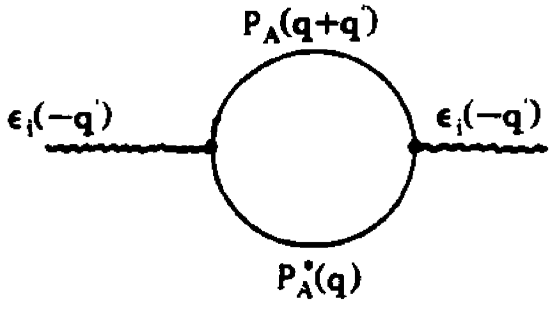

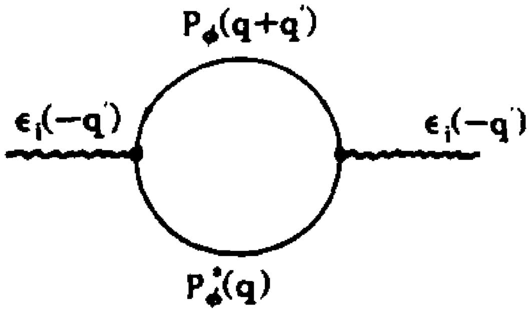

They just replace, with the same weight, the two soft mode bubble diagrams corresponding to the minima at $\pm q_0$. Again, the total contribution from the coupling can be obtained by summing over q in the vicinity of the origin.

We will show in the next section that the contributions of the third order coupling, the bubble diagrams, will lead to the well know result of the fluctuation integrals discussed by Levanyuk[L10] in 1966.

2. DERIVATION OF THE LONGITUDINAL ELASTIC ANOMALY

The longitudinal elastic constants of K_2SeO_4 exhibit anomalies in the vicinity of the incommensurate phase transition due to the coupling of strains, ϵ_i (i=1,2,3), to the order parameter through the term of $(h_i\epsilon_i - g_i\epsilon_i^2)QQ^*$ in the free energy of (4.1.2). Of the three LA modes, only the C_{33} mode shows a major anomaly near T_i, a rounded-step decreasing by about 25% in the immediate vicinity of the transition. Such anomalies are often found in incommensurate and other structural phase transitions [L7] in which bilinear coupling of strains to the order parameter is forbidden by symmetry. However, even within the simplified framework of a mean-field theory, a complete treatment of that kind of coupling effect has not been given in the case of a normal-incommensurate phase transition. Therefore, in this chapter, we will derive the expansion of the longitudinal elastic anomalies in which the fluctuation effects, including the acoustic phonon-phason coupling, have been taken into account.

To study the elastic anomaly, we need to compute the complex temperature-dependent elastic constants $\tilde{C}(\omega) = C'(\omega) + C''(\omega)$. A phenomenological approach to the calculation of the elastic constants based on the Landau free energy has been reported by Yao et al. [Y5] in their studies of the acoustic anomalies of terbium molybdate. Essentially following the same procedure, we will first find the static results from the free energy (4.1.15), then make a dynamical approach with the consideration of one dimensional order parameter,and finally, extend the result to a two dimensional order parameter system of incommensurate K_2SeO_4.

a. Static results

Minimizing the simplified free energy of equation (4.1.15) with respect to ρ and ϵ_i by setting $F_\rho = (\frac{\partial F}{\partial \rho}) = 0$ and $\sigma_i = (\frac{\partial F}{\partial \epsilon_i}) = 0$, we have the equilibrium conditions of

$$[A_0(T-T_i)+B\rho^2+D\rho^4-\sum_{i=1}^{3}(2h_i\epsilon_i-2g_i\epsilon_i^2)]\rho = 0, \qquad (4.2.1a)$$

$$\sum_{j=1}^{3}C_{ij}^{o}\epsilon_j-(h_i-2g_i\epsilon_i)\rho^2 = 0. \qquad (4.2.1b)$$

The equilibrium values of ρ and ϵ_i are give by

$$\rho_o = 0, \qquad (T>Ti) \qquad (4.2.2a)$$

$$\epsilon_i^o = 0, \qquad (T>Ti) \qquad (4.2.2b)$$

$$A_o(T-T_i)+B\rho_o^2+D\rho_o^4-\sum_{i=1}^{3}(2h_i\epsilon_i^2-2g_i\epsilon_i^{o2}) = 0, \qquad (T<T_i) \qquad (4.2.2c)$$

$$\sum_{j=1}^{3}C_{ij}^{o}\epsilon_j^o-(h_i-2g_i\epsilon_i^o)\rho_o^2 = 0. \qquad (T<T_i) \qquad (4.2.2d)$$

For small deviation of ρ and ϵ_i from equilibrium

$$\rho = \rho_o+\delta\rho_o,$$

$$\epsilon_i = \epsilon_i^o+\delta\epsilon_i,$$

the stresses σ_i and force conjugate to the order parameter F_ρ become

$$\delta F_\rho = A_o(T-T_i)\delta\rho, \qquad (T>T_i) \qquad (4.2.3a)$$

$$\delta\sigma_i = \sum_{j=1}^{3} C_{ij}^{o}\delta\epsilon_j, \qquad (T>T_i) \qquad (4.2.3b)$$

$$\delta F_\rho = (2B\rho_o^2+4D\rho_o^4)\delta\rho - \sum_{i=1}^{3}(2h_i-4g_i\epsilon_i^{o})\rho_o\delta\epsilon_i, \qquad (T<T_i) \qquad (4.2.3c)$$

$$\delta\sigma_i = \sum_{j=1}^{3} C_{ij}^{o}\delta\epsilon_j + 2g_i\rho_o^2\delta\epsilon_i - (2h_i-4g_i\epsilon_i^{o})\rho_o\delta\rho, \qquad (T<T_i) \qquad (4.2.3d)$$

where we have only kept the terms linear in $\delta\epsilon_i$ and $\delta\rho$. The static equilibrium conditions (4.2.2) are used.

In the static limit, we assume that ρ remains in equilibrium, the linearized longitudinal elastic constants under zero δF_ρ are given by $\left(\frac{\delta\sigma_i}{\delta\epsilon_i}\right)_{F_\rho=0}$. That gives

$$\tilde{C}_{ii}(\omega=0) = C_{ii}^{o}, \qquad (T>T_i) \qquad (4.2.4a)$$

$$\tilde{C}_{ii}(\omega=0) = (C_{ii}^{o}+2g_i\rho_o^2) - \frac{(2h_i-4g_i\epsilon_i^{o})^2}{2B+4D\rho_o^2}. \qquad (T<T_i) \qquad (4.2.4b)$$

This is the typical result from the coupling of $(h_i\epsilon_i-g_i\epsilon_i^2)\rho^2$. Note that in the static limit, the coupling has no effect on the elastic constants before the phase transition and causes a discontinuous changes at the phase transition point.

b. Dynamic results

In order to obtain the dynamical properties and include the fluctuation effects, a dynamic treatment for the coupled mode system must be considered. Dynamics can be introduced by constructing a Lagrangian density in which the free energy F of equation (4.1.15) is taken to be the potential energy density for the coupled modulation wave and acoustic modes. Usually, in the Landau theory, the soft mode dispersion is produced by the gradient term of $(\nabla\rho)^2$ in the free energy [L8], but for the sake of greater generality, we will not fix the soft-mode dispersion in the calculation and will use the dispersion relation obtained from neutron scattering experiments, as discussed by Yao et al.[Y5]. The kinetic energy density is taken as

$$T = \frac{1}{2}\dot{\rho}^2 + \frac{1}{2}\rho_m \sum_{i=1}^{3} \dot{u}_i^2, \tag{4.2.5}$$

where ρ_m is the mass density and $u_i(r)$ are displacements in the x_i direction, which is related to the longitudinal elastic strain by $\epsilon_i = \frac{\partial u_i}{\partial x_i}$. In the following calculation, we will limit ourselves to the longitudinal acoustic phonons traveling along the crystal axes. External driving forces are included by adding to the potential energy density with

$$F_{ext} = -\sum_{i=1}^{3} \sigma_i \epsilon_i - \rho f_\rho, \tag{4.2.6}$$

where σ_i and f_ρ are the driving stress associated with strain ϵ_i and the driving force for the soft mode. Damping can be introduced phenomenologically by a Rayleigh dissipation function of

$$F_R = \frac{1}{2}\Gamma \dot{\rho}^2 + \frac{1}{2}\rho_m \sum_{i=1}^{3} \gamma_{ii}^{o} \dot{u}_i^2, \tag{4.2.7}$$

in which Γ and γ_{ii}^{o} represent the damping of the soft mode and the acoustic modes. The equation of motion for ρ and ϵ_i are obtained from the Lagrange's equation for continuous system:

$$\frac{d}{dt}\frac{\partial L}{\partial \xi} + \sum_{i=1}^{3} \frac{\partial}{\partial x_i} \frac{\partial L}{\partial(\partial \xi / \partial x_i)} - \frac{\partial L}{\partial \xi} + \frac{\partial F_R}{\partial \xi} = 0, \tag{4.2.8}$$

where $\xi = \rho$, u_i and the Lagrangian

$$L = T - F - F_{ext}.$$

The equations of motion are given as

$$\ddot{\rho}+\Gamma\dot{\rho}+A\rho+B\rho^3+D\rho^5-\sum_{i=1}^{3}(2h_i\epsilon_i-2g_i\epsilon_i^2)\rho = f_\rho, \qquad (4.2.9a)$$

$$\rho_m\ddot{\epsilon}_i+\rho_m\gamma_{ii}^o\dot{\epsilon}_i-C_{ii}^o\frac{\partial^2\epsilon_i}{\partial x_i^2}+h_i\frac{\partial^2\rho^2}{\partial x_i^2}-2g_i\frac{\partial^2}{\partial x_i^2}(\epsilon_i\rho^2) = -\frac{\partial\sigma_i}{\partial x_i}, \qquad (4.2.9b)$$

in which a differentiation with respect to x_i has been taken for the second equation. Fourier transformation of the above equations gives

$$-\Omega^2\rho(q,\Omega)-i\Omega\Gamma\rho(q,\Omega)+A\rho(q,\Omega)+B\{\rho^*\{\rho^*\rho\}\}_{q,\Omega}+D\{\rho^*\{\rho^*\{\rho^*\rho\}\}\}_{q,\Omega}$$

$$-\sum_{i=1}^{3}2h_i\{\epsilon_i^*\rho\}_{q,\Omega}+\sum_{i=1}^{3}2g_i\{\epsilon_i^*\{\epsilon_i^*\rho\}\}_{q,\Omega}= f_\rho(q,\Omega), \qquad (4.2.10a)$$

$$-\rho_m\omega^2\epsilon_i(\mathbf{k},\omega)-i\rho_m\gamma_{ii}^o\epsilon_i(\mathbf{k},\omega)+C_{ii}^ok_i^2\epsilon_i(\mathbf{k},\omega)-h_ik_i^2\{\rho^*\rho\}_{\mathbf{k},\omega}$$

$$+2g_ik_i^2\{\epsilon_i^*\{\rho^*\rho\}\}_{\mathbf{k},\omega} = k_i^2\sigma_i(\mathbf{k},\omega), \qquad (4.2.10b)$$

where $\{f^*g\}$ denote the convolution of

$$\{f^*g\}_{q,\Omega}=\int f(q',\Omega')g(q'-q,\Omega'-\Omega)dq'd\Omega'$$

The conventional Fourier transformation is taken as

$$f(q,\Omega) = \frac{1}{(2\pi)^2}\int f(\mathbf{r},t)e^{-i(q\cdot r-\Omega)}d\mathbf{r}dt,$$

$$f(\mathbf{r},t) = \frac{1}{(2\pi)^2}\int f(q,\Omega)e^{i(q\cdot r-\Omega)}dqd\Omega$$

Now considering the small deviations of ρ and ϵ_i from their equilibrium positions, we denote

$$\rho(q,\Omega) = \rho_o\delta(q_o-q)\delta(\Omega)+\delta\rho(q,\Omega), \qquad (4.2.11a)$$

$$\epsilon_i(\mathbf{k},\omega) = \epsilon_i^o\delta(\mathbf{k})\delta(\omega)+\delta\epsilon_i(\mathbf{k},\omega), \qquad (4.2.11b)$$

where q_o is the wavevector of the soft-mode on the Σ_2 branch which is condensed below T_i. ρ_o and ϵ_i^o are the equilibrium values of ρ and ϵ_i obtained from (4.2.2). The $\delta\rho$ and $\delta\epsilon_i$ are the dynamical variables in the following calculations. Substitute the above equations into equation (4.2.10), keep terms linear in the dynamical variables of $\delta\rho$ and $\delta\epsilon_i$ as well as the coupling terms of $\delta\epsilon_i{*}\delta\rho$ from (4.2.10a) and the second order term of $\delta\rho{*}\delta\rho$ from (4.2.10b), The equations of motion for the coupled acoustic mode and the soft optical mode are

$$\frac{1}{\chi_\rho^o}\delta\rho(\mathbf{q},\Omega)-\sum_{i=1}^{3}(2h_i-4g_i\epsilon_i^{\,o})\rho_o\delta\epsilon_i(\mathbf{q}-\mathbf{q}_o,\Omega)$$

$$-\sum_{i=1}^{3}(2h_i-4g_i\epsilon_i^{\,o})\{\delta\epsilon_i{*}\delta\rho\}_{\mathbf{q},\Omega}=f_\rho(\mathbf{q},\Omega), \tag{4.2.12a}$$

$$\frac{1}{\chi_{\epsilon_i}^o}\delta\epsilon_i(\mathbf{k},\omega)-(2h_i-4g_i\epsilon_i^{\,o})\rho_o\delta\rho(\mathbf{k}-\mathbf{q}_o,\omega)$$

$$-(h_i2g_i\epsilon_i^{\,o})\{\delta\rho{*}\delta\rho\}_{\mathbf{k},\omega}=\sigma_i(\mathbf{k},\omega), \tag{4.2.12b}$$

where the χ_ρ^o and $\chi_{\epsilon_i}^o$ are the zeroth-order susceptibilities of the soft mode and the acoustic mode. They are

$$\frac{1}{\chi_\rho^o}(\mathbf{q},\Omega)=A+3B\rho_o^{\,2}+5D\rho_o^{\,4}-\sum_{i=1}^{3}(2h_i\epsilon_i^{\,o}-2g_i\epsilon_i^{\,o2})-\Omega^2-i\,\Omega\Gamma, \tag{4.2.13a}$$

$$\frac{1}{\chi_{\epsilon_i}^o}(\mathbf{k},\omega)=(C_{ii}^o+2g_i\rho_o^{\,2})-\frac{\rho_m}{k_j^{\,2}}\omega^2-i\frac{\rho_m}{k_j^{\,2}}\gamma_{ii}^o. \tag{4.2.13b}$$

From these susceptibilities, we can identify the soft-mode frequency as

$$\Omega_p^2(q_o)=A_0(T-T_i),\qquad (T>T_i) \tag{4.2.14a}$$

$$\Omega_p^2(q_o)=(2B+4D\rho_o^{\,2})\rho_o^{\,2},\qquad (T<T_i) \tag{4.2.14b}$$

where we have used the equilibrium conditions of (4.2.2). To extend the analysis with the soft-mode dispersion, we demand that the pole of $\chi_\rho^o(\mathbf{q},\Omega)$ must correspond to $\Omega_p(\mathbf{q})$ so that

$$\frac{1}{\chi_\rho^o}(\mathbf{q},\Omega)=\Omega_p(\mathbf{q})-\Omega-i\,\Omega\Gamma.$$

From (4.2.12a) one obtains

$$\delta\rho(\mathbf{q},\Omega) = \delta\rho^{o}(\mathbf{q},\Omega)$$

$$+\chi_{\rho}^{o}(\mathbf{q},\Omega)\sum_{i=1}^{3}(2h_i-4g_i\epsilon_i^{o})[\delta\epsilon_i(\mathbf{q}-\mathbf{q}_o,\Omega)+\{\delta\epsilon_i{*}\delta\rho\}_{\mathbf{q},\Omega}], \quad (4.2.15a)$$

where $\delta\rho^{o}(\mathbf{q},\Omega) = \chi_{\rho}^{o}(\mathbf{q},\Omega)f_{\rho}(\mathbf{q},\Omega)$ is the zeroth-order value of the $\delta\rho$. Substitute (4.2.15) into (4.2.12b) and only keep terms linear in $\delta\epsilon_i$ yielding

$$\sigma_i(\mathbf{k},\omega) = \frac{1}{\chi_{\epsilon_i}^{o}(\mathbf{k},\omega)}\delta\epsilon_i(\mathbf{k},\omega)-(2h_i-4g_i\epsilon_i^{o})^2\rho_o^2\chi_{\rho}^{o}(\mathbf{k}-\mathbf{q}_o,\omega)\delta\epsilon_i(\mathbf{k},\omega)$$

$$-(2h_i-4g_i\epsilon_i^{o})^2\rho_o\chi_{\rho}^{o}(\mathbf{k}-\mathbf{q}_o,\omega)\{\delta\epsilon{*}\delta\rho^{o}\}_{\mathbf{k}-\mathbf{q}_o,\omega}$$

$$-(2h_i-4g_i\epsilon_i^{o})^2\rho_o\{\delta\rho^{o*}\chi_{\rho}^{o}(\mathbf{q}',\Omega')\delta\epsilon_i(\mathbf{q}'-\mathbf{q}_o,\Omega')\}_{\mathbf{k},\omega}$$

$$-(2h_i-4g_i\epsilon_i^{o})^2\{\delta\rho^{o*}\chi_{\rho}^{o}(\mathbf{q}',\Omega')\{\delta\epsilon{*}\delta\rho^{o}\}_{\mathbf{q},\Omega}\}_{\mathbf{k},\omega}. \quad (4.2.16)$$

To evaluate the nonlinear coupling terms in the above equation, we note that the average of the thermal fluctuation of $<\delta\rho^{o}> = 0$, and introduce the fluctuation- dissipation theorem [H6] which provides

$$<\delta\rho^{o}(\mathbf{q},\Omega)\delta\rho^{o}(\mathbf{q}',\Omega)> = \frac{2k_BT}{(2\pi)^4\Omega}\mathrm{Im}[\chi_{\rho}^{o}(\mathbf{q},\Omega)]\delta(\mathbf{q}+\mathbf{q}')\delta(\Omega+\Omega), \quad (4.2.17)$$

where $\mathrm{Im}[\chi_{\rho}^{o}(\mathbf{q},\Omega)]$ is the imaginary part of χ_{ρ}^{o}. Then the average of the σ_i over the thermal fluctuation of $\delta\rho^{o}$ gives

$$<\sigma_i(\mathbf{k},\omega)>_{\delta\rho} = \frac{1}{\chi_{\epsilon_i}^{o}(\mathbf{k},\omega)}\delta\epsilon_i(\mathbf{k},\omega)-(2h_i-4g_i\epsilon_i^{o})^2\rho_o^2\chi_{\rho}^{o}(\mathbf{k}-\mathbf{q}_o,\omega)\delta\epsilon_i(\mathbf{k},\omega)$$

$$-\frac{2k_BT}{(2\pi)^4}(2h_i-4g_i\epsilon_i^{o})^2\delta\epsilon_i(\mathbf{k},\omega)\int d\mathbf{q}\int\frac{d\Omega}{\Omega}\mathrm{Im}[\chi_{\rho}^{o}(\mathbf{q},\Omega)]\chi_{\rho}^{o}(\mathbf{k}-\mathbf{q},\omega-\Omega). \quad (4.2.18)$$

The elastic susceptibility is given by $\frac{1}{\chi_{\epsilon_i}} = \frac{\partial <\sigma_i>_{\delta\rho}}{\partial(\delta\epsilon_i)}$. With the approximation of $\chi_\rho^o(\mathbf{k}-\mathbf{q}_o,\omega) \approx \chi_\rho^o(\mathbf{q}_o,\omega)$, we substitute (4.2.13a) into the second and third terms of (4.2.18), then carry out the integration over the Ω by using contour integration, which gives us

$$\frac{1}{\chi_{\epsilon_i}(\mathbf{k},\omega)} = \frac{1}{\chi_{\epsilon_i}^o(\mathbf{k},\omega)} - \frac{(2h_i-4g_i\epsilon_i^o)^2\rho_o^2}{\Omega_p^2(q_o)-\omega^2-i\omega\Gamma}$$

$$-\frac{2k_BT(2h_i-4g_i\epsilon_i^o)^2}{(2\pi)^3}\int dq \frac{(1+i\omega/\ 2\Gamma)}{\Omega_p^2(1-i\omega/\ \Gamma)[4\Omega_p^2-i2\omega\Gamma(1-i\omega/\ \Gamma)]}. \qquad (4.2.19)$$

For $\omega \ll \Gamma$ which is true in the case of K_2SeO_4, we drop terms of ω/Γ. Since $\omega \ll \Omega_p(q_o)$ we omit the ω^2 in the second term. That results in

$$\frac{1}{\chi_{\epsilon_i}(\mathbf{k},\omega)} = \frac{1}{\chi_{\epsilon_i}^o(\mathbf{k},\omega)} - \frac{(2h_i-4g_i\epsilon_i^o)^2\rho_o^2}{\Omega_p^2(q_o)-i\omega\Gamma}$$

$$-\frac{2k_BT(2h_i-4g_i\epsilon_i^o)^2}{(2\pi)^3}\int \frac{dq}{\Omega_p^2(q)[4\Omega_p^2(q)+i2\omega\Gamma(q)]}. \qquad (4.2.20)$$

By using the above susceptibility and equation (4.2.13b), we can find the elastic constant and the damping as

$$C_{ii}'(\omega) = (C_{ii}^o+2g_i\rho_o^2) - \frac{(2h_i-4g_i\epsilon_i^o)^2\rho_o^2\,\Omega_p^2(q_o)}{\Omega_p^4(q_o)+\omega^2\Gamma^2}$$

$$-\frac{2k_BT(2h_i-4g_i\epsilon_i^o)^2}{(2\pi)^3}\int \frac{dq}{4\Omega_p^4(q)+\omega^2\Gamma^2(q)}, \qquad (4.2.21a)$$

$$\gamma_{ii}(\omega) = \gamma_{ii}^o + \frac{k_i^2}{\rho_m}\frac{(2h_i-4g_i\epsilon_i^o)^2\rho_o^2\Gamma}{\Omega_p^4(q_o)+\omega^2\Gamma^2}$$

$$+\frac{k_i^2}{\rho_m}\frac{k_BT(2h_i-4g_i\epsilon_i^o)^2}{(2\pi)^3}\int \frac{\Gamma dq}{\Omega_p^2(q)[4\Omega_p^4(q)+\omega^2\Gamma^2(q)]}. \qquad (4.2.21b)$$

The second term in equation (4.2.20) is the well known Landau-Khalatnikov term resulted from the bilinear coupling of $\delta\epsilon_i\delta\rho$. In the $\omega\rightarrow 0$ limit, it reduces to the static result of equation (4.2.4). The third term of equation (4.2.20) is the fluctuation integral developed from the third order coupling of $\delta\epsilon_i\delta\rho\delta\rho$. This integral is important in both the normal and incommensurate phase near T_i where the $\Omega_p\rightarrow 0$.

In order to obtain the elastic anomalies for the two dimensional dynamic variable system of K_2SeO_4, we have to extend the above results from the simplified free energy employed so far by considering the free energy in normal mode expansions and the dynamic results discussed in section 4.1b. When $T>T_i$, the elastic anomalies are caused only by the third order coupling. It is clear that from equation (4.1.23), two fluctuation integrals will be obtained corresponding to the two minima on the Σ_2 branch. In the case of $T<T_i$, the elastic anomalies are caused by two effects: bilinear coupling and third order couplings. It is also clear that from equation (4.1.26), a Landau-Khalatnikov term will result from the bilinear coupling of the acoustic phonon and the amplitudon, and two fluctuation integrals will be resulted from the third order coupling of the acoustic phonon to pairs of amplitudons and phasons. Therefore, the theoretical predictions for the temperature dependence of the elastic constants and the attenuation are given as

$T>T_i$:

$$C'_{ii}(\omega) = C^o_{ii}-\frac{16k_BT}{(2\pi)^3}h_i^2\int\frac{dq}{4\Omega^4_{\Sigma_2}(q)+\omega^2\Gamma^2_{\Sigma_2}(q)}, \tag{4.2.22a}$$

$$\gamma_{ii}(\omega) = \gamma^o_{ii}+\frac{k_i^2}{\rho_m}\frac{8k_BT}{(2\pi)^3}h_i^2\int\frac{\Gamma_{\Sigma_2}(q)dq}{\Omega^2_{\Sigma_2}(q)[4\Omega^4_{\Sigma_2}(q)+\omega^2\Gamma^2_{\Sigma_2}(q)]}, \tag{4.2.22b}$$

$T<T_i$:

$$C_{ii}'(\omega) = (C_{ii}^o+2g_i\rho_o^2)-\frac{(2h_i-4g_i\epsilon_i^o)^2\rho_o^2\,\Omega_A^2(0)}{\Omega_A^4(0)+\omega^2\Gamma_A^2(0)}$$

$$-\frac{2k_BT}{(2\pi)^3}(2h_i-4g_i\epsilon_i^o)^2\left[\int\frac{dq}{4\Omega_A^4(q)+\omega^2\Gamma_A^2(q)}\right.$$

$$\left.+\int\frac{dq}{4\Omega_\phi^4(q)+\omega^2\Gamma_\phi^2(q)}\right], \qquad (4.2.22c)$$

$$\gamma_{ii}(\omega) = \gamma_{ii}^o+\frac{k_i^2}{\rho_m}\frac{(2h_i-4g_i\epsilon_i^o)^2\rho_o^2\Gamma_A(0)}{\Omega_A^4(0)+\omega^2\Gamma_A^2(0)}$$

$$+\frac{k_i^2}{\rho_m}\frac{k_BT}{(2\pi)^3}(2h_i-4g_i\epsilon_i^o)^2\left[\int\frac{\Gamma_A(q)dq}{\Omega_A^2(q)[4\Omega_A^4(q)+\omega^2\Gamma_A^2(q)]}\right.$$

$$\left.+\int\frac{\Gamma_\phi(q)dq}{\Omega_\phi^2(q)[4\Omega_\phi^4(q)+\omega^2\Gamma_\phi^2(q)]}\right]. \qquad (4.2.22d)$$

In the expressions of equation (4.2.22a) and (4.2.22b), we have multiplied the fluctuation integrals by 2 to take into account the existence of the two minima in the Σ_2 branch. Also, in the Landau-Khalatnikov terms of equation (4.2.22c) and (4.2.22d), we have used the approximations of $\Omega_A(q_i) \approx \Omega_A(0)$ and $\Gamma_A(q_i) \approx \Gamma_A(0)$ which is valid for phonons of small q_i detected by ultrasonics or Brillouin scattering. In the above expressions, Ω_{Σ_2}, Γ_{Σ_2}, Ω_A, Γ_A, Ω_ϕ, and Γ_ϕ are the frequencies and attenuations of the Σ_2 soft mode, the amplitude mode, and the phase mode branches respectively. Expressions of Ω_{Σ_2}, Ω_A, and Ω_ϕ are given by equations (4.1.18), (4.1.25a) and (4.1.25b).

After evaluating the coefficients of the free energy (4.1.15), we will use equations (4.2.22) to calculate the temperature dependance of the elastic and damping constants. By comparing the theoretical results with the experimental results, we may check the validity of the theory and the consistence of the analysis.

3. EVALUATION OF THE FREE ENERGY COEFFICIENTS

Most of the coefficients in the full form free energy expansion of equation (4.1.2) can be evaluated from the existing experimental literature on K_2SeO_4 as has been discussed by Sannikov and Golovko [55]. However, for the purpose of analyzing the C_{33} longitudinal acoustic anomalies around the normal-incommensurate phase transition, we will only consider the coefficients A_o, B, D, $C_{ij}(i,j=1-3)$, $h_i(i=1-3)$ and g_3 appearing in the simplified free energy of equation (4.1.15) (ignoring all g_i except g_3) as well as the three diagonal components of the tenser $\Lambda_{\alpha\beta}$ in equation (4.1.18). These coefficients are necessary for carrying out the theoretical calculations with equations (4.2.22).

a. A_o:

Equation (4.1.18) shows that in the normal phase, the coefficient A_o is related to the soft mode frequency by

$$\Omega^2_{\Sigma_2}(q_o) = A_o(T-T_i). \tag{4.3.1}$$

The temperature dependence of the $\Omega_{\Sigma_2}(q_o)$ has been determined by Iizumi et al.[11] in their inelastic neutron scattering studies of K_2SeO_4. Their results are shown in figure 4.3.1. A linear fit to the data points of $q_o = (0.31,0,0)$ gives

$$[h\Omega_{\Sigma_2}(q_o)]^2 = 0.07(T-T_i)\ \mathrm{meV^2K^{-1}}, \tag{4.3.2}$$

from which we obtain

$$A_o = 1.6\times10^{23}S^{-2}K^{-1} \tag{4.3.3}$$

b. C_{ij}^{o} :

We have estimated the "bare" values of the elastic constants $C_{ii}^{o}(i=1\text{-}3)$ by extrapolating the Brillouin Scattering results of Hauret et al.[H2] to T_i in the normal phase, and the $C_{ij}^{o}(i\neq j,\ i,j=1\text{-}3)$ by the Brillouin scattering results of Rehwald et al.[R1] (as shown in figure 2.1.7). We find

$$[C^{o}] = \left|\begin{array}{ccc} 5.8 & 1.7 & 1.5 \\ & 5.4 & 2.0 \\ & & 4.0 \end{array}\right| \times 10^{11}\text{dyn cm}^{-2}, \qquad (4.3.4a)$$

and

$$[S^{o}] = [C^{o}]^{-1} = \left|\begin{array}{ccc} 0.20 & -0.045 & -0.045 \\ & 0.23 & -0.10 \\ & & 0.32 \end{array}\right| \times 10^{-11}\text{dyn}^{-1}\text{cm}^{2}. \; (4.3.4b)$$

c. B and h_i :

The B and h_i coefficients are related to the abrupt changes of the specific heat (ΔC_p) and thermal expansion coefficients ($\Delta\alpha_i$) at T_i.

The specific heat anomalies of K_2SeO_4 have been measured by several groups [A3][L2][C2][F2][A7]. From the most resent result of Flerov et al.[F2], the specific heat jump at T_i is $\Delta C_p = 10.1\text{J K}^{-1}\text{mol}^{-1}$. With the molar volume of $72\text{cm}^3\text{mol}^{-1}$ ($g=3.05\text{g cm}^{-1}$, 1 mole=221g), we find

$$\Delta C_p = 1.4\times10^{6}\text{erg cm}^{-3}\text{K}^{-1}. \qquad (4.3.5)$$

The thermal expansion of K_2SeO_4 has also been studies by several groups [M2][F2][K3][S1]. From the results of Flerov et al.[F2], the discontinuities of the thermal expansion coefficients at T_i, as shown in figure 2.1.5, were found to be

$$[\ \Delta\alpha_1, \Delta\alpha_2, \Delta\alpha_3\ ] = [\ 3.4, 8.1, -19.1\ ] \times 10^{-5}\text{K}^{-1}. \qquad (4.3.6)$$

When temperature is very close to T_i, the simplified free energy of equation (4.1.15) can be further reduced by ignoring the sixth power and the biquadratic coupling terms. We write

$$F(T \approx T_i,\ \sigma=0) = F_o + \frac{1}{2}A\rho^2 + \frac{1}{4}B\rho^4 + \frac{1}{2}\sum_{i,j=1}^{3} C_{ij}^{o}\epsilon_i\epsilon_j - \sum_{i=1}^{3} h_i\epsilon_i\rho^2, \qquad (4.3.7)$$

where F_o is the "background" free energy which does not depend on ϵ_i and ρ. By minimizing the above free energy with respect to ϵ_i, we have the spontaneous strains at zero stress

$$\epsilon_i^{o} = \sum_{j=1}^{3} S_{ij}^{o} h_j \rho_o^2. \qquad (4.3.8)$$

Using this result to eliminate the ϵ_i, the free energy of equation (4.3.7) can be rewritten into

$$F(T \approx T_i,\ \sigma=0) = F_o + \frac{1}{2}A\rho^2 + \frac{1}{4}B'\rho^4 \qquad (4.3.9)$$

where

$$B' = B - 2\sum_{i,j=1}^{3} h_i S_{ij}^{o} h_j. \qquad (4.3.10)$$

From the equilibrium condition of $\frac{\partial F}{\partial \rho} = 0$, the equilibrium value of the order parameter near T_i is given as

$$\rho_o^2 = 0, \qquad (T>T_i) \qquad (4.3.11a)$$

$$\rho_o^2 = -\frac{A}{B'}, \qquad (T<T_i) \qquad (4.3.11b)$$

so that

$$F = F_o, \qquad (T>T_i) \qquad (4.3.12a)$$

$$F(\epsilon_i=\epsilon_i^{o},\ \rho=\rho_o) = F_o - \frac{A^2}{4B'}. \qquad (T<T_i) \qquad (4.3.12b)$$

the specific heat, $C_p = -T(\frac{\partial^2 F}{\partial T^2})_{(\epsilon_i^\circ,\, \rho_o)}$, is then

$$C_p = C_p^\circ, \qquad (T>T_i) \qquad (4.3.13a)$$

$$C_p = C_p^\circ + \frac{TA_o^2}{2B'} \qquad (T<T_i) \qquad (4.3.13b)$$

where $C_p^\circ = -T(\frac{\partial^2 F_o}{\partial T^2})_{(\epsilon_i^\circ,\, \rho_o)}$ is the "background" specific heat due to other degrees of freedom. The jump of the specific heat at T_i is, thus,

$$\Delta C_p = \frac{T_i A_o^2}{2B'}. \qquad (4.3.14)$$

Similarly, the thermal expansion coefficients $\alpha_i = (\frac{\partial \epsilon_i^\circ}{\partial T})$ can be obtained from equation (4.3.7) with $\alpha_i = \sum_{j=i}^{3} S_{ij}^\circ h_j (\frac{\partial \rho_o^2}{\partial T})$. We have

$$\alpha_i = \alpha_i^\circ, \qquad (T>T_i) \qquad (4.3.15a)$$

$$\alpha_i = \alpha_i^\circ - \sum_{j=1}^{3} S_{ij}^\circ h_j \frac{A_o}{B'}. \qquad (T<T_i) \qquad (4.3.15b)$$

The jump in α_i at T_i is then

$$\Delta\alpha_i = -\frac{A_o}{B'} \sum_{j=1}^{3} S_{ij}^\circ h_j, \qquad (4.3.16)$$

From equations (4.3.14) and (4.3.16), we obtain

$$h_i = -\frac{A_o T_i}{2\Delta C_p} \sum_{j=1}^{3} C_{ij}^\circ \Delta\alpha_j, \qquad (4.3.17)$$

while from equations (4.3.10) and (4.3.14), we have

$$B = \frac{T_i A_o^2}{2\Delta C_p} + 2 \sum_{i,j=1}^{3} h_i S_{ij} h_j, \qquad (4.3.18)$$

Using the values of A_o, C_{ij}^o, ΔC_p and $\Delta\alpha_i$ obtained above, we find

$$B = 2.1 \times 10^{43} g^{-1} cm\ s^2, \tag{4.3.19}$$

and

$$[\ h_1, h_2, h_3\ ] = [\ -0.42, -0.80, 3.8\ ] \times 10^{26} s^{-2}. \tag{4.3.20}$$

An auxiliary check of these values can be made from the downward step in C_{33} at T_i which experimentally is approximately 11×10^{10}dyn cm^{-2} as shown in figure 3.3.2. From the static result of equations (4.2.4), the calculated abrupt change in C_{33} at T_i is

$$\Delta C_{33}(\omega{=}0) = -\frac{2h_3^2}{B} = -14 \times 10^{10} \text{dyn cm}^{-2}, \tag{4.3.21}$$

in reasonable agreement with observation.

d. D and g_3 :

The coefficients of the sixth order term and the biquadratic coupling term (D and g_3) in the simplified free energy of equation (4.1.15) cannot be properly evaluated from existing experimental data, but they can be estimated from the temperature dependence of the spontaneous strain ϵ_3^o in the incommensurate phase, as determined from X-ray diffraction data by Kudo and Ikeda [K3]. The equilibrium conditions obtained from equation (4.1.15) for $T < T_i$ are:

$$A_o(T-T_i)+B\rho_o^2+D\rho_o^4-2\sum_{i=1}^{3} h_i\epsilon_i^o+2g_3(\epsilon_3^o)^2 = 0, \tag{4.3.22a}$$

$$\sum_{j=1}^{3} C_{ij}^o\epsilon_j^o-h_i\rho_o^2+2\delta_{3i}g_i\epsilon_i^o\rho_o^2 = 0 \qquad (i = 1,2,3), \tag{4.3.22b}$$

where the δ_{3i} eliminates the g_i except g_3 terms. From these equations, $\rho_o(T)$ and $\epsilon_i^o(T)$ can, in principle, be deduced if D and g_3 are known. Treating D or g_3 as a fitting parameter and fitting the ϵ_3^o to the experimental data [K3], one

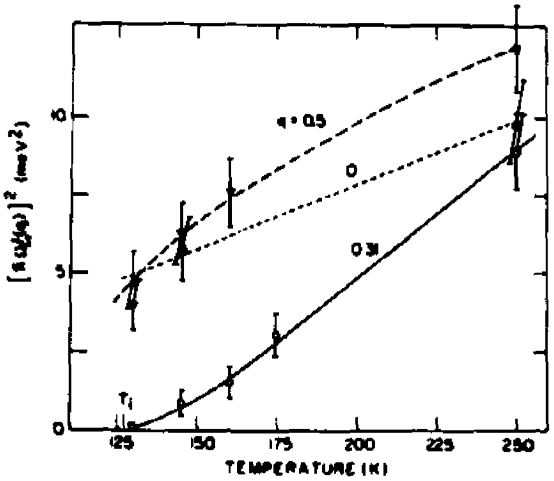

Figure 4.3.1. Squares of the phonon energies of K_2SeO_4 at the zone center, q = (0, 0, 0) at q_o = (0.31, 0, 0) and at the zone boundary, q = (0.5, 0, 0) as a function of temperature (from Iizumi et al.[I1]).

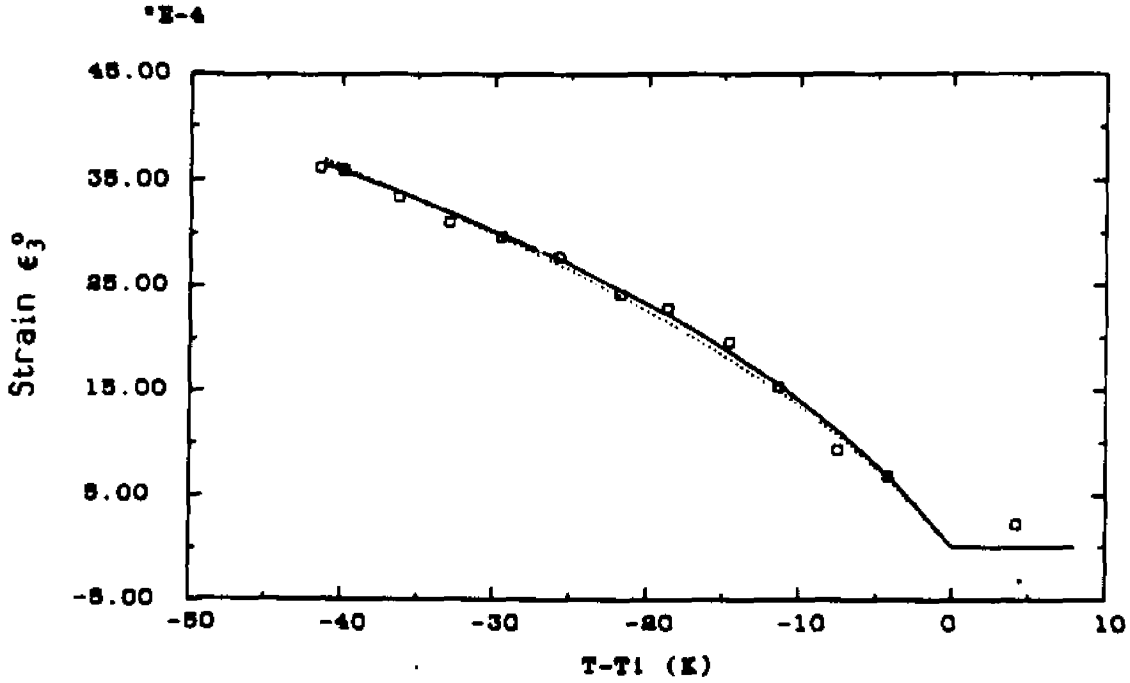

Figure 4.3.2. Best fit to the spontaneous strain ϵ_3^o by using equations (4.3.22a) and (4.3.22b). Squares are the experimental results from Kudo and Ikeda [K3], solid line is the best fitting result with D=0, $g_3 = 1.8\times10^{28}s^{-2}$ and the dotted line is the best fitting result with $g_3 = 0$, $D = 0.42\times10^{60}g^{-2}cm^2s^{-2}$.

can deduce the best value of either D or g_3, setting the other one equal to zero. By setting D=0, we obtained a best fit of ϵ_3^o, as shown in figure 4.3.2 (solid line), with

$$g_3 = 1.8 \times 10^{-28} s^{-2}. \qquad \textbf{(4.3.23a)}$$

Conversely, by setting $g_3 = 0$ we obtain another best fit, also shown in figure 4.3.2 (dotted line), with

$$D = 0.42 \times 10^{60} g^{-2} cm^2 s^{-2}. \qquad \textbf{(4.3.23b)}$$

e. Λ_i :

As has been indicated in equation (4.1.18), the dispersion of the Σ_2 optic branch near $\mathbf{K} = \mathbf{q}_o + \mathbf{q} = 0$ can be represented by

$$\Omega_{\Sigma_2}^2(\mathbf{q}) = \Omega_{\Sigma_2}^2(\mathbf{q}_o) + \frac{1}{2}\Lambda_x K_x^2 + \frac{1}{2}\Lambda_y K_y^2 + \frac{1}{2}\Lambda_z K_z^2. \qquad \textbf{(4.3.24)}$$

From the neutron scattering results of Iizumi et al.[11] at T=130K, we find

$$\Lambda_x = 3.2\ THz^2 \dot{A}^2, \qquad \textbf{(4.3.25a)}$$

$$\Lambda_z = 17\ THz^2 \dot{A}^2. \qquad \textbf{(4.3.25b)}$$

Λ_y was not determined, so we assume that

$$\Lambda_y = \Lambda_z. \qquad \textbf{(4.3.25c)}$$

We also assume that the Λ_i are temperature independent and have the same values above and below T_i.

f. Γ :

In agreement with Quilichini and Currat [Q1], for the whole temperature range under study, we assume a $\mathbf{q}$-independent damping constant for the soft

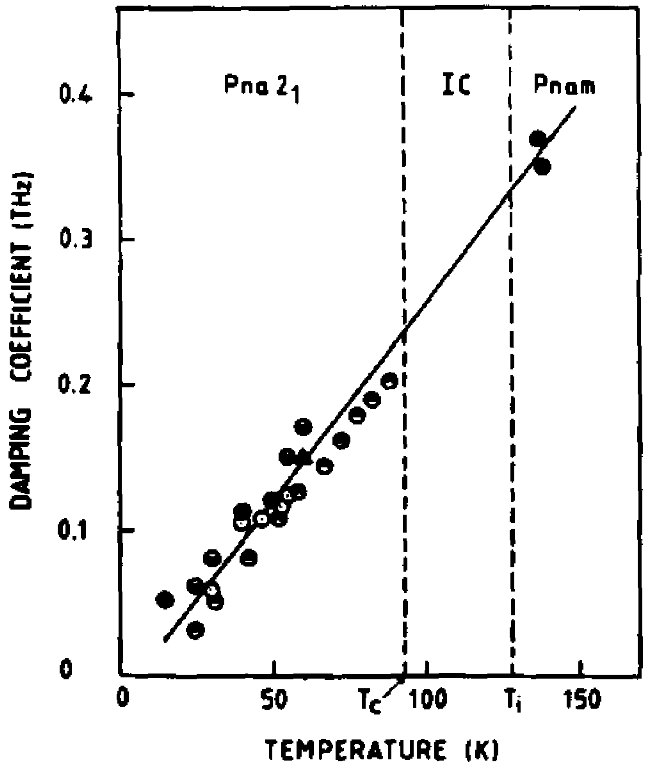

Figure 4.3.3. Pseudo-phason ($T < T_c$) and soft-mode ($T > T_i$) damping constants: open and half filled circles – data from Raman scattering; filled circles and triangles – data from neutron scattering (from Quilichini et al.[91]

modes (Σ_2, amplitudon and phason) and represent its temperature variation by:

$$\Gamma = [0.0027(T-T_i)+0.34]\ \mathrm{THz}, \qquad (4.3.26)$$

as shown in figure 4.3.3 obtained from Quilichini et al.[Q1].

Having evaluated all the coefficients in the free energy of equation (4.1.15) and rewriting equations (4.1.25a) and (4.1.25b) as

$$\Omega_A^2(K) = 2B\rho_o^2+4D\rho_o^4+\frac{1}{2}\Lambda_x K_x^2+\frac{1}{2}\Lambda_z(K_y^2+K_z^2), \qquad (4.3.27a)$$

$$\Omega_\phi^2(K) = \frac{1}{2}\Lambda_x K_x^2+\frac{1}{2}\Lambda_z(K_y^2+K_z^2), \qquad (4.3.27b)$$

we are able to calculate the temperature dependence of the $C_{33}'(\omega)$ and $\gamma_{33}(\omega)$ with the equations (4.2.22). The calculations will be shown in the next section.

Quilichini and Currat [Q1] have verified, in their inelastic neutron scattering experiments on the phason dispersion, that the Γ, Λ_x and Λ_z deduced from equation (4.3.27b) are consistent with the values obtained above T_i as we have assumed. However, their data (as shown in figure 2.1.2) indicate that the phason frequency at $K = 0$ is not zero; instead it indicates a value of

$$\Omega_\phi(0) \approx 60 \pm 25\ \mathrm{GHz}, \qquad (4.3.28)$$

which does not agree with equation (4.3.27b). We therefore add a phason gap term to the equation and rewrite it as

$$\Omega_\phi^2(K) = \Omega_\phi^2(0)+\frac{1}{2}\Lambda_x K_x^2+\frac{1}{2}\Lambda_z(K_y^2+K_z^2). \qquad (4.3.29)$$

We summarize all the coefficients evaluated in this section in the second column of table I. For comparison, we also list the values of the coefficients found by Sannikov and Golovko [S5] in the last column of the table.

TABLE I. FREE ENERGY COEFFICIENTS.

Coefficient	Value found from previous experiments *	Best fit of $C_{33}(\omega)$ and $\gamma_{33}(\omega)$ to present experiments (mean Field) **	Value found by Sannikov and Golovko ***
A_0 $(s^{-2}K^{-1})$	1.6×10^{23}		1.5×10^{23}
B $(g^{-1}s^{-2}cm)$	2.1×10^{42}	2.1×10^{42}(with $D=0$) 2.0×10^{42}(with $g_3=0$)	2.1×10^{42}
D $(g^{-2}cm^2s^{-2})$	4.2×10^{59}(with $g_3=0$)	3.6×10^{59}(with $g_3=0$)	
$[C^0]$(dyn cm^{-2})	$\begin{vmatrix} 5.8 & 1.7 & 1.5 \\ & 5.4 & 2.0 \\ & & 4.0 \end{vmatrix}\times10^{11}$		$\begin{vmatrix} 5.8 & 1.7 & 1.5 \\ & 5.3 & 2.0 \\ & & 3.8 \end{vmatrix}\times10^{11}$
h_1 (s^{-2})	-0.42×10^{26}		-0.31×10^{26}
h_2 (s^{-2})	-0.80×10^{26}		-0.90×10^{26}
h_3 (s^{-2})	3.8×10^{26}	3.5×10^{26}	3.6×10^{26}
g_3 (s^{-2})	1.8×10^{28}(with $D=0$)	1.2×10^{28}(with $D=0$)	
Λ_x $(THz^2\dot{A}^2)$	3.2		
$\Lambda_y=\Lambda_z(THz^2\dot{A}^2)$	17		
Γ (THz)	$0.0027(T-T_i)+0.34$		
$\Omega_\phi(0)$ (GHz)	60 ± 25		

* As described in the text of Sec. 4.3.

** Values for the unfilled coefficients in this column are the same as those in the first column.

*** D.G. Sannikov and V.A. Golovoko, Sov. Phys. Solid State 20 580 (1978). Values for the coefficients not given in this column were not determined in their analysis.

4. COMPARISON OF THEORY WITH EXPERIMENTAL RESULTS

a. Estimation of "adiabatic correction"

It is known that the measured elastic constant will be adiabatic if the period of the elastic wave is short compared to the time required for relaxation by heat conduction [H7]. The necessary inequality for an adiabatic process[Z1][B6] is $\gamma \ll \gamma_c$ where γ_c is the "crossover" frequency given by

$$\gamma_c = v^2 \frac{\rho_m C_p}{2K_t}, \tag{4.4.1}$$

and v, ρ_m, C_p and K_t are the sound velocity, density, specific heat and thermal conductivity of the sample, respectively. For K_2SeO_4 around T_i, these quantities are estimated as $v \approx 1.8\times10^5$ cm s^{-1}, $C_p \approx 1.4\times10^7$erg k^{-1}cm^{-3}, $\rho_m = 3.05$ g cm^{-3} and $K_t \approx 10^6$ erg cm^{-1}s^{-1}K^{-1}. With these values, we have $\gamma_c \approx 7\times10^2$GHz, whereas the Brillouin frequency of the C_{33} longitudinal mode around T_i is $\gamma_B \approx 16$GHz, showing that $\gamma_c \gg \gamma_B$. Therefore the C_{33} elastic constants obtained from our Brillouin scattering measurements are adiabatic.

To derive the static adiabatic elastic constants for C_{ii} (i=1−3) longitudinal modes, we use the simplified free energy (equations (4.3.35)) and include a "background" term $F_0(T)$ as we did in equation (4.3.7). The forces conjugate to the order parameter $F_\rho = (\frac{\partial F}{\partial \rho})$, the stresses $\sigma_i = (\frac{\partial F}{\partial \epsilon_i})$ and the entropy $S = -(\frac{\partial F}{\partial T})$ are then

$$F_\rho = A\rho + B\rho^3 + D\rho^5 - 2\sum_{i=1}^{3} h_i \epsilon_i \rho + 2\sum_{i=1}^{3} g_i \epsilon_i^2 \rho, \tag{4.4.2a}$$

$$\sigma_i = \sum_{j=1}^{3} C_{ij}^0 \epsilon_j - h_i \rho^2 + 2 g_i \epsilon_i \rho^2, \tag{4.4.2b}$$

$$S = -\frac{A_o}{2}\rho^2 - \frac{\partial F_o}{\partial T}. \tag{4.4.2c}$$

The equilibrium values of ρ and ϵ_i are given in equations (4.2.2). For small departures from equilibrium, we find

$$\delta F_\rho = (2B+4D\rho_o^2)\rho_o^2\delta\rho - \sum_{i=1}^{3}(2h_i-4g_i\epsilon_i^o)\rho_o\delta\epsilon_i + A_o\rho_o\delta T, \tag{4.4.3a}$$

$$\delta\sigma_i = \sum_{j=1}^{3}C_{ij}^o\delta\epsilon_j + 2g_i\rho_o^2\delta\epsilon_i - (2h_i-4g_i\epsilon^o)\rho_o\delta\rho, \tag{4.4.3b}$$

$$\delta S = -A_o\rho_o\delta\rho - \frac{\partial^2 F_o}{\partial T^2}\delta T, \tag{4.4.3c}$$

where we have used the equilibrium conditions (equations (4.2.2)) and kept the terms linear in the fluctuations. With the adiabatic condition $\delta S = 0$ and the assumption of $\delta F_\rho = 0$ which has been discussed previously, we have

$$\frac{\partial^2 F_o}{\partial T^2}\delta T = -A_o\rho_o\delta\rho, \tag{4.4.4a}$$

$$(2B+4D\rho_o^2+\frac{A_o^2T}{C_p^o})\rho_o^2\delta\rho = \sum_{i=1}^{3}(2h_i-4g_i\epsilon_i^o)\rho_o\delta\epsilon_i. \tag{4.4.4b}$$

To derive equation (4.4.4b), we have used equation (4.4.4a) and the relation $C_p^o = -T(\frac{\partial^2 F_o}{\partial T^2})$. The longitudinal adiabatic elastic constants $\tilde{C}_{ii}^s(\omega)$ under zero δF_ρ are given by $(\frac{\delta\sigma_i}{\delta\epsilon_i})_{\delta F_\rho,\delta S=0}$. From equation (4.4.3b) and the above conditions, we obtain

$$\tilde{C}_{ii}^s(0) = C_{ii}^o \qquad (T>T_i), \tag{4.4.5a}$$

$$\tilde{C}_{ii}^s(0) = (C_{ii}^o+2g_i\rho^2) - \frac{(2h_i-4g_i\epsilon_i^o)^2}{2B+4D\rho_o^2+A_o^2T/\,C_p^o} \qquad (T<T_i). \tag{4.4.5b}$$

Comparison of the these results with equations (4.2.4) shows that the term

A_o^2T/C_p^o appearing in equation (4.4.5b) is the "adiabatic correction". This correction can be estimated by using the values of the free energy coefficients evaluated in the last section. With $B = 2.1\times10^{42}\ g^{-1}s^{-2}cm$, $T=130K$, $A_o = 1.6\times10^{23}\ s^{-2}K^{-1}$ and $C_p^o = 1.4\times10^7$ erg $K^{-1}cm^{-3}$, we find the ratio

$$\frac{A_o^2T/\ C_p^o}{2B} \approx 5\%. \tag{4.4.6}$$

The correction only changes the value of the denominator in the second term of equation (4.4.5b) by about 5%.

Because the "adiabatic correction" effect is small, we will ignore it the following calculations in order to simplify the analysis.

b. Theoretical predictions and comparison with experimental results

Now we can compare the mean-field theory predictions of $C_{33}^{'}(\omega)$ and $\gamma_{33}(\omega)$ given in equations (4.2.22) with the Brillouin scattering data of the C_{33} longitudinal mode described in the section 3 of chapter 3. We begin by evaluating the equations (4.2.22) using the evaluated free energy coefficients described in the last section. For the acoustic frequency ω in these equations we used the approximate value

$$\omega = 2\left|\frac{C_{33}^o}{\rho_m}\right|^{1/2} n_b\frac{\omega_L}{c}\sin(\frac{\theta}{2}), \tag{4.4.7}$$

where ω_L is the laser frequency, $\frac{c}{n_b}$ is the speed of light in the crystal, and θ is the scattering angle. This value of ω corresponds to the "bare" frequency of the acoustic phonon without including coupling. From our experimental results as shown in figure 3.3.2(a), we have $\omega = 2\pi\times16.2\ s^{-1}$.

We evaluated the equations both with $D = 0$, $g_{33} \neq 0$ and vice-versa. For these two cases, the results were somewhat different in $C_{33}^{'}(\omega)$ when temperature was lower in the incommensurate phase, but were essentially identical in $\gamma_{33}(\omega)$. Evaluation of the integrals appearing in the equations (4.2.22) was carried out in several different approximations. For $T>T_i$, we first used the dispersion curve of $\Omega_{\Sigma_2}(q)$ determined by Iizumi et al.[11] and integrated over the full Brillouin zone. We then used the parabolic approximation (equation (4.3.24)) and integrated over a cylindrical volume (with its axis along **a**) which was equal to one-half the volume of the Brillouin zone, then multiplied the result by 2. These two procedures gave indistinguishable results. Also, the integrals were insensitive to change in the integration volume, demonstrating that the integral is dominated by a small volume element centered at the minimum. Consequently we used the second procedure for $T>T_i$, and also for $T<T_i$ but without multiplication by 2 in this case.

The calculated results (with $D=0$, $g_3 \neq 0$) are shown in figure 4.4.1 with $C_{33}'(\omega)$ on the left and $\gamma_{33}(\omega)$ on the right. The top pair of figures (figure 4.4.1(a)) are the first terms of equations (4.2.22) ($C_{33}^{o}+2g_3\rho_o^2$ and γ_{33}^{o}), the second pair (figure 4.4.1(b)) are the Landau-Khalatnikov terms, and the third pair (figure 4.4.1(c)) are the anharmonic contributions found from the integrals. For reasons to be discussed below, we performed this calculation with three different values of the phason gap $\Omega_\phi(0)=0$, 60 and 160 GHz. The bottom pair (figure 4.4.1(d)) are the total $C_{33}'(\omega)$ and $\gamma_{33}(\omega)$ obtained by adding these three contributions. Clearly the size of the phason gap has only a minor effect on $C_{33}'(\omega)$ but causes major changes in the values of $\gamma_{33}(\omega)$ with a saturation effect for large values of $\Omega_\phi(0)$ which totally suppress the phason contribution.

Comparison of figures 4.4.1 and 3.3.2 makes clear the importance of using a consistent theory. Indeed, the rounding of $C_{33}'(\omega)$ and $\gamma_{33}(\omega)$ above T_i, which is very distinct in the experimental data as shown in figure .3.3.2, cannot be

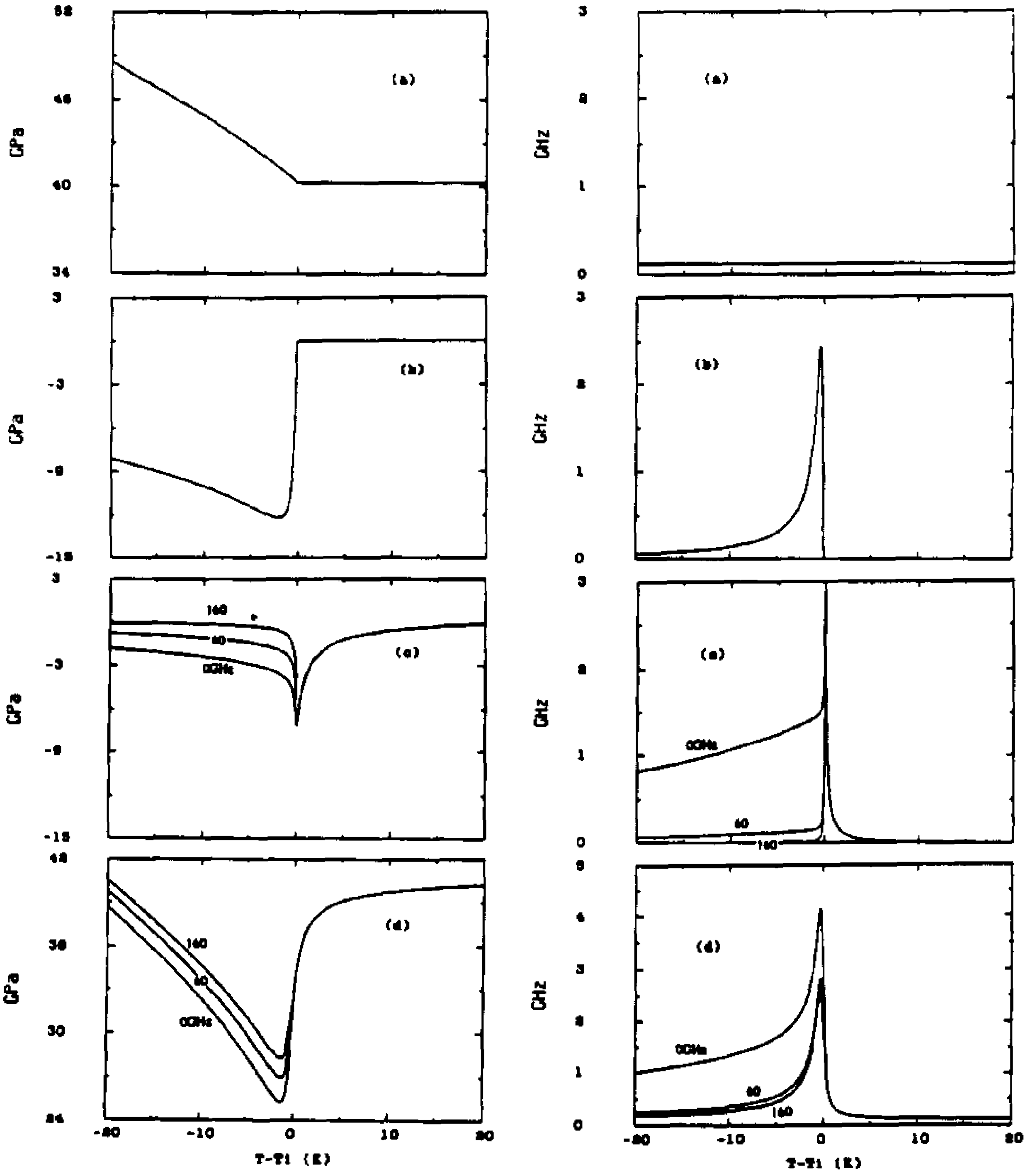

Figure 4.4.1. Theoretical predictions for the anomaly in $C_{33}(\omega)$ [left] and $\gamma_{33}(\omega)$ [right] calculated by equations (4.2.22). Top pair (a): the first terms of equation (4.2.22). Second pair (b): the Landau-Khalatnikov contribution. Third pair (c): anharmonic contributions from third-order coupling to pairs of soft modes ($T>T_i$) or pairs of amplitudons or phasons ($T<T_i$). Three values for the phason gap were used: $\Omega_\phi(0) = 0$, 60 and 160 GHz. Bottom pair (d): total values of $C_{33}(\omega)$ and $\gamma_{33}(\omega)$.

obtained without including the fluctuation terms (figure 4.4.1(c)). Conversely, once the contribution of both the phason and the amplitudon are taken into account, $\gamma_{33}(\omega)$ is too large below T_i (figure 4.4.1(c)) if a phason gap is not introduced in the phason dispersion curve.

Figure 4.4.2 shows the comparison of our 90° Brillouin scattering results with the calculated theoretical predictions (both with $D=0$, $g_3 \neq 0$ and vice-versa) using 160GHz for the phason gap which was obtained indirectly by Topic et al.[T2] in a recent NMR study of K_2SeO_4. The agreement is fair, which is already important for the primary test of the theoretical treatment in view of the large uncertainties in some of the numerical values we have used (second column of table I).

To further test the Landau free energy approach, we subsequently carried out a non-linear least squares fit in which the coefficients B, h_3 and D (with $g_3 = 0$) or g_3 (with $D=0$) were varied in order to optimize the fit to the 90° Brillouin scattering data. Figure 4.4.3 shows the optimized fits obtained either with $D=0$ ($g_3 \neq 0$) or with $g_3 = 0$ ($D \neq 0$). A better fit is obtained for the $g_3 = 0$ ($D \neq 0$) case. The resulting values of the parameters from the best fits are given in the third column of table I. Comparison of the values in the third column with those in the second column shows that excellent agreement between the theoretical calculation and experimental data can be achieved with only slight adjustments of the values of B, h_3, and D or g_3, and these small changes are within the experimental accuracy.

The calculations and the fits shown in figures 4.4.2 and 4.4.3 were obtained with a phason gap $\Omega_\phi(0) = 160$GHz. Other values larger than approximately 100GHz would also be acceptable, producing only minor changes in the four adjusted parameters. Lower values would lead to the values of $\gamma_{33}(\omega)$ too large at low temperature to agree with our experimental data. Note that

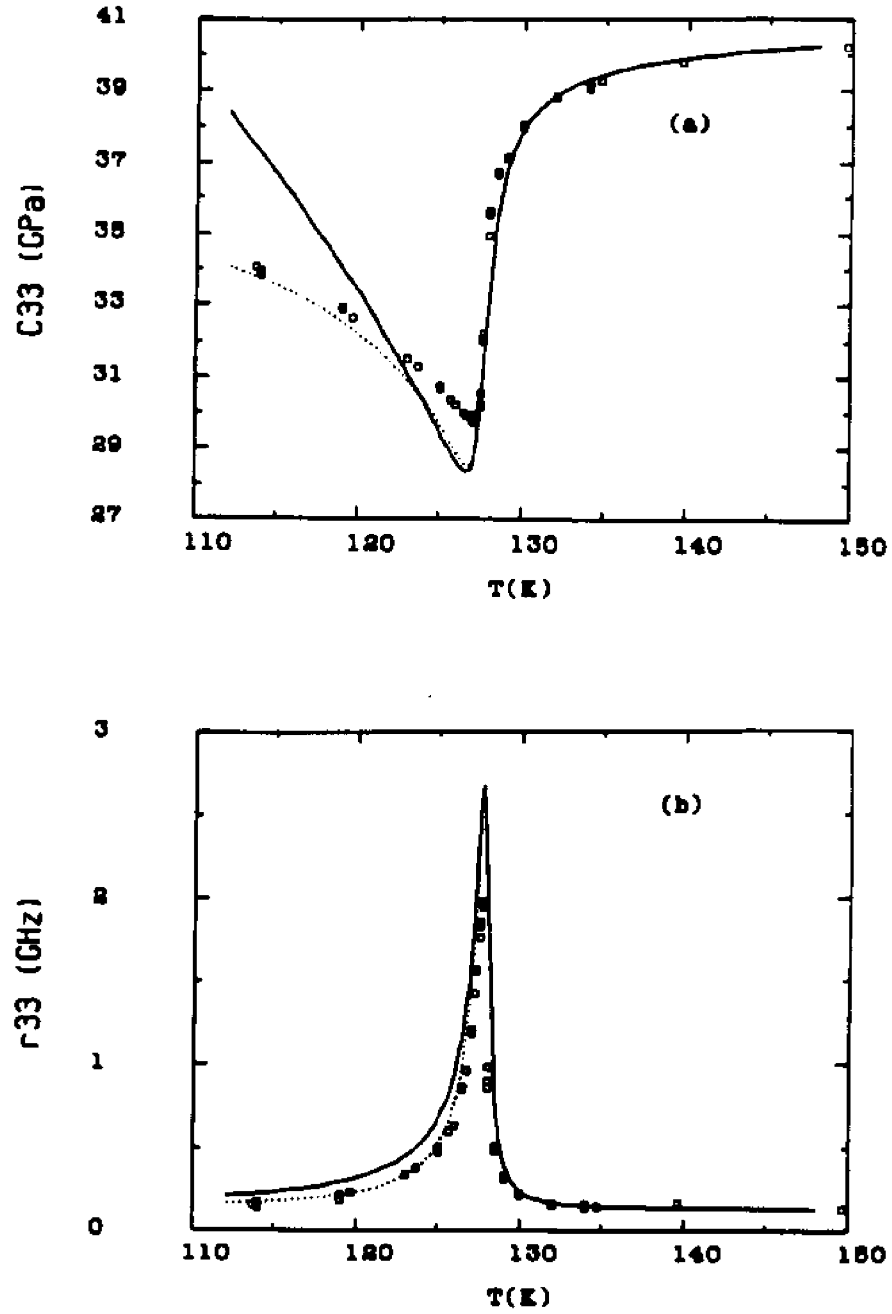

Figure 4.4.2. Comparison of the 90° Brillouin data of figure 3.3.2 with the theoretical predications of figure 4.4.1 for (a) $C_{33}(\omega)$ and (b) $\gamma_{33}(\omega)$. Solid lines: $D=0$, $g_3 \neq 0$. Dotted lines: $g_3 = 0$, $D\neq 0$. The theoretical calculations include a phason gap of Ω_ϕ = 160GHz. The free energy coefficients used were those listed in the second column of table 1.

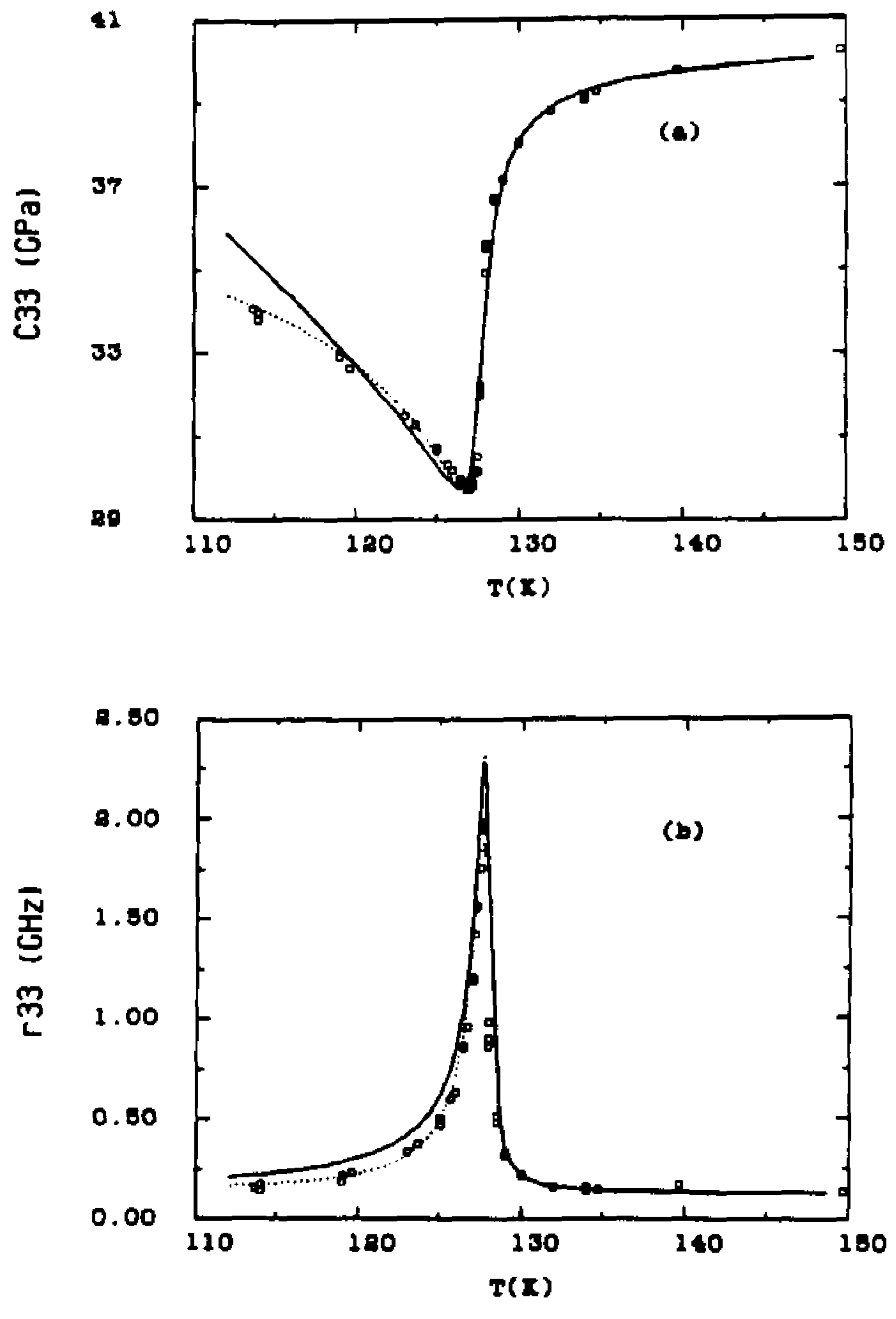

Figure 4.4.3. The best fits of the theoretical results to the experimental data of (a): $C_{33}(\omega)$ and (b): $\gamma_3(\omega)$. The best fits of (a) and (b) were obtained simultaneously by adjusting the coefficients B, h_3, and g_3 or D. The resulted values of these coefficients are listed in column 3 of table I.

the lower limit on $\Omega_\phi(0)$ deduced form this analysis is slightly above the upper limit, 85GHz, deduced from the neutron scattering data (as shown in figure 2.1.2) of Quilichini and Currat[Q1].

Using the same values in the third column of table I, we further checked our theoretical results against the 180° Brillouin scattering $C'_{33}(\omega)$ and $\gamma_{33}(\omega)$ data which have been shown in figure 3.3.3. Figure 4.4.4 shows the comparison of the theoretical results and the experimental data. Again the agreement is quite convincing in the $g_3 = 0$, $D \neq 0$ case.

From the above results, we conclude that a consistent mean field theory can explain our Brillouin scattering results for the C_{33} acoustic anomaly of K_2SeO_4 near the normal-incommensurate phase transition.

c. Comparison with previous studies

As has been mentioned in chapter 2, the $C_{33}(\omega)$ acoustic anomaly in K_2SeO_4 near the normal-incommensurate phase transition has been studied previously by several investigators. However, the analysis of the effect in all of these investigations was incomplete.

Yagi et al.[Y4][C3] were the first group to study the $C_{33}(\omega)$ anomaly near T_i. In their theoretical analysis, they used the same free energy expansion as our equation (4.1.15), but adding a term $\delta_3\epsilon_3\rho^4$ for completeness. Their result included both the bilinear coupling and anharmonic contributions, but with all coefficients treated as adjustable parameters. Also they did not consider the q_o, $-q_o$ degeneracy of the soft mode above T_i and the role of phasons below T_i. They assumed that the soft mode dispersion curve is isotopic, and that $\rho_0(T)$ is always small enough so that all equations can be linearized in $(T-T_i)$. Although they obtained reasonable fits of their theoretical expressions to their experimental results, in view of the assumptions they made and the fact that

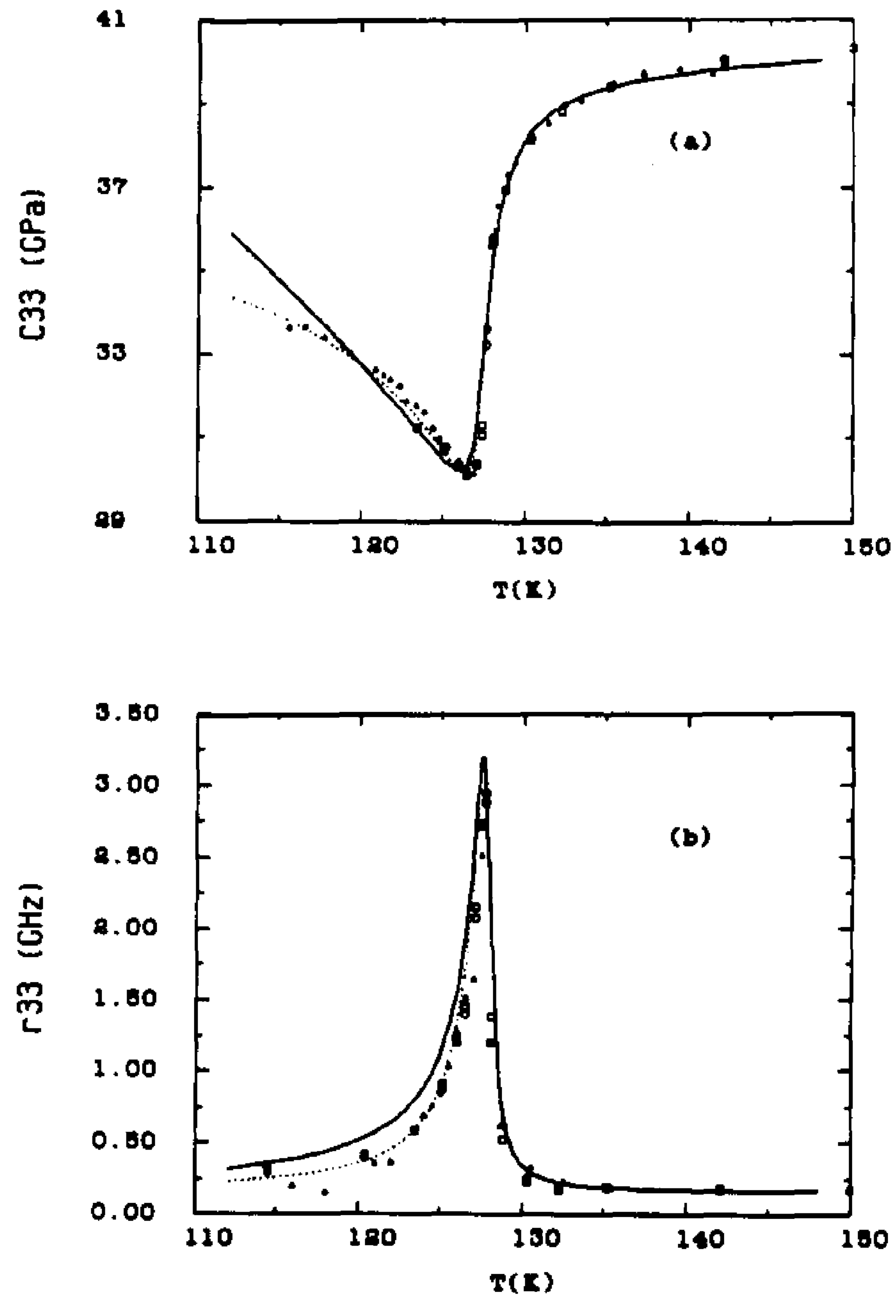

Figure 4.4.4. Comparison of the 180° Brillouin data of figure 3.3.3 with the theoretical results of equations (4.2.22) computed with the same parameters used in figure 4.4.3. (a): $C_{33}(\omega)$, (b): $\gamma_3(\omega)$. Data points are: triangles - Paris, squares - New York.

the linewidth was not analyzed, the values of the fitting parameters they found cannot be expected to be physically significant.

Rehwald et al.[R1] compared ultrasonic and Brillouin data for $C_{33}'(\omega)$ and were the first to measure $\gamma_{33}(\omega)$. They also presented a careful theoretical analysis of the harmonic contributions to $C_{33}'(\omega)$. They pointed out a a further coupling of C_{33} to the amplitudon and phason at $\mathbf{K} = \delta\, \mathbf{a}^*$ arising from a $p_3\epsilon_3\rho^3$ term, linearized to $p_3\epsilon_3\rho_0^3\rho$ below T_i. They concluded that this effect was presumably too small to be measured and did not attempt any fit.

Hauret and Benoit[H2 determined both $C_{33}'(\omega)$ and $\gamma_{33}(\omega)$ in 90° Brillouin scattering experiment. They analyzed their data starting from a free energy similar to our equation (4.1.15) with $D=0$, but considered only the Landau-Khalatnikov term, ignored anharmonic effects. This procedure did not enable them to analyze the rounding off of $C_{33}'(\omega)$ and $\gamma_{33}(\omega)$ above T_i and the corresponding effects below T_i. The relaxation time they found $\tau = \tau_0(T_i-T)^{-1}$ with $\tau_0 = 2.6\times10^{-12}$s is in fair agreement with our value of $\tau_0 = 2.1\times10^{-12}$s obtained from table I. Having set $D=0$, they could not explain the downward curvature of $C_{33}'(\omega)$ below T_i and had to use a non-mean field critical exponent for $\rho_0(T)$ $(2\beta \approx 0.75)$ in order to achieve a reasonable fit through the $g_3\rho_0^2$ term of equation (4.2.22c). This group[L4] subsequently extended their Brillouin scattering studies with 45°, 90° and 135° which illustrated the ω dependence of $\tilde{C}_{33}(\omega)$. They confirmed their previous value of $\tau_0 = (2.85\pm0.20)\times10^{-12}$s.

Esayan and Lemanov[E2] performed ultrasonic measurements, and were the first to take into account the role of the $\mathbf{K} \approx 0$ phason. Again within the Landau-Khalatnikov approximation, they simply mentioned the absence of the coupling of the strain ϵ_3 to this excitation.

The analysis employed in a recent Brillouin scattering of Rb_2ZnBr_4 and Rb_2ZnCl_4 by Horikx et al.[H8] is similar to ours. They included both the Landau-Khalatnikov and anharmonic fluctuation terms, but did not include phason contributions. Since inelastic neutron scattering studies of these materials did not show any propagating soft modes[D3][D4][Q2], their fits could not be carried out using independent dynamical data as inputs. Furthermore, the anomalies in these materials are very small compared to that of the C_{33} in K_2SeO_4, making the analysis much less significant.

5. HIGHER ORDER CORRECTION AND BEYOND MEAN FIELD APPROXIMATION

a. 3-dimensional XY model

The theoretical analysis we have employed to derive predictions for $C_{33}'(\omega)$ and $\gamma_{33}(\omega)$ was based on the framework of a mean field approximation with the usual Landau assumption of $A(T) = A_0(T-T_i)$ in equation (4.1.15). It was, however, necessary to include a phason gap (assumed temperature independent) in the calculation in order to obtain good agreement between the theory and the experimental results. Although a $\mathbf{K} = 0$ gap in the excitation spectrum of the phason was observed experimentally[Q1][I2][T2], it is not predicted by the mean field theory. Thus the phason gap used in our analysis is an additional assumption. We note that Gooding and Walker[G4] have suggested that the phason branch may actually be gapless and that the observed apparent gap could result from phason-acoustic phonon interactions.

There is extensive evidence which indicates deviations of the critical behave of K_2SeO_4 at the normal-incommensurate phase transition from the mean field approximation. As has been mentioned in chapter 2, the critical exponent found by Majkrzak et al.[M1] was $2\beta = 0.75$. The temperature dependence of the soft mode frequency $\Omega^2_{\Sigma_2}(q_o)$ obtained by Iizumi et al.[I1] (as shown in figure 4.3.1) clearly shows upward curvature. A non-linear least squares fit of their data to the relation of $\Omega^2_{\Sigma_2}(q_o) \propto (T-T_i)^{\gamma}$ gives $\gamma = 1.3$. Andrews and Mashiyama[M6][A9] carried out x-ray scattering and dielectric constant measurements in Rb_2ZnCl_4 which is isomorphous to K_2SeO_4, and found the critical exponents $2\beta = 0.69$, $\gamma = 1.26$ and $\nu = 0.693$. All these values of the critical exponents show clear deviations from the mean field values of $2\beta = 1$, $\gamma = 1$ and $\nu = 1/2$. In the incommensurate phase of K_2SeO_4, Unruh et al.[U1] have found that the dielectric anomaly behaves as $\Delta\chi \propto (T_i-T)^{0.76}$, while the frequency of the amplitudon $\Omega^2_A(0) \propto (T_i-T)^{0.52}$. They also found that the damping constant Γ_A of the amplitudon deduced from their Raman data increased strongly near T_i. We found that their results can be well described, as shown in figure 4.5.1, by

$$\Gamma_A = \left[-0.089(T_i-T)+9.6+\frac{300}{(T_i-T)^2+21}\right]cm^{-1}. \tag{4.5.1}$$

We note that similar strong increases in the soft mode linewidth have been observed in many materials undergoing structural phase transitions[S13], but no theoretical explanation for this effect yet exists. These non-mean field effects have not been taken into account in our analysis.

To proceed with our analysis beyond the mean field approximation would require a complete theory. Although some ingredients are already available, such a complete theory has not yet been established. As has been discussed in chapter 2, K_2SeO_4 is a 3-dimensional system with a 2 component order parameter. Critical exponents for the 3-dimensional XY model have been estimated by LeGuillon and Zinn-Jastin[L11][L12] ($2\beta = 0.691$, $\gamma = 1.316$ and $\nu = 0.669$). By using a crossover theory which accounts for the crossover from singular

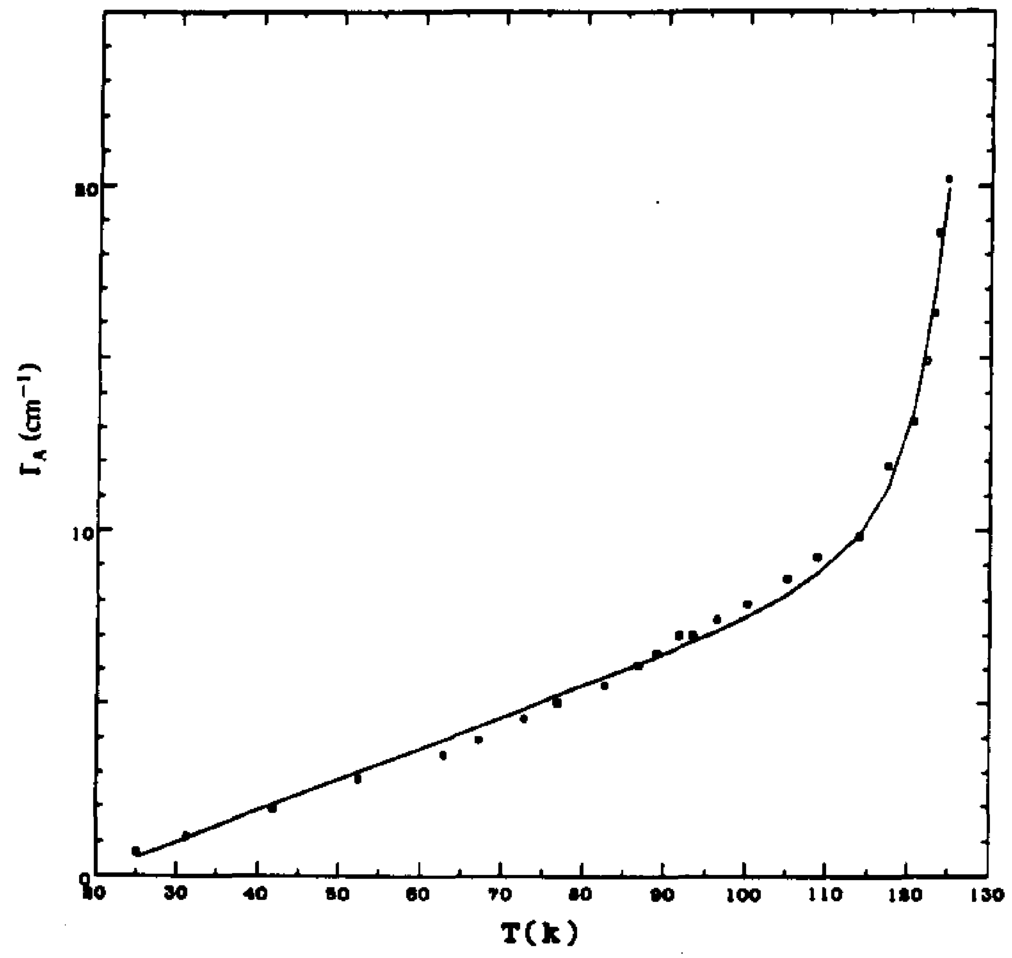

Figure 4.5.1. Best fit to the damping constant of the amplitudon $\Gamma_A(0)$. Squares are the experimental results from Unruh et al.[U1]. Solid line is the result of equation (4.5.1).

critical behavior to regular classical behavior, Chen[C7] has successfully analyzed the specific heat data of K_2SeO_4[C2][A7] and Rb_2ZnCl_4[L2] based on the 3-dimensional XY model. However, the crossover and scaling effects on the lattice dynamics in the A_2BX_4 class of materials has not been investigated.

Some of the basic theory for a scaling analysis of the acoustic anomalies in incommensurate crystals has been developed by Schwabl and his co-workers[S10][S11][I5][D3]. They also noted that the usual separation of the acoustic anomaly into independent Landau-Khalatnikov and anharmonic contributions may not be correct in the context of a scaling theory[D3]. Hu et al.[H9] have carried out a scaling analysis in their ultrasonic studies of $NaNO_2$.

In the absence of a complete theory, there is no straightforward way to carry out an analysis of the C_{33} acoustic anomalies beyond the mean field approximation. Generally, one cannot modify the temperature dependence of any property without simultaneously changing others. To illustrate, we carried out an analysis with equations (4.2.22) and used the damping constant of the amplitudon Γ_A found by Unruh et al.[U1] (equation (4.5.1)) rather than the linear temperature dependence form of equation (4.3.26). We found that even with the adjustment of the coefficients B, h_3, D or g_3, no satisfactory agreement can be achieved between the theoretical values and the experimental results. Figure 4.5.2 shows the best fit (solid lines) for the $g_3 = 0$, $D \neq 0$ case. The disagreement is evident. We then used a non-mean field amplitudon frequency $\Omega_A^2(0) \propto (T_i - T)^\gamma$ to replace the mean field result of equation (4.1.25a) with γ as a free parameter. The best fit is also shown in figure 4.5.2 by the dotted lines (for the $D=0$ $g_3 \neq 0$ case). Good agreement can be achieved again, but the fit gave a value of $\gamma \approx 0.66$ rather than $\gamma = 0.52$ found by Unruh et al.[U1] or $\gamma = 1.3$ predicted by the XY model.

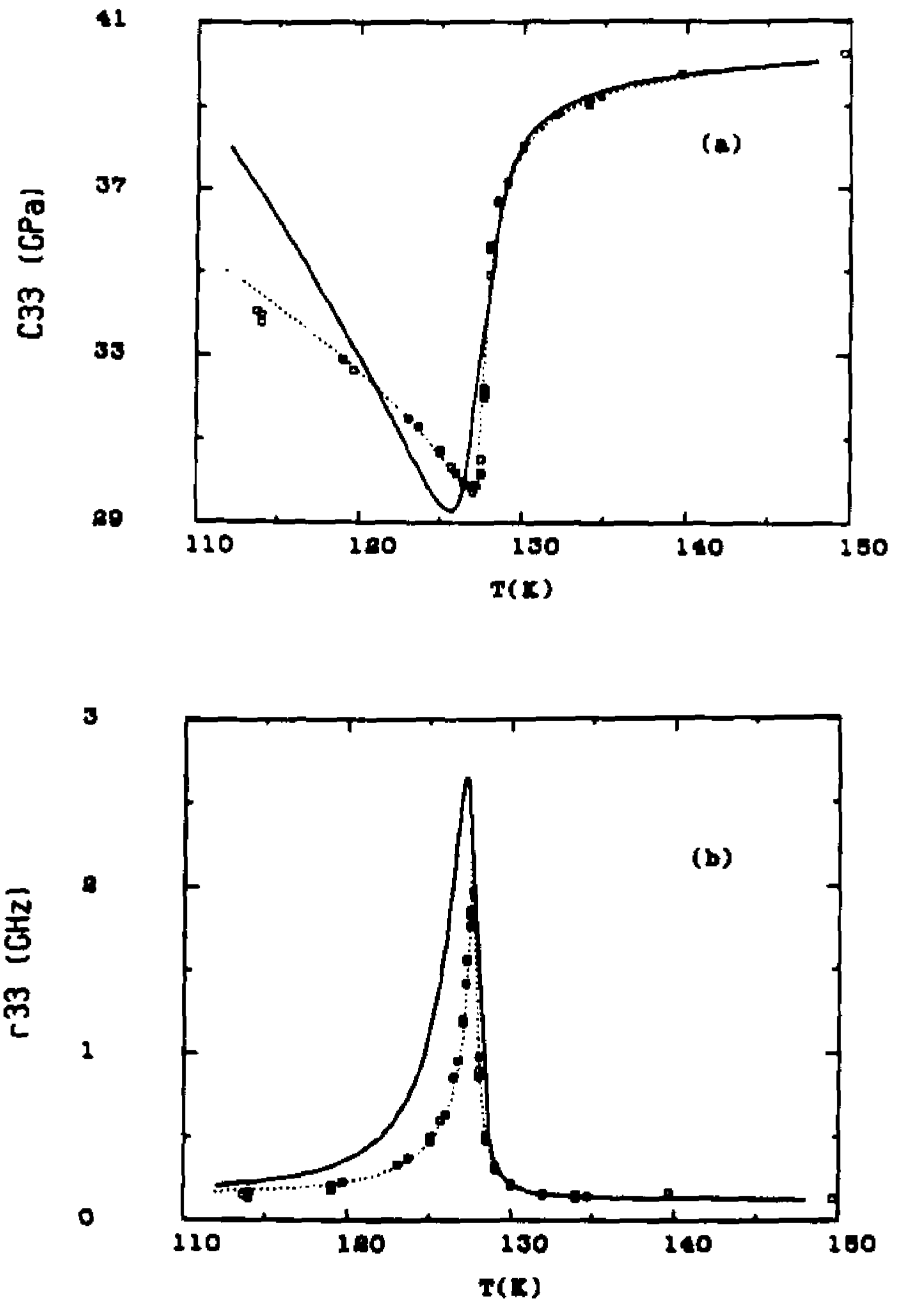

Figure 4.5.2. Fits to (a) $C_{33}(\omega)$ and (b) $\gamma_{33}(\omega)$ using Unruh's amplitudon damping constant from equation (4.5.1). Solid lines: best fit with mean field amplitudon frequency. Dotted lines: best fit with $\Omega_A^2(0) \propto (T_i - T)^{\gamma}$. The fitting results were: $\gamma = 0.66$, $B = 2.5\times10^{42}\ g^{-1}s^{-2}cm$, $h_3 = 3.8\times10^{26}\ s^{-1}$, and $g_3 = 0.72\times10^{28}\ s^{-2}$ (with D=0).

b. Higher order coupling corrections

In deriving the theoretical expressions of $C'_{33}(\omega)$ and $\gamma_{33}(\omega)$ (equations (4.2.22)), the anharmonic contributions were treated only in the lowest order approximation. We have only included the coupling of an acoustic mode to a pair of Σ_2 soft modes above T_i, and to a pair of amplitudons and a pair of phasons below T_i. Recently, Levanyuk et al.[L14] noted that in the incommensurate phase the higher-order couplings may have an important effect in the anharmonic contributions . Their preliminary results are expressed as

$T>T_i$:

$$\tilde{C}_{33}(\omega) = C_{33}^{o} - \frac{8k_BT}{(2\pi)^3}h_3^2\int\frac{dq}{\Omega_{\Sigma_2}^2(q)[2\Omega_{\Sigma_2}^2(q)-i\omega\Gamma_{\Sigma_2}(q)]} \qquad (4.5.2a)$$

$T<T_i$:

$$\tilde{C}_{33}(\omega) = (C_{33}^{o}+2g_3\rho_o^{\,2}) - \frac{(2h_3-4g_3\epsilon_3^{o})^2\rho_o^{\,2}}{\Omega_A^2(0)-i\omega\Gamma_A(0)}$$

$$-\frac{k_BT}{(2\pi)^3}(2h_3-4g_3\epsilon_3^{o})^2\left\{[1-\frac{3\Omega_A^2(0)+8D\rho_o^{\,4}}{\Omega_A^2(0)-i\omega\Gamma_A(0)}]^2\int\frac{dq}{\Omega_A^2(q)[2\Omega_A^2(q)-i\omega\Gamma_A(q)]}\right.$$

$$\left.+[1-\frac{\Omega_A^2(0)}{\Omega_A^2(0)-i\omega\Gamma_A(0)}]^2\int\frac{dq}{\Omega_\phi^2(q)[2\Omega_\phi^2(q)-i\omega\Gamma_\phi(q)]}\right|. \qquad (4.5.2b)$$

It is important to note that in their results (equations (4.5.2)) the fluctuation integrals for the amplitudons and phasons now have different weights. The anharmonic contribution from phasons is weighted by $[1-\frac{\Omega_A^2(0)}{\Omega_A^2(0)-i\omega\Gamma_A(0)}]^2$ and thus will be largely suppressed at low temperature when $\frac{\omega\Gamma_A(0)}{\Omega_A(0)} \ll 1$. This is the main difference from our analysis in which we need to introduce a phason gap to suppress the phason contribution. Also it is interesting to note that the introduction of the D and g_3 terms does not affect the weight of the phason contribution, whereas the weight of the anharmonic contribution from amplitudons is affected by the D term.

Equations (4.5.2) are a preliminary result. In a trial analysis using the values of the free energy coefficients given in the second column of table I, we found that the $C'_{33}(\omega)$ and $\gamma_{33}(\omega)$ of equations (4.5.2) showed some unexpected behavior (fluctuating rapidly) near T_i in the incommensurate phase. A more careful reexamination of their results (which is currently in progress) will be required in order to carry out further analyses.

CHAPTER V

ELASTIC ANOMALIES OF TRANSVERSE ACOUSTIC MODES AROUND T_i AND T_c

1. C_{44} TRANSVERSE ACOUSTIC ANOMALIES

a. Theory

As shown in figures 2.1.6, 2.1.7, and 3.3.5, the C_{44} elastic constant of K_2SeO_4 exhibits anomalies in the normal phase and the incommensurate as well as the commensurate phases. In the normal phase, C_{44} continuously decreases with decreasing temperature, while in the incommensurate and commensurate phases, C_{44} gradually increases with further decreasing temperature. A similar C_{44} anomaly was also observed in incommensurate Rb_2ZnCl_4, an isomorph of K_2SeO_4, by Ultrasonic[H10] and Brillouin scattering[L15] measurements.

Besides the anomalies of the elastic constant, the Brillouin scattering intensity of this C_{44} acoustic mode also exhibits abnormal changes in the normal, incommensurate and commensurate phases. This Brillouin intensity anomaly strongly suggested that the C_{44} acoustic anomalies are caused by a coupling mechanism.

The variation of C_{44} in the normal phase is an indication of a bilinear interaction between the strain ϵ_4 and an ordering quantity which should have the same symmetry type as ϵ_4 and should have its wavevector at the zone center. Because the C_{44} transverse acoustic modes measured by Ultrasonic or Brillouin scattering methods belong to the B_{3g} representation, Hirotsu et al.[H10] suggested, in analyzing their Rb_2ZnCl_4 ultrasonic data, that the ordering quantity might be the zone center mode of the Σ_2 branch (on which the soft mode occurs at $q = q_o$) which belongs to the representation of either B_{3g} or A_u. Because of the softening of the Σ_2 branch, this zone center mode exhibits decreasing frequency in the normal phase as shown in the neutron scattering results[I1] of figures 1.2.3 and 4.3.1. Rehwald et al.[R1] also used this assumption in explaining their C_{44} Ultrasonic and Brillouin K_2SeO_4 data. However, previous Raman scattering studies[W1][M8] and our new Raman scattering experiments have not been able to observe the zone center mode (~ 25 cm^{-1} at room temperature) of the soft Σ_2 branch. Furthermore, theoretical simulation results[H5] indicated that the symmetry of the zone center mode on the soft Σ_2 branch belongs to the A_u representation rather than B_{3g} which is Raman active. Therefore, the assumption of bilinear coupling of the C_{44} acoustic mode with the zone center mode of the Σ_2 soft branch is unlikely, although it is possible that the mode actually is of B_{3g} symmetry but has an extremely small Raman cross-section.

Nevertheless, Raman scattering studies[W1] of K_2SeO_4 have shown that the lowest frequency B_{3g} optical model (~ 50 cm^{-1}) did show softening in the normal phase. We also performed Raman scattering measurements to study this B_{3g} mode. Figure 5.1.1 shows three Raman spectra of this B_{3g} mode at different temperatures, and figure 5.1.2 shows the temperature dependence of the squared B_{3g} mode frequency (Ω_B^2) deduced from the Raman spectra. It shows clearly that the temperature dependence of the Ω_B^2 is very similar to that of the C_{44} elastic constant. The data of Ω_B^2 above and below T_i can be well represented (solid lines in figure 5.1.2) by

$$\Omega_B^2(T) = [8.82(T-T_i)^{0.83}+2084](\mathrm{cm}^{-1})^2, \quad (T>T_i) \qquad (5.1.1a)$$

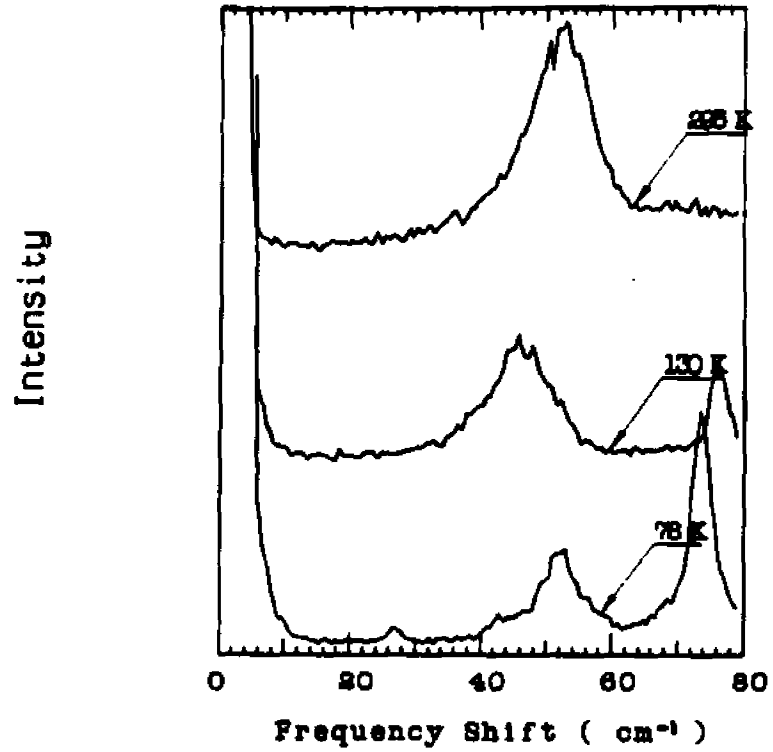

Figure 5.1.1. Raman scattering spectra of K$_2$SeO$_4$ at 295, 130, and 78K in the b(c, b)a scattering geometry, showing the temperature dependence of the lowest B$_{3g}$ optical mode.

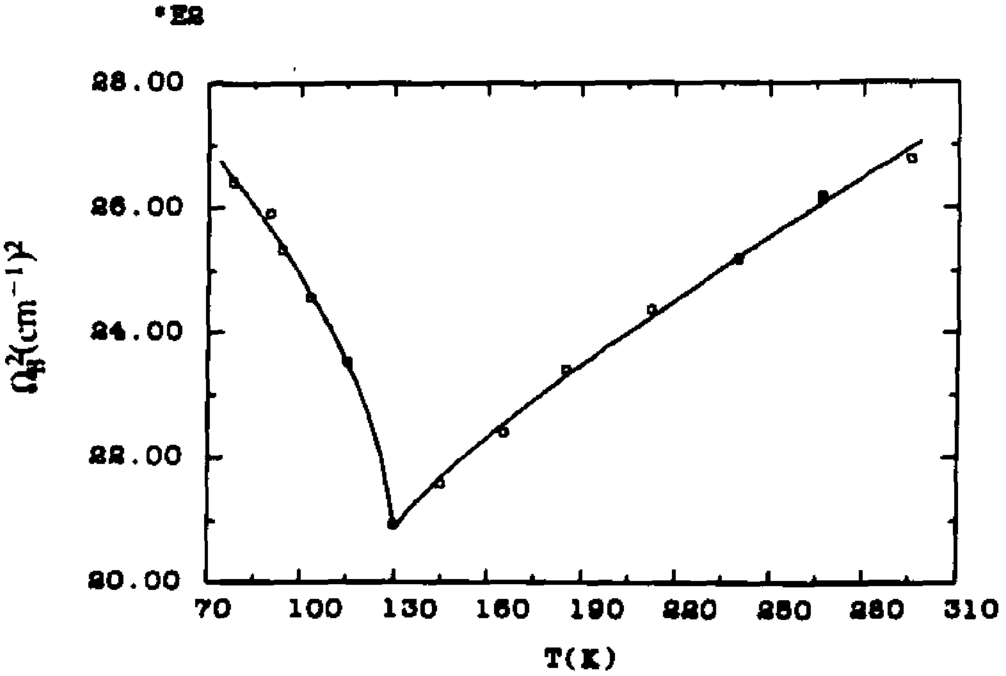

Figure 5.1.2. Squares of the lowest B$_{3g}$ optical mode frequency as a function of temperature. Solid lines are the calculated results of equations (5.1.1)

$$\Omega_B^2(T) = [52(T_i-T)^{0.60}+2084](cm^{-1})^2, \quad (T<T_i) \qquad (5.1.1b)$$

where we take $T_i = 129.5K$. Taking This B_{3g} optical mode as the ordering quantity, we then can explain the C_{44} anomaly in the normal phase. We leave aside the origin of the temperature dependence of this mode, and proceed to consider its interaction with the C_{44} acoustic mode phenomenologically.

The equation of motion for the coupled B_{3g} optical mode and the C_{44} acoustic mode can be derived from the Largrangian density as we have done in section 2 of chapter 4. If we denote the normal-mode coordinate of the B_{3g} optical mode by Q_B with $Q_B Q_B^* = \rho_B^2$, then the potential and kinetic energy density for the B_{3g} optical mode and the C_{44} acoustic mode can be written

$$U = \frac{1}{2}\Omega_B \rho_B^2+\frac{1}{2}C_{44}^o \epsilon_4^2+a_4 \rho_B \epsilon_4, \qquad (5.1.2)$$

$$T = \frac{1}{2}\dot{\rho}_B^2+\frac{1}{2}\frac{\rho_m}{q^2}\dot{\epsilon}_4^2, \qquad (5.1.3)$$

where C_{44}^o is the "bare" elastic constant, a_4 the coupling constant, ρ_m the density of the crystal and q the wavevector of the C_{44} acoustic mode. Including the external driving force and a Rayleigh dissipation function

$$F_{ext} = -\sigma_4 \epsilon_4 - \rho_B f_B, \qquad (5.1.4)$$

$$F_R = \frac{1}{2}\Gamma_B \dot{\rho}_B^2+\frac{1}{2}\frac{\rho_m}{q^2}\gamma_{44}\dot{\epsilon}_4^2, \qquad (5.1.5)$$

following the same procedures used in section 2 of chapter 4, we find the theoretical expressions for the temperature dependence of the elastic constant $C'_{44}(\omega)$ and the damping constant $\gamma_{44}(\omega)$

$$C'_{44}(\omega) = C_{44}^o - \frac{a_4^2(\Omega_B^2-\omega^2)}{(\Omega_B^2-\omega^2)^2+(\omega\Gamma_B)^2}, \quad (T>T_i) \qquad (5.1.6a)$$

$$\gamma_{44}(\omega) = \gamma_{44}^o + \frac{q^2}{\rho_m}\frac{a_4^2\Gamma_B}{(\Omega_B^2-\omega^2)^2+(\omega\Gamma_B)^2}, \quad (T>T_i) \qquad (5.1.6b)$$

where σ_4, f_B, Γ_B, and γ_{44} are the driving stress associated with ϵ_4, driving force for the B_{3g} mode, damping constant of the B_{3g} mode and the C_{44} acoustic mode, respectively. For $\Omega_B \gg \omega, \Gamma_B$, which is true in our case, the above results can be simplified by dropping terms in ω^2 and $\omega\Gamma_B$, whence

$$C_{44}'(0) = C_{44}^{o} - \frac{a_4^2}{\Omega_B^2(T)}, \qquad (T>T_i) \qquad (5.1.7a)$$

$$\gamma_{44}(0) = \gamma_{44}^{o} + \frac{q^2}{\rho_m}\frac{a_4^2\Gamma_B}{\Omega_B^4(T)}. \qquad (T>T_i) \qquad (5.1.7b)$$

Equation (5.1.7a) is the well know bilinear coupling result which has been discussed by many authors[M7][B7][R3]. It predicts that the decrease of $\Omega_B(T)$ will cause a decrease of the C_{44} elastic constant, providing a possible explanation to the C_{44} elastic anomaly in the normal phase.

In the incommensurate and commensurate phases, the C_{44} acoustic mode still can bilinearly couple with the same zone center optical mode as in the normal phase because both of them still have the same symmetry and belong to the B_2 representation in the commensurate phase. Therefore, equations (5.1.7) are also valid below T_i, providing that the $\Omega_B^2(T)$ takes the values of equation (5.1.1b).

In the incommensurate and commensurate phases, the C_{44} acoustic mode also can couple with the modulation wave through the quadratic coupling term $g_4\rho^2\epsilon_4^2$ term appearing in the free energy of equation (4.1.2c). It is also well know that this coupling will lead to a modification of the C_{44} elastic constant proportional to the square of the order parameter

$$\Delta C_{44}' = 2g_4\rho_o^2, \qquad (5.1.8)$$

where ρ_o is the equilibrium value of the order parameter given by equations (4.2.2c) and (4.2.2d). The C_{44} elastic constant in the incommensurate and commensurate phases is then given by

$$C'_{44}(0) = C^{o}_{44} - \frac{a_4^2}{\Omega_B^2(T)} + 2g_4\rho_o^2. \quad (T<T_i) \qquad (5.1.9)$$

Equations (5.1.7a) and (5.1.9) together describe the temperature variations of the C_{44} elastic constant in the high temperature normal phase and the low temperature incommensurate and commensurate phases.

b. Comparison of theory with experiment

To compare the theory with experimental results, we first fitted equation (5.1.7a) to the C_{44} data in the normal phase ($T>T_i$) in which C^{o}_{44} and a_4 were treated as adjustable parameters and $\Omega_B^2(T)$ was determined by equation (5.1.1a). The best fit was obtained with $C^{o}_{44} = 17.1$ GPa and $a_4 = 3.0\times10^{18}$ $g^{1/2}cm^{-1/2}s^{-2}$. Keeping these values of C^{o}_{44} and a_4, we then fit equation (5.1.9) to the low temperature ($T<T_i$) C_{44} data with g_4 as the only adjustable parameter. $\Omega_B^2(T)$ was determined by equation (5.1.1b), while ρ_o^2 was calculated by the mean-field results of equations (4.3.22) and the evaluated free energy coefficients listed in the third column of table I (with $g_3 = 0$). We obtained the best fit with $g_4 = 1.8\times10^{27}s^{-2}$. Figure 5.1.3 shows the comparison of the calculated results of equations (5.1.7a) and (5.1.9) with the C_{44} experimental results. The agreement between the theory and the C_{44} data is excellent.

In our analysis the theory coupled-mode theory was used consistently. To explain the C_{44} anomaly in the normal phase, a bilinear coupling of the C_{44} acoustic mode with a "soft" B_{3g} optical mode is required. Whereas once the bilinear coupling is invoked in the normal phase, its contribution in the incommensurate and commensurate phases was also considered on the same basis.

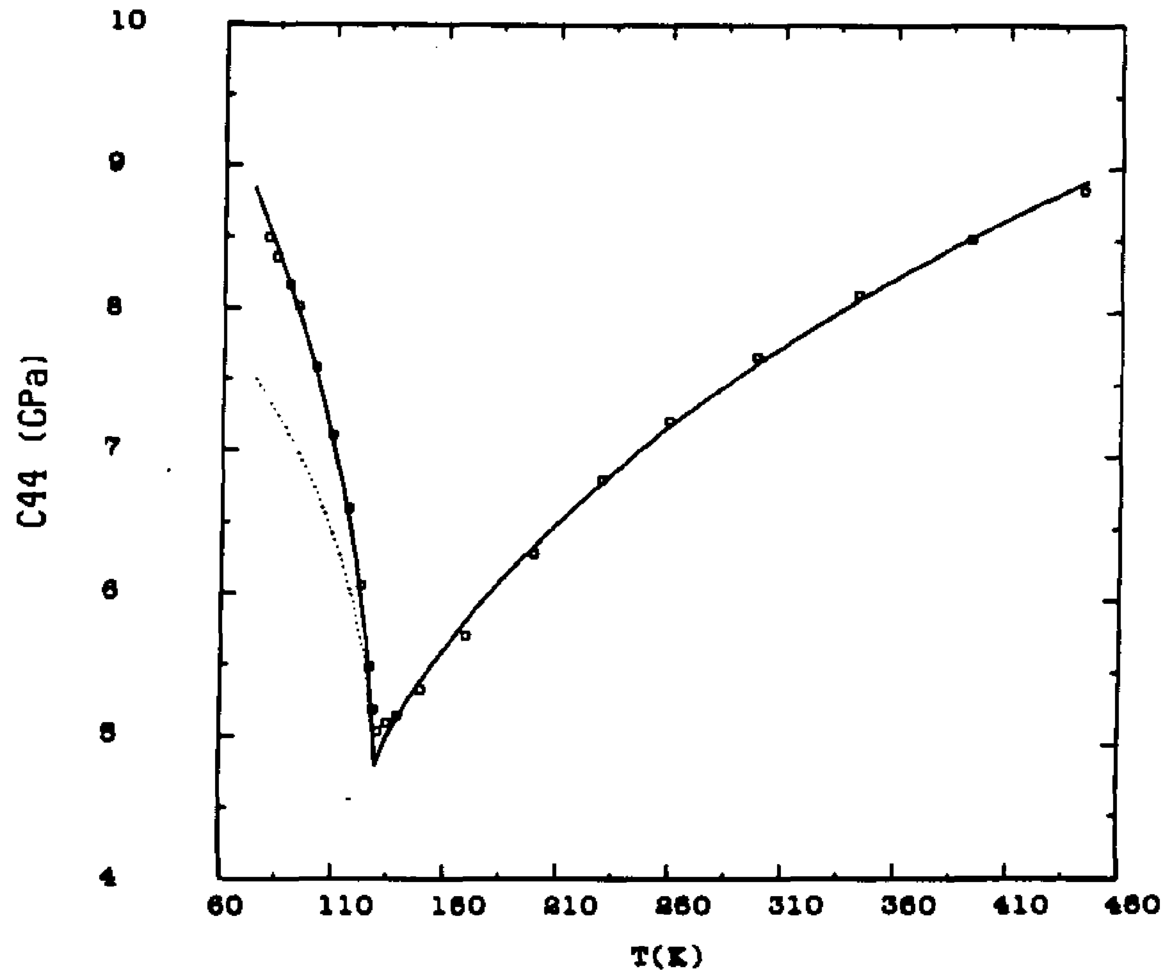

Figure 5.1.3. Comparison of the experimental data (squares) with the best fit results of equations (5.1.7a) and (5.1.9) (solid lines). $\Omega_B^2(T)$ was determined by equations (5.1.1) and ρ_0^2 was calculated by using equations (4.3.22) with the evaluated free energy coefficients listed in the third column of table I. The best fit was obtained with $C_{44}^0 = 17.1$GPa, $a_4 = 3.0\times10^{18}g^{1/2}cm^{-1/2}s^{-2}$ and $g_4 = 1.8\times10^{27}s^{-2}$. The dotted line in the low temperature phases ($T<T_i$) is the result of the first two terms in equation (5.1.9), showing the contributions of the bilinear coupling in the low temperature phases.

The anomaly of the damping constant γ_{44} due to the bilinear coupling can be estimated by using equation (5.1.7b). With $q = 2.8\times10^5 cm^{-1}$ (90° scattering and $\lambda_{laser} = 488nm$), $\rho_m = 3.05gcm^{-3}$, $\Gamma_B \approx 300GHz$ and the above fitted a_4 value, we found that the maximum variation of $\gamma_{44}(0)$ is $(\Delta\gamma_{44})_{max} = \frac{q^0}{\rho_m}\frac{a_4^2}{\Omega_B^2(T_i)} \approx 13$ MHz. Such a small variation is beyond our experimental accuracy of ~ 100MHz and explains why the damping anomaly is not observed in our measured attenuation results as shown in figure 3.3.6(a).

An analysis of the low temperature ($T<T_i$) C_{44} data using equation (5.1.9) with a non-mean field $\rho_0^2 \propto (T_i-T)^{2\beta}$ was also attempted, with β as a free parameter. Good agreement was achieved with $2\beta = 0.70$, in agreement with the result of the 3-dimensional XY model ($2\beta = 0.691$)[L11][L12].

c. Previous studies

The C_{44} elastic anomaly of K_2SeO_4 and the isomorph Rb_2ZnCl_4 were investigated by several groups. Hirotsu et al.[H10] were the first to observe the C_{44} anomaly of Rb_2ZnCl_4 around the normal-incommensurate phase transition by ultrasonic measurement. Noting the considerable decrease of C_{44} with decreasing temperature in the normal phase, they suggested a possible explanation of bilinear coupling of the C_{44} acoustic mode with the zone center mode of the soft Σ_2 branch, providing that there was also a soft Σ_2 branch in Rb_2ZnCl_4 like that in K_2SeO_4 and that the zone center mode on the branch belonged to B_{3g} rather than A_u representation. Because neutron scattering studies on Rb_2ZnCl_4 did not show such a soft Σ_2 branch, their suggestion for Rb_2ZnCl_4 is questionable.

Rehwald et al.[R1] analyzed their high temperature ($T>T_i$) ultrasonic and Brillouin C_{44} data in the framework of Landau theory including bilinear coupling of ϵ_4 to an ordering quantity. This theory leads to an elastic Curie-Weiss law, $C_{44}(T) = C_{44}^{o}\frac{T-T_o^{(\sigma)}}{T-T_o^{(\epsilon)}}$. Based on Hirotsu's assumption, they then compared their fitted results ($T_o^{(\sigma)} = 5K$ for ultrasonic and $T_o^{(\sigma)} = 70K$ for Brillouin) with the extrapolated transition temperature (they found T_o~72K, but from Fig. 7 of Iizumi et al.[I1] we found T_o~5K) for the zone center mode on the Σ_2 soft branch measured by Iizumi et al.[I1], and they concluded that Hirotsu's assumption fitted well with their Brillouin results. Because of the B_{3g} symmetry they assumed for the zone center mode on the soft Σ_2 branch, their comparison may not be meaningful. Also their interpretation of the difference of their C_{44} ultrasonic and Brillouin data in the normal phase (the ultrasonic C_{44} curve is less bent than that of Brillouin results) by crystal imperfection is not correct. Note that they did not measure the Brillouin C_{44} directly because the Brillouin intensity is too weak, they obtained it by analyzing mixed modes. We found that our C_{44} Brillouin results are closer to their ultrasonic results than their Brillouin results. In analyzing the low temperature C_{44} results, they simply fitted the data in the incommensurate and commensurate phase to a power law and obtained an exponent 0.71.

Hoshizaki et al.[H1] also studied the C_{44} anomaly of K_2SeO_4 by Ultrasonic measurements. Matsuda et al.[M9] and Luspin et al.[L15] investigated the C_{44} anomaly of Rb_2ZnCl_4 by ultrasonic measurement and Brillouin scattering, respectively. All of them analyzed their low temperature data ($T<T_i$) by linearly extrapolating the C_{44} variation in the normal phase to the low temperature phases and fitted the difference of the data with the extrapolation to a power law expression. Hoshizaki et al. obtained an exponent 0.68, Matsuda et al. 0.61 and Luspin et al. 0.60. Without considering the mechanism of the softening of the C_{44} acoustic mode in the normal phase, their results are not

physically significant.

2. C_{55} TRANSVERSE ACOUSTIC ANOMALY AROUND T_c

a. Theory

Ultrasonic and Brillouin scattering studies of K_2SeO_4 [R1][E2] have shown that the C_{55} elastic constant exhibited significant variations around the lock-in phase transition. It can be clearly seen in figures 2.1.6 and 2.1.7 that C_{55} decreases dramatically when temperature approaches T_c from above and then gradually increases below T_c. Our Brillouin C_{55} results in figure 3.3.5 also show the same variation in the incommensurate phase. We lack the low temperature data below T_c because of the vanishing of Brillouin scattering intensity. The unusual decrease of the scattering intensity near T_c, as shown in figures 3.3.7(b) and 3.3.8(b), is a good indication of coupling effect.

The C_{55} elastic anomalies have been analyzed by Rehwald et al.[R1][R2] and Esayan et al.[E2] in the framework of Landau theory. It has been shown that the C_{55} anomalies can be well described with the fourth-order coupling term $\epsilon_5 Q^3$ by which the C_{55} acoustic mode interacts with the amplitudon and phason in the incommensurate phase and the coupling with the phason causes the large C_{55} anomaly near T_c.

The theoretical expression for the C_{55} elastic constant can be derived by using the free energy of equations (4.1.2). For simplicity, we just keep terms containing ϵ_5 and Q and write

$$F = F_Q + \frac{1}{2} C_{55}^0 \epsilon_5^2 + g_5 \epsilon_5^2 Q Q^* + \frac{1}{2} a_5 \epsilon_5 (Q^3 + Q^{*3}). \tag{5.2.1}$$

where F_Q is the part of the free energy which depends only on the normal mode coordinates and is given by equation (4.1.17a). In the plane wave approximation, the free energy associated with the time dependent fluctuations of the normal coordinate Q in the presence of the static distortion ρ_o is

$$\delta F = \delta F_Q + \frac{1}{2}(C_{55}^o + 2g_5\rho_o^2)\epsilon_5^2$$

$$+\frac{3}{2}a_5\epsilon_5[<Q(q_o)>^2Q(K_i+q_o)+<Q(-q_o)>^2Q(-K_i-q_o)], \qquad (5.2.2)$$

in which wavevector conservation requires

$$K_i = a^* - 3q_o = 3(q_c - q_o) = a^*\delta(T), \qquad (5.2.3)$$

where q_c is the commensurate wavevector $q_c = a^*/3$, and $\delta(T)$ is the mismatch parameter. In obtaining equation (5.2.2), we have used the redefinition equation (4.1.21) and dropped all terms high than quadratic in Q or ϵ_5. In the incommensurate phase, the new normal modes, amplitudon and phason, are defined in equations (4.1.24). Using these definitions and equation (4.1.26a), equation (5.2.2) can be rewritten as

$$\delta F = \Omega_A^2(K_i)P_A(K_i)P_A^*(K_i) + \Omega_\phi^2(K_i)P_\phi(K_i)P_\phi^*(K_i) + \frac{1}{2}(C_{55}^o + 2g_5\rho_o^2)\epsilon_5^2$$

$$+\frac{3}{2\sqrt{2}}a_5\epsilon_5\rho_o^2\{[P_A(K_i) - iP_\phi(K_i)] + c.c.\}. \qquad (5.2.4)$$

Taking this free energy as the potential energy, including the damping constants Γ_A, Γ_ϕ, and γ_{55} phenomenologically for the amplitudon, phason, and C_{55} acoustic mode, respectively, the same dynamical calculation we used in section 2 of chapter 4 leads to the well-known result

$$\tilde{C}_{55}(\omega) = (C_{55}^o + 2g_5\rho_o^2)$$

$$-\frac{9}{4}a_5^2\rho_o^2[\frac{1}{\Omega_A^2(K_i) - \omega^2 + i\omega\Gamma_A(K_i)} + \frac{1}{\Omega_\phi^2(K_i) - \omega^2 + i\omega\Gamma_\phi(K_i)}]. \qquad (5.2.5)$$

Since $\Omega_A(K_i) \gg \Omega_\phi(K_i) \gg \omega$, the above equation can be simplified by dropping the amplitudon and ω^2 term. Then we have

$$C'_{55}(\omega) = (C^{o}_{55}+2g_5\rho_o^2)-\frac{9}{4}a_5^2\rho_o^4\frac{\Omega_\phi^2(K_i)}{\Omega_\phi^4(K_i)+[\omega\Gamma_\phi(K_i)]^2}, \qquad (5.2.6a)$$

$$\gamma_{55}(\omega) = \gamma^{o}_{55}+\frac{9}{4}\frac{q^2}{\rho_m}a_5^2\rho_o^4\frac{\Gamma_\phi(K_i)}{\Omega_\phi^4(K_i)+[\omega\Gamma_\phi(K_i)]^2}, \qquad (5.2.6b)$$

where γ^{o}_{55} is the background damping of the C_{55} acoustic mode.

According to equation (4.3.27b), we have

$$\Omega_\phi^2(K_i) = \frac{1}{2}\Lambda_x K_i^2. \qquad (5.2.7)$$

For K_2SeO_4, the value of Λ_x is given in table I. According to Iizumi et al.[I1], the temperature dependence of the mismatch parameter $\delta(T)$ can be described by

$$\delta(T) = \frac{0.07}{1+0.002(T_i-T)^2}, \qquad (5.2.8)$$

with $T_i = 127.5K$. Due to the continuous decrease of K_i from $0.07a^*$ at T_i to $0.02a^*$ at T_c, $\Omega_\phi(K_i)$ decreases similarly which causes the decrease of C_{55}.

The above theoretical treatment has been utilized by Rehwald et al.[R1][R2] and Esayan et al.[E2] in analyzing their C_{55} ultrasonic data. Note that in the above treatment we have used the plane wave approximation for the modulation wave in the incommensurate phase. However we know that near T_c in the incommensurate phase the modulation wave evolves into phase solitons[B2]. Therefore the plane wave approximation is not valid near T_c. Dvorak and Hudak[D5] carried out theoretical studies for the C_{55} elastic constant of A_2BX_4-type crystals in the domain-like regime in the incommensurate phase near T_c. They found that the anomalous part of C_{55} is proportional to the domain wall density n_D, a result anticipated by Rehwald and Vonlanthen[R2]. In the constant amplitude approximation, their theory leads to the result

$$C_{55}'(0) = C_{55}^{\infty} + C_{55}^{\infty}\left(1 - \frac{C_{55}^{\infty}}{C_{55}^{o}}\right)\left(\ln\frac{4}{\sqrt{c(T-T_c)}}\right)^{-1}, \qquad (5.2.9)$$

where C_{55}^{o} and C_{55}^{∞} are the 'bare' elastic constants in the normal and commensurate phases, respectively. c is a positive constant. This result predicts a decrease of C_{55} near T_c in the incommensurate phase.

b. Comparison with experiments

To analyze our Brillouin C_{55} results, we first fitted the data in the normal phase to a linear temperature dependence and obtained the background elastic constant

$$C_{55}^{o} = 16.0-0.0051T \quad \text{(GPa)}. \qquad (5.2.10)$$

We then fitted equation (5.2.6a) to the data in the incommensurate phase with $\Omega_{\phi}^{2}(K_i)$ calculated by using equations (5.2.3), (5.2.7) and (5.2.8), ρ_o^2 determined by equations (4.3.22) and the values in the third column of table I (mean-field result), and $\Gamma_{\phi}(K_i)$ obtained from equation (4.3.26) (a linear temperature dependence of the damping constants of phason used by Quilichini et al.[Q1] in their neutron scattering studies of phason in K_2SeO_4). Taking $\omega = 9.9$GHz (Brillouin frequency of the C_{55} acoustic mode at room temperature), treating a_5 and g_5 as adjustable parameters, we obtained the best fit with $a_5 = 1.9\times10^{34}\ g^{-1/2}cm^{1/2}s^{-2}$ and $g_5 = 8.8\times10^{26}\ s^{-2}$. Figure 5.2.1 shows the comparison of the calculated results of equations (5.2.6a) and (5.2.10) (solid lines) with the C_{55} experimental results. The agreement is good in view of the large uncertainties in the low temperature C_{55} data.

Rehwald et al.[R2] have found that the theoretical result of equation (5.2.6a) deviated from their Ultrasonic C_{55} data near the lock-in transition.

They interpreted it as the effects of solitonlike discommensurations described by the sine-Gorden equation (4.1.10). Our C_{55} data also indicates the same departure from the theory as shown in figure 5.2.1. However, the poor precision of our C_{55} data near T_c prevent us from carrying out a quantitative analysis. Rehwald et al.[R2] and Dvorak et al.[D5] have tried to fit the C_{55} ultrasonic data[R1] of K_2SeO_4 by a logarithmic law as given in equation (5.1.9) and they found that it was too steep to agree with the data. Dvorak and Hudak concluded that within the constant amplitude approximation a quantitative explanation to the temperature dependence of C_{55} of K_2SeO_4 is questionable.

In correspondence with the analysis of the C_{33} anomalies in chapter 4, we also carried out an analysis of equation (5.2.6a) using non-zero phason gaps with

$$\Omega_\phi^2(K_i) = \Omega_\phi^2(0) + \frac{1}{2}\Lambda_x K_i^2. \tag{5.2.11}$$

For the reasons mentioned in chapter 4, $\Omega_\phi(0) = 60\text{GHz}$ and $\Omega_\phi(0) = 160\text{GHz}$ were considered. For the case of $\Omega_\phi = 60\text{GHz}$ the best fit of equation (5.2.6a) to the C_{55} data was obtained with $a_5 = 2.3\times10^{34}\text{g}^{-1/2}\text{cm}^{1/2}\text{s}^{-2}$ and $g_5 = 11\times10^{26}\text{s}^{-2}$, while for $\Omega_\phi(0) = 160\text{GHz}$ best fit was obtained with $a_5 = 4.8\times10^{34}\text{g}^{-1/2}\text{cm}^{1/2}\text{s}^{-2}$ and $g_5 = 21\times10^{26}\text{s}^{-2}$. The calculated results of equation (5.2.6a) for these two cases are essentially identical with the result shown in figure 5.2.1 calculated by using gapless phason.

The theoretical predictions of the damping constant $\gamma_{55}(\omega)$ anomalies (equation (5.2.6b)) for $\Omega_\phi(0) = 0, 60, 160\text{GHz}$ are plotted in figure 5.2.2 (solid lines). In contrast to the equivalence of the $C_{55}(\omega)$ in the above three cases, $\gamma_{55}(\omega)$ is very sensitive to phason-gap values. It shows clearly in figure 5.2.2 that the $\gamma_{55}(\omega)$ anomaly near T_c can be largely suppressed by a phason gap of $\Omega_\phi(0) \geqslant 100\text{GHz}$. Although we were not able to trace the behavior of the C_{55}

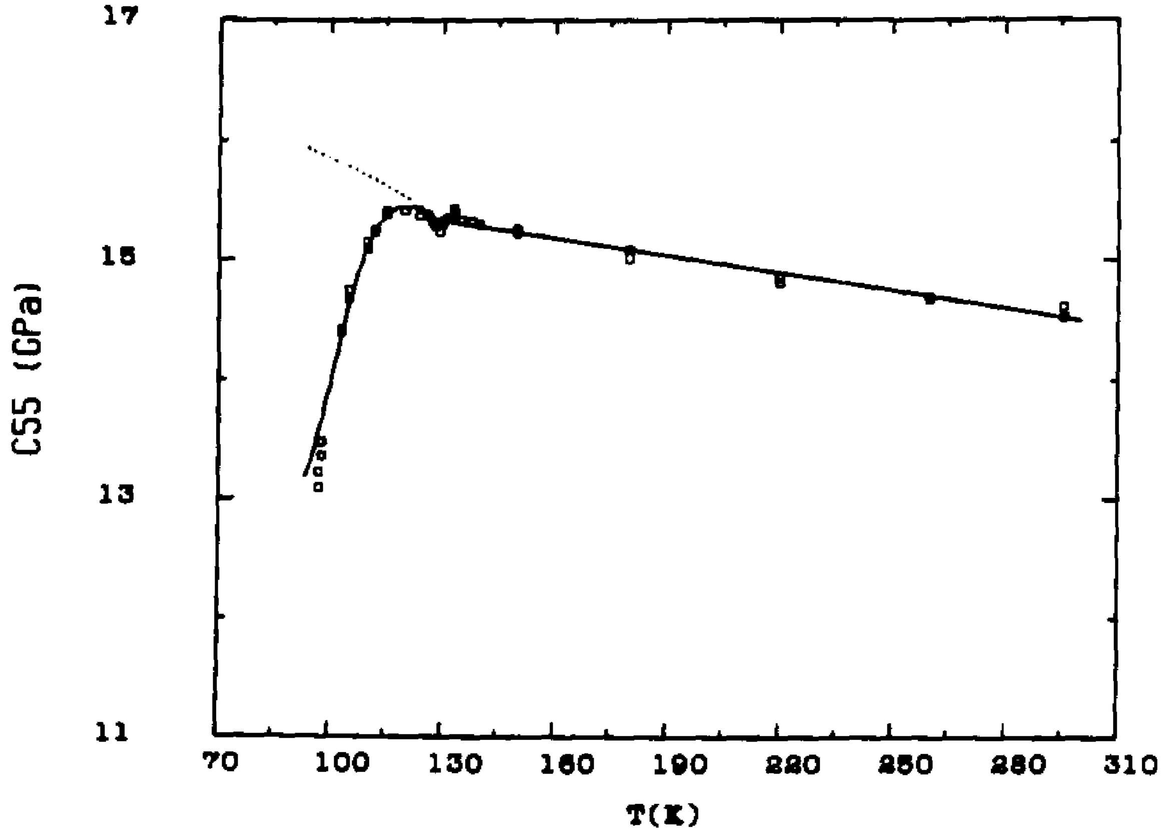

Figure 5.2.1. Comparison of C_{55} experimental data (squares) with the best fit results of equations (5.2.6a) and (5.2.10). $\Omega_{\phi}^{2}(K_i)$ was calculated by equations (5.2.7), (5.2.3) and (5.2.8) with Λ_x given in table I. Γ_{ϕ} was determined by equation (4.3.26) and ρ_o^2 was calculated by equations (4.3.22) with the coefficients in the third column of table I. The best fit was obtained with $a_5 = 1.9\times10^{34}g^{-1/2}cm^{1/2}s^{-2}$ and $g_5 = 8.8\times10^{26}s^{-2}$.

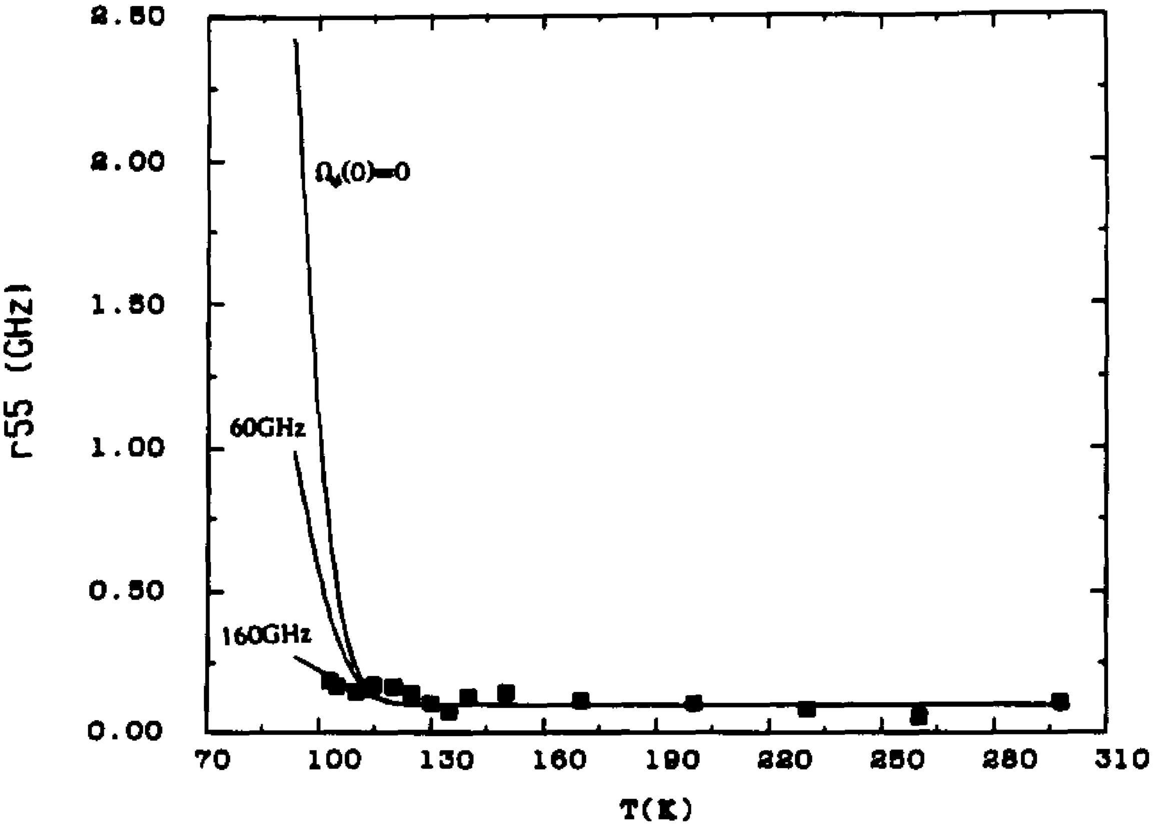

Figure 5.2.2. Temperature dependence of the damping constant $\gamma_{55}(\omega)$. solid lines are the calculated result of equation (5.2.6b). Three phason gaps are used:

(1) $\Omega_\phi(0) = 0$, $a_5 = 1.9\times10^{34} g^{-1/2} cm^{1/2} s^{-2}$, $g_5 = 8.8\times10^{26} s^{-2}$;
(2) $\Omega_\phi(0) = 60GHz$, $a_5 = 2.3\times10^{34} g^{-1/2} cm^{1/2} s^{-2}$, $g_5 = 11\times10^{26} s^{-2}$;
(3) $\Omega_\phi(0) = 160GHz$, $a_5 = 4.8\times10^{34} g^{-1/2} cm^{1/2} s^{-2}$, $g_5 = 21\times10^{26} s^{-2}$.

Other parameters are the same as that used in figure 5.2.1. Squares are the experimental results.

mode close enough to T_c because of the vanishing of the Brillouin scattering signal near T_c, a comparison of our data with the theoretical results (figure 5.2.2) indicates a preference for the result with a phason gap $\geqslant$ 100GHz, in agreement with the result of chapter 4 in which the analysis of the C_{33} anomalies required a phason gap $\Omega_\phi(0) \geqslant$ 100GHz.

3. C_{66} TRANSVERSE ACOUSTIC ANOMALY AROUND T_i

Of the three transverse elastic constants, C_{66} shows the simplest temperature dependent variation. It only exhibits a slight change of slope at T_i as shown in figure 3.3.5.

The theoretical explanation for the C_{66} elastic anomaly is straightforward. After T_i, the C_{66} acoustic mode can interacts with the order parameter through the quadratic coupling $g_6\epsilon_6^2QQ^*$ term appearing in the free energy of equation (4.1.2c). In the lowest order approximation, this coupling leads to the variation of the elastic constant

$$\Delta C_{66} = 2g_6\rho_o^2. \tag{5.3.1}$$

Then

$$C_{66}'(0) = C_{66}^o + 2g_6\rho_o^2. \tag{5.3.2}$$

In the normal phase, the C_{66} data is well described by

$$C_{66}^o = 17.6-0.0079T \quad \text{(GPa)}. \tag{5.3.3}$$

A fit of equation (5.3.2) to the C_{66} data points below T_i gives $g_6 = -5.6\times10^{26}s^{-2}$, in which, again, we used the mean-field ρ_o^2 calculated from equations (4.3.22).

Figure 5.3.1 shows good agreement between the calculated results of equation (5.3.2) (solid lines) and the experimental results.

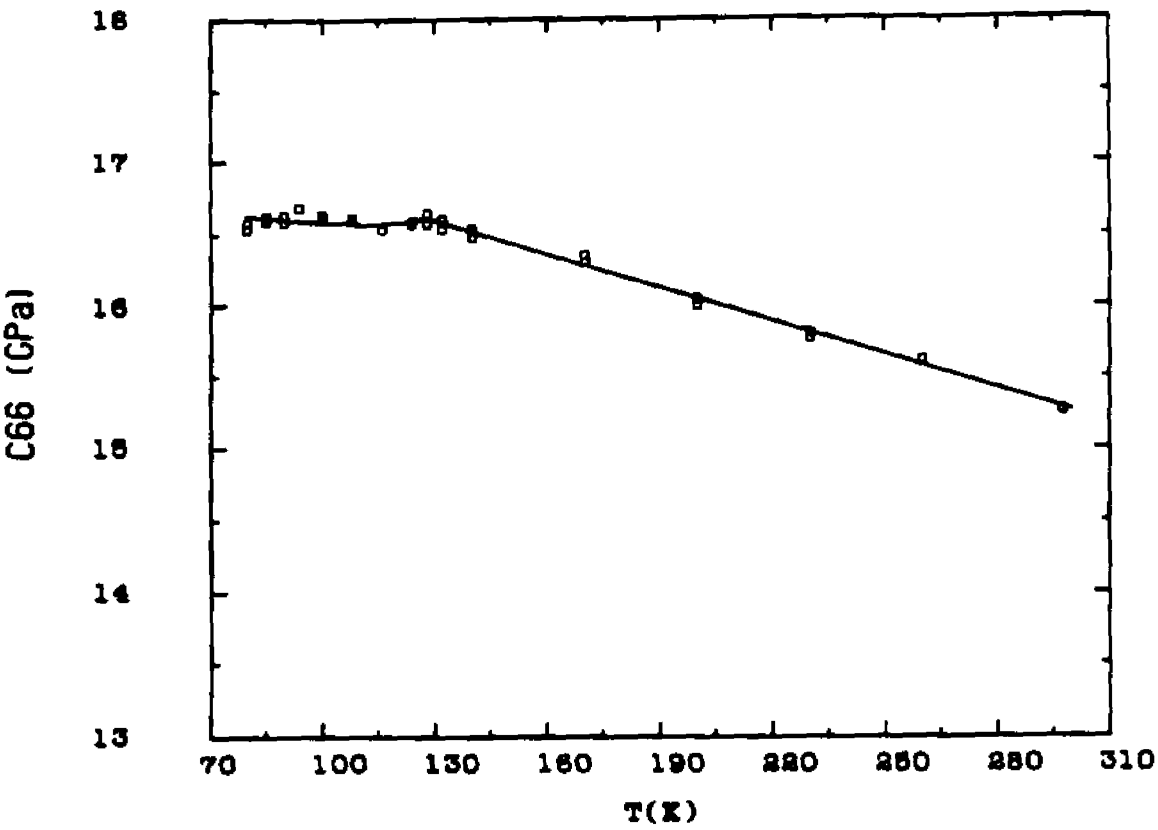

Figure 5.3.1. Comparison of C_{66} experimental data (squares) with the calculated results of equations (5.3.2) and (5.3.3). ρ_o^2 was calculated as in the figure 5.2.1. The best fit was obtained with $g_6 = -5.6\times10^{26}s^{-2}$.

4. TRANSVERSE ACOUSTIC ASYMMETRIES

a. Experimental evidence

Asymmetric behavior of transverse waves in the incommensurate phase is one of the interesting phenomena which has been observed in several incommensurate crystals.

Fritz[F4] studied the incommensurate phase transition of $BaMnF_4$ by ultrasonic measurements. He found that ultrasonic waves propagating along the a-axis (polar-axis) and polarized along b-axis underwent a larger change in velocity than the one with interchanged propagation and polarization directions.

Esayan et al.[E4] tigated the acoustic properties of $RbH_3(SeO_3)_2$ in the incommensurate and commensurate phases. They observed that the velocity and damping of the ultrasonic transverse waves propagating along the b-axis (modulation axis) and polarized along the a-axis exhibited much stronger anomalies in the incommensurate phase than the transverse waves with interchanged propagation and polarization directions.

Berge et al.[B8] also observed asymmetric behavior of transverse acoustic modes in quartz (SiO_4) crystals in the incommensurate phase by Brillouin scattering measurements. They found that the damping constant of the TA mode propagating along the y direction and polarized along the x direction showed a stronger anomaly in the incommensurate phase than the TA mode propagating along x and polarized along y.

b. Theoretical studies

Theoretical investigations of the transverse acoustic asymmetries in the incommensurate phase have been reported by several authors. Based on the framework of Landau theory, Poulet and Pick[P3] studied selection rules for light scattering by soft modes and interacting acoustic modes in displacive incommensurate structures. By considering the symmetry properties of amplitudon, phason and acoustic modes, they found that in the case of K_2SeO_4 the phason can couple with the transverse acoustic modes propagating along the b-axis (or c-axis) and polarized along the modulation axis (a-axis), but not with the transverse acoustic modes propagating along the a-axis and polarized along the b-axis (or c-axis). This result predicted transverse acoustic asymmetries in the incommensurate phase, providing that the phason coupling effect is strong enough to be observed.

Dvorak and Esayan[D4] proposed a possible explanation for the transverse acoustic asymmetry of $RbH_3(SeO_3)_2$ on basis of the Landau-type theory. From the starting point that acoustic waves propagating along a particular direction are coupled only to soft modes propagating in the same direction, they suggested that the the coupling of the transverse acoustic modes to soft modes with anisotropic dispersion curves around q_o (wavevector of the frozen-in soft mode) might cause the transverse acoustic asymmetries in the incommensurate phase. Lemanov et al.[L3] also discussed the asymmetric behavior of transverse waves in the incommensurate phase. From symmetry considerations, they obtained the same phason-acoustic phonon coupling results as Poulet and Pick[P3]. From their analysis, they pointed out that the observed asymmetry of $RbH_3(SeO_3)_2$ cannot be explained by the phason coupling effects and cannot be due to the mechanisms discussed by Dvorak and Esayan[D4]. They also studied the acoustic properties of K_2SeO_4, Rb_2ZnCl_4 and $(NH_4)_2BeF_4$ crystals by ultrasonic measurements and were not able to observe a similar asymmetry of the transverse waves within their experimental accuracy. They concluded that ultrasonic experiments cannot reveal a Goldstone phason because of its very large relaxation time.

Scott[S12] presented an explanation for the observed transverse asymmetries based on nonequilibrium defects observed in certain incommensurate crystals. He also proposed that the asymmetries do not arise from spatial dispersion as proposed by Dvorak and Esayan[D4], but from anti-symmetric contributions to the stress tensor due to local rotations caused by chiral defects which are large in incommensurates with screw axes.

Gooding and Walker[G3] developed a linear theory for long-wavelength, low-frequency vibrations in incommensurate dielectrics. Through the consideration of the rotational invariance of the Lagrangian density (extended Nelson-Lax theory[N1][N2] for incommensurate structures), they studied the coupling effects of sound-waves with phason displacement fields in incommensurate crystals. In the normal crystal structures their theory reproduces the results of Nelson and Lax[N1][N2], while in the incommensurate structure their theory indicates that a contribution to transverse acoustic attenuation due to the viscous damping of the motion of the modulation relative to the underlying crystal lattice may be present for one geometry and absent when the propagation and polarization directions are interchanged. Therefore their theory predicts a transverse acoustic asymmetry for the damping constants in the incommensurate phase. They also examined the asymmetric behavior of incommensurate $BaMnF_4$.

Subsequently, Gooding and Walker[G4] carried out analyses on the phasons and transverse sound-wave asymmetries of K_2SeO_4 in the incommensurate phase. They found that the inelastic neutron scattering data of K_2SeO_4 obtained by Quilichini and Currat[Q1], whose damped-harmonic oscillator analysis suggested a non-zero phason gap in the incommensurate phase, may also be explained by using a coupled phason sound-wave (longitudinal acoustic phonons propagating along the a-axis) theory in which the phasons are gapless.

Therefore whether or not the phasons in K_2SeO_4 are really gapless is still uncertain. However, from their further analysis of the coupling effects of transverse sound-waves with phasons, they found that coupling with gapless phasons would give very different results in the transverse acoustic asymmetries from that of phasons with a gap. Considering the high-frequency ($q \gtrsim 0.02 Å^{-1}$) and low-frequency ($q \lesssim 0.0005 Å^{-1}$) limits, their theory predicted:

(1). For gapless phasons and in the high-frequency regime

$$v_{ba} > (\text{or} <)\ v_{ab}\,, \tag{5.4.1a}$$

$$D_{ba} < D_{ab}\,, \tag{5.4.1b}$$

$$v_{ca} > (\text{or} <)\ v_{ac}\,, \tag{5.4.1c}$$

$$D_{ca} < D_{ac}\,, \tag{5.4.1d}$$

where v_{ba} is the velocity of sound-waves propagating along the b-axis and polarized along the a-axis. D_{ba} is related to the damping constant γ_{ba} of the v_{ba} sound-wave by $\gamma_{ba} = D_{ba}q^2$. Similar definitions are applied in equations (5.4.1). The $>$ (or $<$) inequality of equation (5.4.1a) pertains to the conditions of $v_{ba} > v_p$ (or $v_{ba} > v_p$), respectively, where v_p is the bare phason speed. Similarly for equation (5.4.1c).

(2). For gapless phasons and in the low-frequency regime

$$v_{ba} = v_{ab} \tag{5.4.2a}$$

$$D_{ba} > D_{ab} \tag{5.4.2b}$$

$$v_{ca} = v_{ac} \tag{5.4.2c}$$

$$D_{ca} > D_{ac} \tag{5.4.2d}$$

(3). For phasons with a gap and at sufficiently low frequencies (less then 1GHz), the attenuation asymmetries predicted by equations (5.4.2) are removed.

In the high-frequency regime, the theory of Gooding and Walker and that of Poulet and Pick predict identical sound-speed asymmetries. Following the predictions of Gooding and Walker, further experimental studies on the transverse acoustic asymmetries may provide important information for determining whether the phasons in K_2SeO_4 are gapless or not.

c. Our Brillouin scattering results

To investigate the transverse acoustic asymmetries, we studied the acoustic properties of the six transverse acoustic modes of K_2SeO_4 propagating and polarized along the crystal axes by Brillouin scattering method. The deduced elastic and damping constants corresponding to each of the transverse acoustic modes are shown in figures 3.3.5 and 3.3.6. Within our experimental accuracy of $\sim$0.6GPa for the elastic constants and $\sim$200GHz for the damping constants in the incommensurate phase, we were not able to observed acoustic asymmetric behavior for the pairs of transverse modes under interchange of their propagation and polarization directions. We conclude that Brillouin scattering cannot reveal the coupling effects of transverse sound-wave with phasons of K_2SeO_4. According to Gooding and Walker[G4], the transverse modes we measured by Brillouin scattering method ($q \approx 0.0028\text{Å}^{-1}$, $\omega \approx 10$GHz) are beyond the low-frequency regime. Besides, the experimental accuracy of the damping constants in the incommensurate phase are poor. Therefore, it is not possible to draw definitive conclusions about the phason gap from our results. Further careful ultrasonic experimental studies on the damping asymmetries of the transverse modes may provide the answer.

APPENDIX A

RAMAN SCATTERING APPARATUS

The Raman scattering apparatus is illustrated schematically in figure A.1. The Coherent model 52 Argon-ion laser (either at 4880Å or 5145Å) was operated single-line multi-mode with a usual output power of ~300mW. The laser beam was focused into sample contained in a cryostat and the scattered light was collected and focused on an intermediate slit which was used to eliminate the strong elastic scattering from the edges of the sample. The collected light was collimated and then refocused on the entrance-slit of a Spex 1401 tandem grating spectrometer. The openings of the three slits in the Spex spectrometer can be adjusted to optimize the throughput and the resolution (the highest resolution is $\sim 0.5\text{cm}^{-1}$). The settings usually used for the three slits is 100μm:200μm:100μm. The scattered light is analyzed by two gratings in tandem operation. The analyzed light was detected by a photomultiplier tube (PMT) (I.T.T, FW-130) operated at a cathode voltage of -1750 volts d.c. The PMT is cooled by a refrigerated chamber (model Te-104, Products for Research Inc.) in order to reduce the background (dark-current) emission. The electrical pulses emitted by the PMT were processed by a Canberra Industries model 813 discriminator/pre-amplifier, and the TTL signals were acquired by an AT-type computer equipped with an EG&G Ortec ACE-MCS multi-scalar board which has been described in chapter 3.

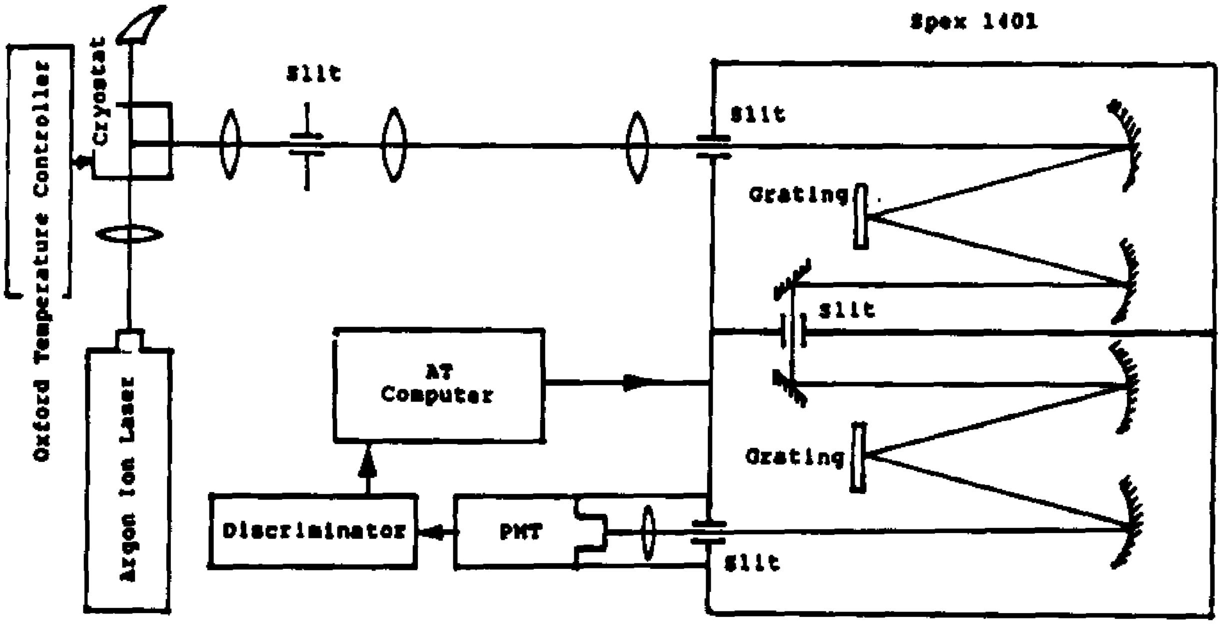

Figure A.1. Schematic illustration of the Raman scattering apparatus.

APPENDIX B

CRYOSTAT AND OXFORD TEMPERATURE CONTROLLER

The cryostat used in our experiment is an Air Products Cryo-Tip model LT-3-110 continuous flow nitrogen (or helium) cryostat. A schematic illustration of the cooling system is given in figure B.1. The cryostat has four optical windows in the four sides for light scattering experiments. The Sample is mounted in a cylindrical sample holder with four windows and the sample holder is attached to the coldfinger of the cryostat. A platinum resistance thermometer (100 Ω at room temperature) is installed in the coldfinger near the sample holder to monitor the temperature of the coldfinger and the sample. Heating wires are wound around the coldfinger for heating and temperature control. The coldfinger and sample are cooled by flowing liquid nitrogen (or helium). The temperature is controlled by an Oxford temperature controller model ITC4 which detects the temperature of the coldfinger via the platinum thermometer and applies DC power to the heater on the coldfinger.

The Oxford temperature controller is a programmable proportional controller. It can provide up to 80W of heating power. With the above platinum resistance thermometer sensor, it can control the temperature from 19K to 500K with an accuracy of ±0.1K. The cooling or heating rate can be set and automatically controlled by the built-in programmable feature of the controller. Remote computer control and monitoring is also accessible via a built-in standard RS-232 interface.

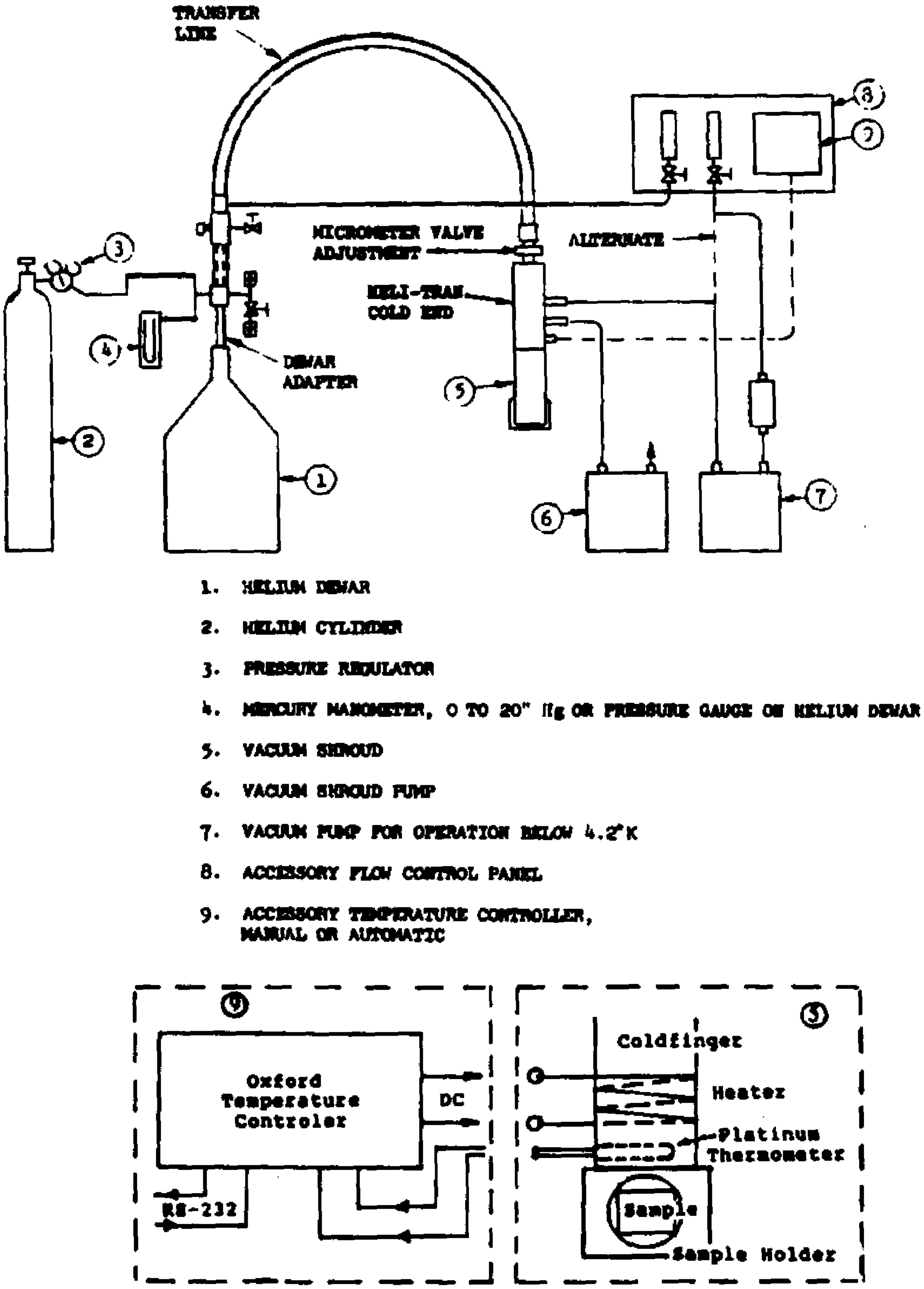

Figure B.1. Schematic illustration of the cryostat cooling system.

APPENDIX C

LISTING OF THE BRILLOUIN SPECTRUM FITTING PROGRAM

The following tandemfit.f program was developed from a standard (taurosv.f) nonlinear least-squares fitting program based on the Rosenbrock stepping method.

```
cccccccccccccccccccccccccccccccccccccccccccccccccccccccccccccccccccccccc
cccccccccccccccccccccccccccccccccccccccccccccccccccccccccccccccccccccccc
ccc
ccc     This program is written for fitting the Brillouin Scattering
ccc     spectra obtainded by the TFP system. It fits the Brillouin
ccc     peaks by the convolution of instrument-response with a damped
ccc     harmoric oscillator response.
ccc
cccccccccccccccccccccccccccccccccccccccccccccccccccccccccccccccccccccccc
cccccccccccccccccccccccccccccccccccccccccccccccccccccccccccccccccccccccc
        implicit double precision (a-h,o-z)
        character inf*15,side*8,sele,outf*18,outex*18
        common/input/r(9,3),snois,fix,npoint
        common/conv/y(4000),z(4000),mm,mm1,fsr
        common/conv11/inf,outf,outex
        common/convv/aln
     common
    c/deriva/ ng,kk

        write(6,2)
2       format(1x,'Nonlinear least squares fitting to Brillouin
    + scattering spectrum')
c       read in the file for fitting
        print'(1x/1x,"Give the input file name for fitting:")'
        read*,inf
        print*,inf
        open(8,file=inf,status='old')
        read(8,*,end=4)(y(i),i=1,4000)
4       npoint=i-1
        close (8)
        print'(1x/1x,"Give the mirror separation (in cm):")'
        read*,fsr
        print*,fsr
        aln=alog(2.0)
        do 8 i=1,npoin
8       z(i)=0.0
        j=1
        do 9 i=1,15
        if (inf(i:i) .eq. "." .or. inf(i:i) .eq. " ") goto 10
```

```
      j=i
9     continue
10    outf=inf(1:j)//".fi"
      outex=inf(1:j)//".ep"
      print'(/1x,"The output file name for the best fitted
     + data is:", /1x, a18)',outf
      print'(/1x,"The output file name for the experimental
     + data is:", /1x, a18)',outex

cget the parameters for the central,left,right Rayleigh lines

      half=1.0
      do 102 n=1,3,1
      side=' Center '
      if (n .eq. 2) then
      side=' Left  '
      half=2.0
      end if
      if (n .eq. 3) side=' Right  '
      write(6,100) side
      write(6,110)
      read*,r(n,2),r(n,3)
      print*, r(n,2),r(n,3)
      i=int(r(n,2))
      r(n,1)=y(i)/half
102   continue

c     get the parameters for the Brillouin lines
      mm=0
      do 20 k=1,2
      side=' Left  '
      if (k .eq. 2) side=' Right  '
      write(6,120) side
      read*, mm1
      print*,mm1
      do 11 i=1,mm1
      print'(1x/1x,"For mode(",i2,1x,"), enter:")',i
      write(6,110)
      mod=mm+3+i
      read*, r(mod,2),r(mod,3)
      print*,r(mod,2),r(mod,3)
      l=int(r(mod,2))
      r(mod,1)=y(l)
11    continue
      if (k .eq. 1) mm=mm1
20    continue

      print'(1x/1x,"Give  the region (in chanel numbers) for finding
     + the noise level:")'
      read*, nois1, nois2
      print*, nois1, nois2
      snois=0.0
```

```
      do 22 i=nois1,nois2
22    snois=snois+y(i)
      snois=snois/(nois2-nois1+1)
      print'(/1x,"The noise level is:")'
      print*, snois
      print'(/1x,"Fix the noise level or not?(y/n):")'
      read*,sele
      print*,sele
      fix=1.0
      if (sele .eq. 'y') fix=0.0

      kk=mm+mm1+3

      ng=1

     call minnew
100   format(1x/1x,'For the Rayleigh line at the (',a8,'), enter:')
110   format(1x,'Peak position, Width(hwhm):')
120   format(1x/1x,'Number of Brillouin mode at the (',a8,'):')
     end
     subroutine minnew
      implicit double precision (a-h,o-z)
     common
    2/parint/ x(15)    ,xt(15)     ,dirin(15)  ,maxint     ,npar
    3/parext/ u(30)    ,w(30)      ,werr(30)   ,maxext     ,nu
    6/unit  / isysrd   ,isyswr
    8/title / title(20)            ,isw(7)     ,nblock
    9/conver/ epsi, apsi  ,vtest     ,nstepq        ,nfcn       ,nfcnmx
    b/minima/ amin          ,up         ,newmin           ,itaur     ,lmi(30)
    c/deriva/ng,kk

      if (ng.lt.kk+1) go to 10
      call fcn(npar,4,amin,u,2)
      call exit

10   maxint=15
     maxext=30
     isysrd=5
     isyswr=6
     nblock=0
  110 continue
     nfcn=1
     call midata
     call intoex(x)
     call fcn(npar,ng,amin,u,1)
     call fcn(npar,ng,amin,u,4)
     call mprint(1,amin)
     call fcn(npar,ng,f,u,4)
     if(f.ne.amin) go to 160
     nfcn=3
     call comand
     go to 110
```

```
 160 continue
     write(isyswr,880) amin,f
     return
 880 format('0for the above values of the parameters, fcn is time-depen
    *dent'/'0f =',e22.14,' for first call'/' f=',e22.14,' for second')
     end
     subroutine midata
        implicit double precision (a-h,o-z)
        common/input/r(9,3),snois,fix,npoint
     common
    1/names / nam1(30)    ,nam2(30)
    2/parint/ x(15)   ,xt(15)     ,dirin(15) ,maxint     ,npar
    3/parext/ u(30)   ,w(30)      ,werr(30)  ,maxext     ,nu
    4/limits/ alim(30)    ,blim(30)  ,lcode(30) ,lcorsp(30) ,limset
    6/unit  / isysrd   ,isyswr
    8/title / title(20)              ,isw(7)    ,nblock
    9/conver/ epsi, apsi  ,vtest      ,nstepq        ,nfcn       ,nfcnmx
    b/minima/ amin            ,up          ,newmin            ,itaur      ,lmi(30)
    c/deriva/ ng,kk

     double precision dax,dbx
     equivalence(kp,maxext)
     nblock=nblock+1
     do 50 i=1,7
  50 isw(i)=0
     npfix=0
     nint=0
     nu=0
     npar=0
     k2=0
     kcard=1
     do 100 i=1,kp
     u(i)=0.0
     nam1(i)=0
     lcode(i)=0
     lcorsp(i)=0
 100 continue
     do 105 i=1,maxint
     dirin(i)=0.0
 105 continue

c       tansfer the parameters to u(i)
        do 110 i=1,3
        u(i)=r(ng,i)
110     continue

c       set step sizes,bounds for u(i)
        w(1)=u(1)/10.0
        blim(1)=u(1)*5.0
        alim(1)=0.0
        w(2)=u(3)/30.0
        blim(2)=u(2)+3*u(3)
```

```
      alim(2)=u(2)-3*u(3)
      if (ng .gt. 3) then
      u(3)=u(3)-r(1,3)
      if (u(3) .le. 0.0) u(3)=1.0
      end if
      w(3)=u(3)/20.0
      blim(3)=5.0*u(3)
      alim(3)=0.0
      ip=4
c     two gaussians for the Rayleigh at the Left and Right
      if (ng .eq. 2 .or. ng .eq. 3 ) then
      ip=7
      do 120 i=1,3
      u(i+3)=u(i)
      w(i+3)=w(i)
      blim(i+3)=blim(i)
      alim(i+3)=alim(i)
120   continue
      end if
c     noise level is in u(ip).
      u(ip)=snois
      w(ip)=u(ip)*fix/10.0
      blim(ip)=200*u(ip)
      alim(ip)=0.0

2030  do 200 i=1,ip
      nint=nint+1
      lcorsp(i)=nint
    nu=max0(nu,i)
    werr(i)=w(i)
    if(alim(i))140,130,140
  130 if(blim(i))140,135,140
  135 lcode(i)=1
    go to 160
  140 lcode(i)=4
  160 continue
  200 continue
  250 continue
    npar=nint
    call extoin(x)
    do 300 i=1,nu
    k=lcorsp(i)
    if(k)300,300,260
  260 sav=u(i)+w(i)
    b=pintf(sav,i)
    sav=u(i)-w(i)
    a=pintf(sav,i)
    dbx=dble(b-x(k))
    dax=dble(a-x(k))
    dirin(k)=(dabs(dax)+dabs(dbx))/2.0
    xt(k)=x(k)
  300 continue
```

```
      up=1.0
      isw(5)=1
        return
      end
      subroutine extoin(pint)
        implicit double precision (a-h,o-z)
      common
     1/names / nam1(30)   ,nam2(30)
     3/parext/ u(30)   ,w(30)    ,werr(30)  ,maxext    ,nu
     4/limits/ alim(30)   ,blim(30)  ,lcode(30)  ,lcorsp(30) ,limset
     6/unit  / isysrd   ,isyswr
      dimension pint(30)
      limset=0
      do 100 i=1,nu
      j=lcorsp(i)
      if(j) 100,100,50
   50 pint(j)=pintf(u(i),i)
  100 continue
      return
      end
      subroutine intoex(pint)
        implicit double precision (a-h,o-z)
      common
     1/names / nam1(30)   ,nam2(30)
     3/parext/ u(30)   ,w(30)    ,werr(30)  ,maxext    ,nu
     4/limits/ alim(30)   ,blim(30)  ,lcode(30)  ,lcorsp(30) ,limset
     6/unit  / isysrd   ,isyswr
      dimension pint(30)
      do 100 i=1,nu
      j=lcorsp(i)
      if(j) 100,100,50
   50 continue
      u(i)=pextf(pint(j),i)
  100 continue
      return
      end
      function pextf(pintj,i)
        implicit double precision (a-h,o-z)
      common
     1/names / nam1(30)   ,nam2(30)
     3/parext/ u(30)   ,w(30)    ,werr(30)  ,maxext    ,nu
     4/limits/ alim(30)   ,blim(30)  ,lcode(30)  ,lcorsp(30) ,limset
     6/unit  / isysrd   ,isyswr
      double precision dpintj
      igo=lcode(i)
      go to (100,200,300,400),igo
  100 pextf=pintj
      go to 800
  200 continue
  300 continue
  400 alimi=alim(i)
      blimi=blim(i)
```

```
   dpintj=dble(pintj)
   pextf=alimi+0.5*(dsin(dpintj)+1.0)*(blimi-alimi)
800 return
   end
   function pintf(pexti,i)
     implicit double precision (a-h,o-z)
   common
  1/names / nam1(30)   ,nam2(30)
  3/parext/ u(30)   ,w(30)     ,werr(30)  ,maxext    ,nu
  4/limits/ alim(30)   ,blim(30)   ,lcode(30)  ,lcorsp(30) ,limset
  6/unit  / isysrd    ,isyswr
   double precision dy
   data big,small /1.570796326795,-1.570796326795/
   igo=lcode(i)
   go to (100,200,300,400),igo
100 pintf=pexti
   go to 800
200 continue
300 continue
400 alimi=alim(i)
   blimi=blim(i)
   if(pexti-alimi) 440,500,460
440 a=small
450 pintf=a
   pexti=pextf(a,i)
   limset=1
   write(isyswr,241) i
   go to 800
460 if(blimi-pexti) 470,520,480
470 a=big
   go to 450
480 y=2.0*(pexti-alimi)/(blimi-alimi)-1.0
   dy=dble(1.0-y**2)
   pintf=datan(y/dsqrt(dy))
   go to 800
500 pintf=small
   go to 800
520 pintf=big
800 return
241 format(' error in pintf. variable', i3,' not within limits' )
   end
   function dexdin(x,int)
     implicit double precision (a-h,o-z)
   common
   3/parext/ u(30)   ,w(30)     ,werr(30)  ,maxext    ,nu
  4/limits/ alim(30)   ,blim(30)   ,lcode(30)  ,lcorsp(30) ,limset
   double precision dx
   do 50 i=1,nu
   lc=lcorsp(i)
   if(lc-int) 50,100,50
 50 continue
   dexdin=0.0
```

```
   go to 200
100 ld=lcode(i)
   go to (110,120,130,140),ld
110 dexdin=1.0
   go to 200
120 continue
130 continue
140 dx=dble(x)
9140 dexdin=(blim(i)-alim(i))*0.5*dabs(dcos(dx))
200 return
   end
   subroutine mprint(ikode,fval)
      implicit double precision (a-h,o-z)
   common
   1/names / nam1(30)   ,nam2(30)
   2/parint/ x(15)    ,xt(15)    ,dirin(15) ,maxint    ,npar
   3/parext/ u(30)    ,w(30)      ,werr(30)  ,maxext    ,nu
   4/limits/ alim(30)    ,blim(30)   ,lcode(30)  ,lcorsp(30) ,limset
   5/varian/ v(15,15)
   6/unit  / isysrd    ,isyswr
   8/title / title(20)               ,isw(7)    ,nblock
   9/conver/ epsi, apsi  ,vtest      ,nstepq           ,nfcn        ,nfcnmx
   b/minima/ amin            ,up          ,newmin            ,itaur      ,lmi(30)
    double precision dup,dv
    dimension dv(15,15)
    dup=dble(up)
    squp=dsqrt(dup)
    write(isyswr,1000)
    kount=0
    do 200 i=1,nu
 20 l=lcorsp(i)
    if(l.eq.0) go to 55
    if(isw(2)-1) 29,25,25
 25 if(v(l,l).lt.0.) v(l,l)=-v(l,l)
    dv(l,l)=dble( v(l,l))
    werr(i)=dexdin(x(l),l)*dsqrt(dv(l,l))*squp
 29 if(kount) 30,30,40
 30 kount=1
    write(isyswr,1001)fval,nfcn
    go to 200
 40 continue
    go to 200
 55 if(ikode.eq.0) go to 200
    if(kount) 60,60,70
 60 kount=1
    write(isyswr,1001) fval,nfcn
    go to 200
 70  continue
 200 continue
    return
1000 format(14x,' fcn value',5x,' calls')
1001 format(10x,e15.7,i7)
```

```
1002 format(' ',55x,i6,i4,1x,2a4,2x,4e13.5)
      end
      subroutine comand
        implicit double precision (a-h,o-z)
      common
     2/parint/ x(15)  ,xt(15)    ,dirin(15) ,maxint    ,npar
     3/parext/ u(30)  ,w(30)     ,werr(30)  ,maxext    ,nu
     4/limits/ alim(30)   ,blim(30)  ,lcode(30) ,lcorsp(30) ,limset
     5/varian/ v(15,15)
     6/unit  / isysrd   ,isyswr
     8/title / title(20)           ,isw(7)    ,nblock
     9/conver/ epsi, apsi  ,vtest     ,nstepq       ,nfcn       ,nfcnmx
     a/card  / cword   ,cword2    ,word7(7)
     b/minima/ amin          ,up        ,newmin          ,itaur     ,lmi(30)
     c/deriva/ ng,kk
      dimension word8(8)
      equivalence( word8,cword2)
      npunch=0
      itaur=0
      nfcnmx=1500
      epsi=.000000000000001
      nstepq=2
      call tauros
      iflag=3
      call fcn(npar,ng,f,u,iflag)

        ng=ng+1
c       go back to the main routine, fit the next
      call minnew
      return
      end
      subroutine tauros
        implicit double precision (a-h,o-z)
      common
     2/parint/ x(15)  ,xt(15)    ,dirin(15) ,maxint    ,npar
     3/parext/ u(30)  ,w(30)     ,werr(30)  ,maxext    ,nu
     6/unit  / isysrd   ,isyswr
     8/title / title(20)           ,isw(7)    ,nblock
     9/conver/ epsi, apsi  ,vtest     ,nstepq       ,nfcn       ,nfcnmx
     a/card  / cword   ,cword2    ,word7(7)
     b/minima/ amin          ,up        ,newmin          ,itaur     ,lmi(30)
     c/deriva/ ng,kk
      double precision dxn,ddirin
      dimension ddirin(15)
      dimension d(15),y(15),xs(15,15),et(15,15)
   10 np=npar
      iswtr=isw(5)-itaur
      npfn=nfcn
      al=3.
      be=-.4
      gam=-2./(al*be)
      nk=20
```

```
      neq=0
      do 30 i=1,npar
      do 20 j=1,npar
   20 xs(i,j)=0.0
      ddirin(i)=dble(dirin(i))
      if(dabs(ddirin(i)).lt.1.0d-20) dirin(i)=1.0e-20
   30 xs(i,i)=1.0
      iflag=4
      avr=amin
      nst=0
c       write(isyswr,470) epsi,nstepq
      call mprint(1,amin)
c       write(isyswr,480)
   40 ast=amin
      do 270 j=1,np
      y1=1.
      ne=0
      ns=0
      d(j)=0.
      kont=0
   50 do 60 i=1,npar
   60 y(i)=x(i)+dirin(j)*xs(j,i)
      call intoex(y)
      iflag=4
      call fcn(npar,ng,a,u,iflag)
      nfcn=nfcn+1
      y2=amin-a
      if(y2) 110,70,80
   70 if(y1) 90,210,110
   80 ne=0
      amin=a
   90 y1=y2
      ns=1
      do 100 i=1,npar
  100 x(i)=y(i)
   95 continue
      d(j)=d(j)+dirin(j)
      kont=kont+1
      if(kont-nk) 105,105,210
  105 continue
      dirin(j)=al*dirin(j)
      go to 50
  110 kont=kont+1
      if(kont-nk) 115,115,95
  115 dirin(j)=be*dirin(j)
      if(ns) 120,50,120
  120 continue
  130 if(y1) 160,140,160
  140 if(ne) 150,150,210
  150 dirin(j)=gam*dirin(j)
      ne=1
      go to 50
```

```
160 x2=dirin(j)/be
    x1=x2/al
    da=x2*y1
    db=x1*y2
       dpp=da-db
       if(dpp.ge.0.e00.and.dpp.le.1.e-38) dpp=1.e-38
       if(dpp.lt.0.e00.and.dpp.ge.-1.e-38) dpp=-1.e-38
    stj=.5*(da*x2+db*x1)/(da-db)
    if(stj) 170,210,170
170 do 180 i=1,npar
180 y(i)=x(i)+stj*xs(j,i)
    call intoex(y)
    iflag=4
    call fcn(npar,ng,a,u,iflag)
    nfcn=nfcn+1
    if(a-amin) 190,210,210
190 amin=a
    do 200 i=1,npar
200 x(i)=y(i)
    d(j)=d(j)+stj
210 continue
    nst=nst+1
    if(iswtr.ge.3.or.(iswtr.eq.2.and.mod(nst,10).eq.0)) call mprint(0,
   *amin)
260 if(nfcn-nfcnmx-npfn) 270,430,430
270 continue
    ame=amin-ast
    if(ame) 290,280,280
280 write(isyswr,490)
    go to 435
290 if(epsi+ame) 300,410,410
300 neq=0
310 do 320 i=1,npar
320 et(np,i)=d(np)*xs(np,i)
    if(npar.eq.1) go to 40
    do 330 j=2,np
    jj=np+1-j
    do 330 i=1,npar
330 et(jj,i)=et(jj+1,i)+d(jj)*xs(jj,i)
    do 400 j=1,np
    do 340 k=1,npar
340 xs(j,k)=et(j,k)
    if(j-1) 380,380,350
350 do 370 i=2,j
    d(i)=0.
    do 360 k=1,npar
360 d(i)=d(i)+et(j,k)*xs(i-1,k)
    do 370 k=1,npar
370 xs(j,k)=xs(j,k)-d(i)*xs(i-1,k)
380 xn=0.
    do 390 k=1,npar
390 xn=xn+xs(j,k)**2
```

```
      dxn=dble(xn)
      dir=dsqrt(dxn)
      dirin(j)=dir*al
        if(dir.le.1.e-38) go to 2222
      do 400 k=1,npar
  400 xs(j,k)=xs(j,k)/dir
2222  continue
      go to 40
  410 neq=neq+1
      if(neq-nstepq) 310,420,420
  420 continue
      write(isyswr,500)
      go to 435
  430 write(isyswr,510)
      isw(1)=1
  435 continue
      do 450 i=1,npar
      d(i)=0.
      do 450 j=1,np
  440 d(i)=d(i)+dirin(j)*xs(j,i)
  450 continue
      do 460 i=1,npar
  460 dirin(i)=d(i)
      call intoex(x)
      call mprint(1,amin)
      return
c 470 format(1x,'start point for tauros min',/1x,'convergence criterion'
c     1,/1x,'function change less than',e10.2,'during',i3,'full iterat'/)
c  480 format(' ' )
  490 format(1x,'minimization terminated since no improvement',/1x,
     1'can be found on current minimum')
  500 format(1x,'tauros minimization has converged')
  510 format(1x,'0tauros minimization terminated without convergence')
      end

c        subroutine for the fitting function
         subroutine fcn(np,ng,f,x,iflag)
         implicit double precision (a-h,o-z)
         character side*8, outf*18, inf*15,outex*18
         dimension x(np)
         common/input/r(9,3),snois,fix,npoint
         common/conv/y(4000),z(4000),mm,mm1,fsr
         common/conv11/inf,outf,outex
         common/convv/aln
         common/save1/nstar,nend,nn,ntime,cinst(-100:100),calbri(4000)
         common/save2/cpp,cpw,plp,prp,wmpc,bpp(2,3),bpw(2,3),ncentw,psh

         go to (10,20,30,30), iflag
 10      nstar=int(x(2)-r(ng,3)*3)
         nend=int(x(2)+r(ng,3)*3)
         if (nstar.le.1) nstar=1
         if (nend.ge.npoint)nend=npoint
```

```
      nn=nend-nstar+1
      ntime=0
      if (np .eq. 7) ntime=1
      return

30    f=0.0
      if (ng .gt. 3) then
      w0=x(2)-cpp
      btop=(2*w0*x(3))**2
      do 31 m=nstar-ncentw, nend+ncentw
      w=m-psh
      bottom=(w0**2-w**2)**2+(2*w*x(3))**2
      calbri(m)=x(1)*btop/bottom
31    continue
      end if
      do 41 jn=nstar,nend
      z(jn)=0.0
      do 40 i=0,ntime
      k=i*3
      if (ng .le. 3) then
      z(jn)=z(jn)+x(k+1)*exp((-(jn-x(k+2))**2)*aln/x(k+3)**2)
      else
      do 39 l=jn-ncentw,jn+ncentw
      z(jn)=z(jn)+cinst(l-jn)*calbri(l)
39    continue
      end if
40    continue
      z(jn)=z(jn)+x(np)
      e2=(z(jn)-y(jn))**2/(y(jn)+0.05)
      f=f+e2
41    continue
      f=f/nn
      if (iflag .ne. 3) return

      go to (500,600,600,700) ng
      go to 700

500   side=' Center '
      write(6,100) side
      cpp=x(2)
      cpw=x(3)
      write(6,110) x(2), x(1), x(3)
c     make a normalized central response array cinst(i)
      ncent=int(cpp+0.50)
      psh=2*cpp-ncent
      ncentw=int(cpw*4)
      bottom=0.0
      do 501 i=ncent-ncentw,ncent+ncentw
      bottom=bottom+y(i)
501   continue
      do 502 i=ncent-ncentw, ncent+ncentw
      cinst(i-ncent)=y(i)/bottom
```

```
502    continue
       go to 800

600    if (ng .eq. 2) then
       side=' Left  '
       plp=x(2)
       if (x(5) .gt. x(2)) plp=x(5)
       end if
       if (ng .eq. 3) then
       side=' Right  '
       prp=x(5)
       if (x(5) .gt. x(2)) prp=x(2)
       end if
       write(6,100) side
       print*,'For peak (1):'
       write(6,110) x(2), x(1), x(3)
       print*,'For peak (2):'
       write(6,110) x(5), x(4), x(6)
       go to 800

700    side=' Left  '
       k=1
       i=ng-3
       if (ng .gt. mm+3) then
       side=' Right  '
       k=2
       i=ng-mm-3
       end if
       write(6,130) side
       print*,'For the mode (', i,'):'
       write(6,110) x(2), x(1), x(3)
       write(6,140) x(3)
       bpp(k,i)=x(2)
       bpw(k,i)=x(3)

800    write(6,120) f, x(np)
       return

100    format(/1x,'Result for the Rayleigh line at the (',a8,'):')
110    format(1x,'position=',e12.5,2x,'heigh=',e12.5,2x,'hwhm=',e12.5)
120    format(1x,'chi square=',e12.5,2x,'nois=',e12.5)
130    format(/1x,'Result for the Brillouin line at the (',a8,'):')
140    format(1x,'the true width(hwhm)=',e12.5)
160    format(1x,'position(1/cm)=',e12.5,2x,'true hwhm(1/cm)=',e12.5)
170    format(1x,'average shift(1/cm)=',e12.5,2x,'average hwhm(1/cm)
     +=',e12.5)
172    format(1x,'brillouin peaks distance(in chanel numbers)',f9.3)

20     wmpc=1.0/(fsr*(prp-plp))
       open(10,file=outf,status='new')
       open(12,file=outex,status='new')
       do 50 i=1,npoint
```

```
         wx=(i-cpp)*wmpc
         write (10,200) wx, z(i)
         write (12,200) wx, y(i)
50       continue
200      format(f8.4, e12.5)
         close (10)
         close (12)
         wit=cpw*wmpc
         print'(/1x,"hwhm(instrument in 1/cm)=",e12.5)',wit
         print'(/1x,"fsr*2(in chanel number)=",f9.3)',prp-plp
         do 52 j=1,2
         side=' Left '
         if (j .eq. 2) then
         side=' Right '
         mm=mm1
         end if
         write(6,130) side
         do 54 i=1,mm
         bposi=wmpc*(bpp(j,i)-cpp)
         thwhm=wmpc*bpw(j,i)
         print*,'For the mode (', i,'):'
         write(6,160) bposi, thwhm
54       continue
52       continue
         if ( mm .eq. mm1) then
         do 56 i=1,mm
         dbpp=bpp(2,i)-bpp(1,i)
         avposi=wmpc*dbpp/2.0
         avhwhm=wmpc*(bpw(2,i)+bpw(1,i))/2.0
         print'(1x/1x,"For the mode ( ",i1," ):")',i
         write(6,170) avposi, avhwhm
         write(6,172) dbpp
56       continue
         end if
         print'(/1x,"The ",a10," and ",a10," files are ready for
     +   plotting.")',outf,outex
         return
         end
```

REFERENCES

[A1]J.D. Axe, Phil. Trans. R. Soc. Lond B 290 593 (1980).

[A2]J.D. Axe, Proceeding of the Gatlinsburg neutron scattering conference, (1976).

[A3]K. Aiki, K. Hukuda and O. Matumura, J. Phys. Soc. Jpn. 26 1064 (1969).

[A4]K. Aiki, and K. Hukuda, J. Phys. Soc. Jpn. 26 1066 (1969).

[A5]K. Aiki, K. Hukuda and T. Kodayashi, J. Phys. Soc. Jpn. 28 389 (1970).

[A6]J.D. Axe, M. Iizumi and G. Shirane, Phys. Rev. B 22 3408 (1980).

[A7]T. Atake, K. Nomoto, B.K. Chaudhuriand and H. Chihara, J. Chem. Thermodynamics 15 383 (1983).

[A8]J.D. Axe, M. Iizumi, G. Shirane, in "Incommensurate Phases in Dielectrics" 2. Materials, edited by R. Blinc and A.P. Levanyuk (North Holland, Amsterdam) P.1 (1986).

[A9]S.R. Andrews and H. Mashiyama, J. Phys. C 16 4985 (1983).

[B1] J.P. Benoit, G. Hauret, Y. Luspin, A. M. Gillet and J. Berger, Solid State Commun. 54 1095 (1985).

[B2] R. Blinc, V. Rutar, B. Topic, F. Milia and T. Rasing, Phys. Rev. B 33 1721 (1986).

[B3] A.D. Bruce and R.A. Cowly, J. Phys. C: Solid State Phys. 11 3609 (1978).

[B4] R. Blinc, P. Prelovsek, V. Rutar, J. Sdiger and S. Zumer, in "Incommensurate Phases in Dielectrics", 1, edited by R. Blinc and A.P. Levanyuk (North Holland, Amsterdam) P.143 (1986).

[B5] D.S. Bedboroagh and D.A. Jackson, J. Phys. E: Instrum. 11 473 (1978).

[B6] E.M. Brody and H.Z. Cummins, Phys. Rev. B 9 179 (1974).

[B7] E.M. Brody and H.Z. Cummins, Phys. Rev. Lett. 21 1263 (1968).

[B8] B. Berge, G. Dolino, M. Vallade, M. Boissier and R. Vacher, J. Phys. 45 715 (1984).

[C1] C.E. Chen, Y. sdalesinger and A.J. Heeger, Phys Rev. B 24 5139 (1981).

[C2] B.K. Chauduri, T. Atake and H. Chihara, Solid State Commun. 37 123 (1981).

[C3] M. Cho and T. Yagi, J. Phys. Soc. Jpn. 50 543 (1981).

[C4] A.S. Charez, R. Gazzinelli and R. Blinc, Solid State Commun. 37 123 (1981).

[C5] H.Z. Cummins, Phys. Reports, 185 (1990).

[C6] H.Z. Cummins and Paul E. Schoen, Jr., in "Laser Handbook", edited by F.T. Arecchi and E.O. Schultz-DuBois (North Holland, Amsterdam), 1029 (1971).

[C7] Z.Y. Chen, Phys. Rev. B 41 9516 (1990).

[D1] P.M. deWolff, Acta Cryst. A30 777 (1974).

[D2] V. Dvorak and J. Petzelt, J. Phys. C: Solid State Phys. 11 4827 (1978).

[D3] R. Dengler and F. Schwabl, Z. Phys. B 69 327 (1987).

[D4] V. Dvorak and S.K. Esayan, Solid State Commun. 44 901 (1982).

[D5] V. Dvorak and O. Hudak, Ferroelectrics 46 19 (1982).

[E1] P. Echegut, F. Gervais and N.E. Massa, Phys. Rev. B 31 581 (1985).

[E2] S.K. Esayan and V.V. Lemanov, Izv. Akad. Nauk. SSSR, Ser. Frz. 47 591 (1985).

[E3] P. Echegut, F. Gervais and N.E. Massa, Phys. Rev. B 34 278 (1986).

[E4] S.K. Esayan, V.V. Lemanov, N. Mamatkulov and L.A. Shuvalov, Sov. Phys. Crystallogr. 26 619 (1981).

[F1] P.A. Fleury, S. chiang and K.B. Lyons, Solid State Commun. 31 279 (1985).

[F2] I.N. Flerov, L.A. Kot and A.I. Kriger, Sov. Phys. Solid State 24 954 (1982).

[F3] M. Fukui and R. Abe, J. Phys. Soc. Jpn. 51 3942 (1982).

[F4] I.J. Fritz, Phys. Lett. 51A 219 (1975).

[G1] G. van Gattow, Acta Cryst. 15 419 (1962).

[G2] V.V. Gladii, in "Incommensurate Phases in Dielectrics", 1, edited by R. Blinc and A.P. Levanyuk (North Holland, Amsterdam), P.309 (1986).

[G3] R.J. Gooding and M.B. Walker, Phys. Rev. B 35 6831 (1987).

[G4] R.J. Gooding and M.B. Walker, Phys. Rev. B 36 5377 (1987).

[H1] H. Hoshizaki, A. Sawada, Y. Ishibashi, T. Matsuda and I. Hatta, Jpn. J. Appl. Phys. Lett. 19 L324 (1980).

[H2] G. Hauret and J.F. Benoit, Ferroelectrics 40 1 (1982).

[H3] M. Horioka, A. Sawada and R. Abe, Jpn. J. Appl. Phys. 19 L145 (1980).

[H4] M. Horioka, A. Sawada and R. Abe, Ferroelectrics 39 347 (1981).

[H5] M.S. Haque and J.R. Hardy, Phys. Rev. B 21 245 (1980).

[H6] Hayes and Louden, "Scattering of Light by Crystals" (John Wiley & Sons), (1978).

[H7] K.F. Herzfeld and T. Lilovitz, "Absorption and Dispersion of Ultrasonic Waves" (Academic, New York), p.45 (1959).

[H8] J.J.L. Horikx, A.F.M. Arts, J.I. Dijkhuis and H.W. de wijn, Phys. Rev. B 39 5726 (1989).

[H9] J. Hu, J.O. Fossum, C.W. Garland and P.W. Wallace, Phys. Rev. B 33 6331 (1986).

[H10] S. Hirotsu, K. Toyota and K. Hamano, J. Phys. Soc. Jpn. 46 1389 (1979).

[I1] M. Iizumi, J.D. Axe, G. Shirane and K. Shimaoka, Phys. Rev. B 15 4392 (1977).

[I2] K. Inoue, and Y. Ishibashi, J. Phys. Soc. Jpn 52 556 (1983).

[I3] Y. Ishibashi, J. Phys. Soc. Jpn. 51 1220 (1982).

[I4] Y. Ishibashi, in "Incommensurate Phases in Dielectrics", 2, edited by R. Blinc and A.P. Levanyuk (North Holland, Amsterdam), P.49 (1986).

[I5] H. Iro and F. Schwabl, Solid State Commun. 46 205 (1983).

[J1] A.K. Jain, Solid State Commun. 31 237 (1979).

[K1] A. Kalman, J.S. Stephens and D.W.J. Cruickshank, Acta Crystal B 26 451 (1970).

[K2] N.N. Kolpakova, B. Brezina and E.S. Sher, Jpn J. Appl. Phys. 24 S24-2 823 (1985).

[K3] S. Kudo and T. Ikeda, J. Phys. Soc. Jpn. 50 3681 (1981).

[K4] J. Kroupa, J. Fousek, F. Smutny and B. Brezina, Phys. Status Solidi B 113 K153 (1982).

[K5] S. Kudo and Y. Ikeda, Jpn. J. Appl. Phys. 19 L45 (1980).

[L1] W.K. Lee, H.z. Cummins, R.M. Pick and C. Dreyfus, Phys Rev. B 37 642 (1988).

[L2] A. Lopez-Echarri, M.J. Tello and P. Gili, Solid State Commun. 36 1021 (1980).

[L3] V.V. Lemanov, S.Kh. Esayan and A. Karaev, Sov. Phys. Solid State 28 931 (1986).

[L4] Y. Luspin, G. Hauret, A.M. Robinet and J.P. Benoit, J. Phys. C 17 2203 (1984).

[L5] H.M. Lu and J.R. Hardy, Phys. Rev. Lett. 64 661 (1990).

[L6] L.D. Landau and I.M. Khalatnikov, Academy of Sci. USSR. Proceedings 96 (1954).

[L7] B. Luthi and W. Rehwald, in "Structural Phase Transitions I" edited by K.A. Muller and H. Thomas (Springer Verlag, Berlin) P.131 (1981).

[L8] L.D. Landau and E.M. Lifschitz, "Statistical Physics" (Addison Wesley, Reading,Mass) P.124 (1958).

[L9] A.P. Levanyuk, in "Incommensurate Phases in Dielectrics" 1, edited by R. Blinc and A.P. Levanyuk (North Holland, Amsterdam) P.1 (1986).

[L10] A.P. Levanyuk, Sov. Phys. JETP. 22 901 (1966).

[L11] J.C. Le Guillou and J. Zinn-Justin, Phys. Rev. Lett. 39 95 (1977).

[L12]J.C. Le Guillou and J. Zinn-Justin, Phys. Rev. Lett. 21 3976 (1979).

[L13]J.D. Litster, Ferroelectrics 15 225 (1983).

[L14]A.P. Levanyuk, Private communication (1990).

[L15]Y. Luspin, M. Chabinand and F. Gilletta, J. Phys. C: Solid State Phys. 15 1581 (1982).

[L16]H.M. Lu and J.R. Hardy, Accepted by Phys. Rev. B (1990).

[L17]G. Li, N. Tao, L. V. Hong, H.Z. Cummins C.Dreyus, M. Hebbache, R.M. Pick, and J. Vagner, Phys. Rev. B 42 4406 (1990).

[M1]C.F. Majkrzak, J.D. Axe and A.D. Bruce, Phys. Rev. B 22 5278 (1980).

[M2]M. Midorikawa, J. Phys. Soc. Jpn. Lett. 50 2141 (1981).

[M3]H. Mashiyama and H. G. Unruh, J. Phys. C: Solid State Phys. 16 5009 (1983).

[M4]H. Mashiyama, Phys. Stat. Sol. 118 757 (1983).

[M5]H. Mashiyama, H.G. Unruh, J. Phys. C: Solid State Phys. 16

[M6]H. Mashiyama, J. Phys. Soc. Jpn. 50 2665 (1981).

[M7]W.P. Mason, Phys. Rev. B 69 173 (1946).

[M8]N.E. Massa, F.G. Ullman and J.R. Hardy, Phys. Rev. B 27 1532 (1983).

[M9]T. Matsuda and I. Hatta, J. Phys. Soc. Jpn. 48 157 (1980).

[N1] D.F. Nelson and M. Lax, Phys. Rev. B 13 1785 (1976).

[N2] D.F. Nelson, Electric Optic and Axoustic Interactions in Dielectrics (Wiley, New York, 1979).

[P1] W. Press, C.F. Majkrzak, J.D. Axe, J.R. Hardy, N.E. Massa and F.G. Ullman, Phys. Rev. B 22 332 (1980).

[P2] J.Petzelt, G.V. Kozlov, A.A. Volkov and Y. Ishibashi, Z. Phys. B 33 369 (1979).

[P3] H. Poulet and R. Pick, J. Phys. C: Solid State Phys. 14 2675 (1981).

[Q1] M. Quilichini and R. Currat, Solid State Commun. 48 1011 (1983).

[R1] W. Rehwald, A. Vonlanthen, J.K. Kruger, R. Wallerius and H.G. Unruh, J. Phys. C: Solid State Phys. 13 2823 (1980).

[R2] W. Rehwald and A Vonlanthen, Solid State Commun. 38 209 (1981).

[R3] W. Rehwald, Advances in Phys. 22 721 (1973).

[S1] S. Shiozaki, A. Sawada, Y. Ishibashi and Y. Takagi J. Phys. Soc. Jpn. 43 1314 (1977).

[S2] G.A. Samara, N.E. Massa and F.G. Ullman, Ferroelectrics 36 335 (1981).

[S3] M. Suhara, A Azuma, M. Hamasaka, K. Aiki and T. Kobayashi, Ferroelectrics 66 295 (1986).

[S4] D.G. Sannikov and A.P. Levanyuk, Sov. Phys. Solid State 20 580 (1978).

[S5] D.G. Sannikov and V.A. Golovoko, Sov. Phys. Solid State 26 678 (1984).

[S6] D. G. Sannikov, in "Incommensurate Phases in Dielectrics" 1, edited by R. Blinc and A.P. Levanyuk (North Holland, Amsterdam), P.43 (1986).

[S7] J.R. Sandercock, in "Proc. 2nd Int. Conf. on Light Scattering in Solids" edited by M. Balkanski, 9 (1971).

[S8] J.R. Sandercock, Solid State Commun. 26 547 (1978).

[S9] J.R. Sandercock, "Operator Manual for Tandem Interferometer", (1980)

[S10]F. Schwabl, Ferroelectrics 78 215 (1988).

[S11]F. Schwabl, J. Stat. Phys. 39 719 (1985).

[S12]J.F. Scott, Ferroelectris 66 11 (1986).

[S13]J.F. Scott and J.A. Sanjurjo, Solid State Commun. 58 678 (1986).

[T1] H. Terauchi, H. Takenaka and K. shimaoka, J. Phys. Soc. Jpn 39 435 (1975).

[T2] B. Topic, U. Haeberlen and R. Blinc, Phys. Rev. B 40 799 (1989).

[U1] H.G. Unruh, W. Eller and G. Kirf, Phys. Status Solidi A 55 173 (1979).

[V1] A.A. Volkov, I. Ishibashi, G.V. Kozlov and Petzelt, Sov Phys. Solid State 22 831 (1980).

[V2] A.A. Volkov, G.v. Kozlov, J. Petzelt and O. Hudak. Ferroelectrics 66 313 (1986).

[W1]M. Wada, A. Sawada, Y. Ishibashi and Y. Takagi, J. Phys. Soc. Jpn. 42 544 (1977).

[W2]M. Wada, H. Uwe, A. Sawada, Y. Ishibashi, Y. Takagi and T. Sakudo, J. Phys. Soc. Jpn. 43 544 (1977)

[W3]M. Wada, H. shichi, A Sawada and Y. Ishibashi, J. Phys. Soc. Jpn. 51 3245 (1982).

[W4]K.G. Wilson, Phys. Rev. B 4 3184 (1971).

[W5]K.G. Wilson, Phys. Rev. B 4 3174 (1971).

[Y1] N. Yamada and T. Ikeda, J. Phys. Soc. Jpn. 53 2555 (1984).

[Y2] N. Yamada, Y. Ono and T. Ikeda, J. Phys. Soc. Jpn. 53 2565 (1984).

[Y3] N. Yamada and T. Ikeda, Ferroelectrics 53 323 (1984).

[Y4] T. Yagi, M. Cho and Y. Hidaka, J. Phys. Soc. Jpn. 46 1957 (1979).

[Y5] W. Yao, H.Z. Cummins and R.H. Bruce, Phys. Rev. B 24 424 (1981).

[Z1] M.W. Zemansky, "Heat and Thermodynamics" (McGraw-Hill, New York) p.133 (1957).